ABSTRACT

A VACUUM-DRIVEN DISTILLATION SYSTEM OF AQUEOUS SOLUTIONS AND MIXTURES

by
Guangyu Guo

Distillation of aqueous solutions and aqueous mixtures has vast industrial applications, including desalination, wastewater treatment, and fruit juice concentration. Currently, two major distillation technologies are adopted in the industry, membrane separation and thermal distillation. However, both of them face certain inevitable drawbacks. Membrane separation has disadvantages as relying on high-grade energy, requiring membrane, fouling problem, narrow treatment range, limited scalability, and vibrating and noisy operating conditions. Traditional thermal distillation technologies can avoid above concerns but has other shortcomings, such as relatively low energy efficiency and yield rate, complicated and bulky system structure, and scaling problem.

This project proposes an innovative membrane-free low-grade energy driven distillation technology that overcomes all the above drawbacks in current membrane distillation and thermal distillation via a multi-stagger-staged spray flash distillation system. The technology consists of three innovative features: polydispersed spray flash distillation process for improving the evaporation rate and efficiency; the multi-stagger stage arrangement of the system design for realizing a parallel operating control with inter-stage heat recovery; actively vacuumed vapor extraction for achieving a highly thermal non-equilibrium process. Specifically, spray nozzles are equipped within each evaporation chamber to take advantage of pressure dropping demand and boost the distillation effect by dramatically increasing the evaporation area. Each stage is parallelly arranged with each

other, in which only the first stage needs an external heat input, and the rest of the stages will be heated via inter-stage heat recovery. All stages are connected to the same active vacuum source. Hence, the operating pressure of each stage can be independently controlled to achieve the most optimized operation. The distillation efficiency will be improved and the non-condensable gas will be timely removed by such an active vapor extraction. In this way, the proposed system can achieve unique advantages such as low-grade heat driven, better yield rate and energy efficiency, no membrane, wider treatment range, scalable, no scaling problem, and safe and quiet operating conditions.

In this dissertation, the technology is developed by the following research logic: proposing an overall system design with working concepts; parametrically studying the curial sub-processes (spray flash and vapor vacuuming) via models and experiments; building the overall systematic model for thermodynamic analysis and system optimization. Specifically, interwind sub-works are conducted as follows: a design of multi-stagger-stage actively vacuumed distillation system; modeling and experimental study of highly non-equilibrium spray flash process; modeling and experimental study of the further spatially dependent salinity effect in spray flash distillation; a point-based modeling methodology of droplet flash process; a CFD study of spray flash process; modeling and experimental study of a lab-scale two-stage prototype; thermodynamic analysis with an overall systematic model.

A VACUUM-DRIVEN DISTILLATION SYSTEM OF AQUEOUS SOLUTIONS AND MIXTURES

by
Guangyu Guo

A Dissertation
Submitted to the Faculty of
New Jersey Institute of Technology
in Partial Fulfillment of the Requirements for the Degree of
Doctor of Philosophy in Mechanical Engineering

Department of Mechanical and Industrial Engineering

December 2021

APPROVAL PAGE

A VACUUM-DRIVEN DISTILLATION SYSTEM OF AQUEOUS SOLUTIONS AND MIXTURES

Guangyu Guo

Dr. Chao Zhu, Dissertation Co-Advisor — Date
Professor of Mechanical Engineering, NJIT

Dr. Zhiming Ji, Dissertation Co-Advisor — Date
Professor of Mechanical Engineering, NJIT

Dr. Joga I. Rao, Committee Member — Date
Professor of Mechanical Engineering, NJIT

Dr. Eon Soo Lee, Committee Member — Date
Professor of Mechanical Engineering, NJIT

Dr. Teh Chung Ho, Committee Member — Date
Senior Research Associate, ExxonMobil Research and Engineering, Annandale, NJ

BIOGRAPHICAL SKETCH

Author: Guangyu Guo

Degree: Doctor of Philosophy

Date: December 2021

Undergraduate and Graduate Education:

- Doctor of Philosophy in Mechanical Engineering,
  New Jersey Institute of Technology, Newark, NJ, 2021

- Master of Science in Mechanical Engineering,
  New Jersey Institute of Technology, Newark, NJ, 2016

- Bachelor of Science in Energy Science and Engineering
  Harbin Institute of Technology, Harbin, P. R. China, 2013

Major: Mechanical Engineering

Presentations and Publications:

G. Guo, C. Zhu, A modified lumped heat capacity model for droplet flash cooling, International Communication in Heat and Mass Transfer. 127 (2021) 105557.

G. Guo, B. Zhang, C. Zhu, Z. Ji, Thermal non-equilibrium in spray flash with vacuum vapor extraction, Desalination. 507 (2021) 115023.

G. Guo, H. Deng, C. Zhu, Z. Ji, Spatially dependent salinity effect in actively vacuumed spray flash distillation, Desalination. (under review).

G. Guo, C. Zhu, M. Zhou, Z. Ji, A, A single-stage spray flash distillation system with active vapor extraction, manuscript finished.

B. Zhang, G. Guo, C. Zhu, Z. Ji, C.-H. Lin, Transport and trajectory of cough-induced bimodal aerosol in an air-conditioned space, Indoor Built Environment. (2020) 1420326X2094116.

B. Zhang, F. Du, G. Guo, C. Zhu, Z. Ji, C.H. Lin, Modeling and thermodynamic cycle analysis of condensation-induced depressurization, Vacuum. 164 (2019) 77–87.

H. Deng, X. Yang, R. Tian, J. Hu, B. Zhang, F. Cui, G. Guo, Modeling and optimization of solar thermal-photovoltaic vacuum membrane distillation system by response surface by methodology, Solar Energy. 195(2020)230-238.

G. Guo, H. Deng, C. Zhu, Z. Ji, Numerical study of vacuum-aided spray flash desalination, 6th Thermal and Fluids Engineering Conference. (2021) 777–787.

G. Guo, H. Deng, C. Zhu, Z. Ji, Non-volatile fraction effects in dispersed vacuum spray flash evaporation, International Mechanical Engineering Congress and Exposition. (2020) V011T11A010.

G. Guo, C. Zhu, Z. Ji, CFD simulation of isolated spray flash evaporation with active vapor extraction, 5th Thermal and Fluids Engineering Conference. (2020) 269–278.

G. Guo, H. Deng, C. Zhu, Z. Ji, Non-equilibrium evaporation in a vacuum spray flash, 4th thermal and Fluids Engineering Conference. (2019) 28099.

B. Zhang, G. Guo, C. Zhu, Z. Ji, Transport of aerosol by coughing in an air-conditioned space, 4th Thermal and Fluids Engineering Conference. (2019) 1341–1353.

H. Deng, G. Guo, Z. Ji, C. Zhu, Solar-powered condensation vacuum technology, Heat 4th Thermal and Fluids Engineering Conference. (2019) 585-593.

G. Guo, Condensation vacuum pumping and actuating technology, 65th International Symposium and Exhibition of American Vacuum Society. (2018) VT-WeM5

B. Zhang, G. Guo, C. Zhu, Z. Ji, Dynamic process modeling on a condensation-based depressurization system, 63th International Symposium and Exhibition of American Vacuum Society. (2016) VT-MoA5

Patents and Awards:

G. Guo, National Science Foundation Innovation Corps Award, National Science Foundation of USA, 2021.

C. Zhu, Z. Ji, M. Zhou, G. Guo, B. Zhang, Edison Patent Award, Research and Development Council of New Jersey, 2020.

C. Zhu, Z. Ji, M. Zhou, G. Guo, B. Zhang, Vaccum distillation and desalination, U.S. Patent 10661194, 2018.

To my family and their unconditional love.

To the important people in my heart, the ones with me now, and the one I lost on the way.

To those anxieties, those loneliness, those struggles, those pains,

and those goodliness.

呈现在你眼前的这本论文，大约是我六年科研工作里的一半内容。

正如大家一样，为了研究这个课题，我付出了很多。回头看看，这些年吃过的苦，走过的路，便成了自己目前最宝贵的人生财富。

称之为人生财富，并非是在期许我的工作能赢得多少他人的赞誉，而真正的意义在于——这一路点点滴滴的挣扎与坚持赢得了我对自己的尊重。

因为我终于得以确认：即便如此平凡的自己，至少也能够做到仅凭一腔信念而去选择背负失败与挫折前进。

现在的我，会带着不能辜负所经风雨的尊严，骄傲的去面对未来人生长路上的困难与使命。

ACKNOWLEDGMENT

I want to express my sincere gratitude to my mentor, Professor Chao Zhu, who not only instilled research skills and academic knowledge, but also greatly supported me beyond research in my life, especially during my most difficult time. I also want to thank my program director and co-advisor, Professor Zhiming Ji, who helped me hugely in my research and campus life. I would like to thank Professor Mengchu Zhou, who offered me many opportunities to pursue academic achievements. I also sincerely thank the Chair and Professor I. Joga Rao, Professor Eon Soo Lee, and the member of National Academy of Engineering and former ExxonMobil sensor research associate, Doctor Teh Chung Ho, for serving as my committee members.

I appreciate our Department of Mechanical and Industrial Engineering for the continuous financial support all the time. I would like to thank the Boeing Technical fellow Doctor Chao-Hsin Lin, for his professional and friendly assistance in our project. I appreciate Mr. Hanafin Ben and AiVacua the company he led, for their precious support to my research all the time. I also want to thank Professor Wen Zhang, who kindly offered help in analyzing our results.

I have so many friends to express my appreciation that cannot even be fully covered here. Our Lab Coordinator Joseph Glaz and his team Gregory Policastro and Nick, who supported me with valuable help all the time. Professor Herli Surjanhatta, the kindest teacher I have ever known. My groupmates and closest friends, Bo Zhang, Fangda Cui, Pan Gao, Hongling Deng, and Caiwu Ding, who always stand with me in those uncountable hard-working times.

TABLE OF CONTENTS

TABLE OF CONTENTS
(Continued)

TABLE OF CONTENTS
(Continued)

Chapter **Page**

TABLE OF CONTENTS
(Continued)

Chapter **Page**

LIST OF TABLES

LIST OF TABLES
(Continued)

LIST OF FIGURES

LIST OF FIGURES
(Continued)

LIST OF FIGURES
(Continued)

LIST OF FIGURES
(Continued)

Figure **Page**

NOMENCLATURE

A	projected area
Bi	Biot number
C	mass fraction of salt
C_d	drag coefficient
c	molar concentration; specific heat
D	diffusion coefficient
d	diameter
F	force
g	gravitational constant
h	heat; convective coefficient
k	Thermal conductivity
L	dimensionless latent heat
M	molecular weight
MW	molecular weight
m	mass
N	mole fraction; group number
n	number density
O	effective vapor coefficient
P	pressure
R	universal gas constant
r	radius

T	temperature
t	time
$\mathbf{u}$	velocity
V	volume

Greek Letters

α	evaporative coefficient
β	dimensionless evaporation
γ^*	thermal non-equilibrium ratio
Δ	difference
η	evaporation efficiency
θ	superheat ratio
λ	fitting slope
μ	dynamic viscosity
σ	surface tension
ρ	density

Subscripts

A	area
a	added mass
$cell$	the control volume
ch	chamber
d	droplet, drag

E	effective heat conduction
e	end
eff	effective
f	fluid
i	order number
j	size/trajectory number
L	Lumped heat capacity
l	liquid(water)
m	modified phase, average, molar
fg	latent heat
o	outlet
p	isobaric
S	Spatially dependent
s	surface
sat	saturated condition
T	turbulent
t	processing time
u	universal
v	vapor
vd	vapor-droplet
w	water
x	internal local position
0	initial condition

∞	far-field ambient

CHAPTER 1

INTRODUCTION

1.1 Background of Water Scarcity

The economic and population growths of the world are leading to an ever-increasing demand for energy and water. Water scarcity already affects every continent. Almost one-fifth of the world's population lives in areas of physical scarcity and an increasing number of regions are chronically short of water [1]. A substantial amount of freshwater is polluted, wasted, and unsustainably managed. Only less than one percent of water on the earth's surface is suitable as an eligible water source for direct consumption in domestic or industrial applications [2]. More energy-intensive water is currently being used to compensate for the decline in water availability. Purification and distillation of wastewater, seawater, dirty water, oil-based water, or brackish water become an important, but expensive, solution for water supply issues [3]. On the other hand, certain concentration applications which are the opposite processes of distillation will also be benefited by improving energy efficiency of the technology of distillation, like juice concentration, production of chemical products, etc. [4]

1.2 Overview of Distillation Technologies

Distillation involves the production of evaporative/condensable solvents from non-evaporative solvents and/or solutes, such as freshwater from wastewater or saline water. Distillation is one of the earliest forms of water treatment. There are two basic methods:

thermal distillation and membrane separation [5]. Thermal distillation uses heat to boil to-be-treated water into vapor, leaving the non-evaporative solvents or solutes behind, that is collected and condensed back into water by cooling it down. Some derivatives of the methods include vacuum distillation processes used in refineries. The process involves vaporous extraction of water. Vapor compression distillation (VCD) is a thermal desalination process, such as MSF (multi-stage flash) and MED (multiple effect distillation), which has in the past provided the majority of potable water in regions where excess heat from power plants is used to heat and desalinate seawater. These are efficient and viable solutions when there is waste heat or sufficient electricity available.

In membrane separation, seawater is forced through a semipermeable membrane that separates salt from water. The most common type of membrane separation can be divided into two categories: the thermally-driven membrane separation, and the pressure-driven membrane separation. In thermally-driven membrane distillation (MD), only vapor molecules are able to transfer through the membrane. The driving force in the MD process is the vapor pressure difference induced by the temperature difference across the hydrophobic membrane. Generally speaking there are four popular technologies based on different separation condition: Direct Contact membrane distillation (DCMD), Air Gap Membrane Distillation (AGMD), Sweep Gas membrane distillation (SGMD) and Vacuum Membrane Distillation (VMD).

In membrane separation, seawater is forced through a semipermeable membrane that separates salt from water. The most common type of membrane separation can be divided into two categories: the thermally-driven membrane separation, and the pressure-driven membrane separation.

Membrane distillation (MD) uses hydrophobic membranes and differences in vapor pressure for separation and distillation. The vapor pressure difference across a membrane can be generated by pressurization (such as in reverse osmosis distillation), heating (such as in thermal membrane distillation), or vacuuming, or their combination. Vapor compressor has been used in some MD processes to increase the difference in vapor pressure in membrane distillation. Vacuum has also been applied in other MD processes to maintain the pressure in the permeate side of the membrane at less than the saturation pressure of the vapor to be separated from the hot feed solution. Common configurations of membrane distillation are Direct Contact membrane distillation (DCMD), Air Gap Membrane Distillation (AGMD), Sweep Gas membrane distillation (SGMD) and Vacuum Membrane Distillation (VMD).

In Direct Contact membrane distillation (DCMD), both sides of the membrane are directly contacted with liquid: hot feed water on the evaporator side and cooler yield on the permeate side. The condensation of the vapour passing through the membrane happens directly inside the liquid phase at the membrane boundary surface. Since the membrane is the only barrier blocking the mass transport, relatively high surface related permeate flows can be achieved with DCMD. However the most obvious disadvantage of DCMD is the high sensible energy loss by heat conduction, as the insulating properties of the single membrane layer are low. This lost heat is not available to the distillation process whereby its efficiency is lowered [5-7].

Air Gap Membrane Distillation (AGMD) has the similar evaporator channel resembles that in DCMD, whereas a permeate air gap lies between the membrane and the cooled walling. The vapor passing through the membrane must additionally overcome this

air gap before condensing on the cooler surface. The advantage of this arrangement is relative high thermal insulation (comparing with DCMD) towards the condenser channel, thus minimizing heat conduction losses. However, the disadvantage is that the air gap represents an additional barrier for mass transport, reducing the rate of permeate flux compared to DCMD [5-7].

Sweep Gas membrane distillation (SGMD), also known as air stripping, which has a very similar configuration as AGMD, which arranges an empty gap on the permeate side. The difference is a batch of inert gas is used to sweep the vapor out of the permeate membrane side to condense outside the membrane module. In other words, the gas barrier in SGMD is not stationary for enhancing the mass transfer coefficient. Hereby higher surface-related product water mass flows can be achieved than with AGMD. However, the disadvantage from that features of SGMD is the higher condenser capacity is required because of the increasing of total gas flow, which caused a negative influence on miniaturization and simplification of the structure [5-7].

Vacuum membrane distillation (VMD) uses vacuum to achieve higher partial pressure gradients, and hence higher permeate flux. It contains a similar air gap channel configuration except using pump to create a vacuum in the permeate membrane side. Once it has passed through the membrane, the vapor is sucked out of the permeate channel and condenses outside the module as with SGMD. One advantage of this method is that undissolved inert gasses blocking the membrane pores are able to be sucked out by the vacuum, leaving a larger effective membrane surface active. Furthermore, a reduction of the boiling point results in a comparable amount of product at lower overall temperatures and lower temperature differences through the membrane. A lower required temperature

difference leaves a lower grade thermal energy demand. However, the electrical energy demand of VMD due to the vacuum producing is a lot higher as with DCMD and AGMD [5-7].

In pressure-driven membrane separation, the most widely used technology is reverse osmosis (RO), where high pressure is applied to drive the solvent moves from the high solute concentration through a certain semipermeable membrane to an area of lower solute concentration. The difference between RO and other forms of MD is that the entire process happens under a normal temperature, which does not need heat supplied to establish the pressure difference. Because of high working pressure and no heating needed, RO has its own advantage of high yield rate and relative low energy cost comparing with MD technologies. However, on the other side, a heavily reliance on high-grade energy-electrical power, a high pressure working environment, lower porosity requirement, higher fouling rate, and an increased requirements for membranes than with MD, becomes new drawbacks [8].

Besides these membrane-needed distillation technologies above, thermal distillation is one of the earliest forms of water treatment. Which is using heat to boil water into vapor, leaving the salt behind, that is collected and condensed back into water by cooling it down. Some of the methods are derivatives of vacuum distillation processes used in refineries, such as MSF (multi-stage flash) and MED (multiple effect distillation), which has in the past provided the majority of potable water in regions where excess heat from power plants is used to heat and desalinate seawater. These are efficient and viable solutions when where waste heat or sufficient electricity available. Comparing with membrane separation, thermal distillation do not exist the common shortcomings that

usually accompanied with membrane, like fouling problem, narrow handling range of feed water, and high maintenance cost. However, traditional popular advanced thermal distillation like MSF or MED, are facing the new drawbacks of lower energy efficiency, complicated and bulky system structure, and high demand in materials and electrical power for pressurized or vacuumed working environment [9].

Multi-stage flash distillation (MSF) can be either a once-through (no brine recirculation) or brine recirculation flow system. Successive evaporation of brine water into flash steam is coupled with condensation inside the stages, such that the evaporation latent heat is recovered by preheating feed seawater. During the process, the feed flows through cooling tubes inside the condensation chambers of stages to receive the latent heat of the vapor to produce condensate and vacuum. The direction of the flow is from the last stage to the first stage and the temperature of the feed is increased by each stage. After exiting the first stage, the temperature of the feed is further increased by a heater. The heated feed is then flows through the evaporation chambers of stages, from the first to the last. The vacuum formed in the condensation chamber of the stage reduces the pressure inside the evaporation chamber below the vapor pressure of the liquid, inducing the liquid inside the chamber to evaporate at a rate self-sustained with the condensation later in the condensation chamber. An orifice is placed on the flow path of the feed between two neighboring stages for reducing the pressure of the flow. Demisters are placed between the evaporation and condensation chambers to remove the entrained brine droplets from the vapor. This is essential to prevent increase in the salinity of product water or scale formation on the outer surface of the condenser tubes.

Seawater has many different gases dissolved in it, especially nitrogen, oxygen, carbon dioxide and argon. They do not react chemically and are not easily condensed by cooling. They are referred to as non-condensable gases (NCG). The presence of non-condensable gases may also be caused by the leakage of ambient air into the process operating under vacuum. The presence of non-condensable gases is a serious problem in seawater distillation. Extensive pretreatment, which includes de-aeration, antifoam, and anti-scalent additions, is often applied to the feed stream, in addition to the removal of suspended solids.

Therefore, at this moment, either membrane separation technologies or traditional thermal distillation technologies have their specific issues that cannot be claimed as the ideal distillation method. This situation is also the main reason that limited using artificial freshwater to solve the water resources shortage of global because the cost is still very high. In other words, there still remains a need in the art for a system and method to avoid the above issues. In addition, there remains a need for a distillation and desalination system that prevents the accumulation of non-condensable gases and avoids surface scaling or fouling associated with current systems, as well as improves efficiency of thermal energy utilization.

CHAPTER 2

THE DESIGN OF OUR TECHNOLOGY

2.1 Design Target

In this project, an innovative membrane-free actively vacuumed multi-stagger stages distillation technology is proposed for overcoming all mentioned common drawbacks in the last chapter of previous attempts and current systems (membrane distillation and thermal distillation) and also adds several other benefits not found in current systems.

Specifically, our technology uses thermal distillation to get rid of requirements of membranes and obtain a larger treatment range; our technology introduced an actively vacuumed distillation process to realize a fast and highly efficient fash distillation, in which the boiling point is deceased due to the depressurized environment hence the system can be powered by low grade energy such as waste heat; in our technology the flash distillation is realized by polydispersed spray, in which the evaporation rate and efficiency are greatly increased and hence the system can be more compact; a multi-stagger stages arrangement is adopted in our system in order to independently control the operating condition of each evaporator and achieve a better thermal performance of the system.

In summary, the advantages of our technology are realized by three unique features: (1) the active vacuum extraction of vapor; (2) the polydispersed spray flash distillation; (3) the multi-stagger stages system arrangement.

2.2 Systematic Design

In order to explain the systematic design of our technology in a clearer way, first we need to exhibit an internal evaporation-condensation design within a stage to introduce a curial actively vacuumed spray flash distillation process, which is the fundamental process that uniquely existed in our technology for achieving advantages compared to current systems. Such an evaporation-condensation processing unit is schematically presented in Figure 2.1.

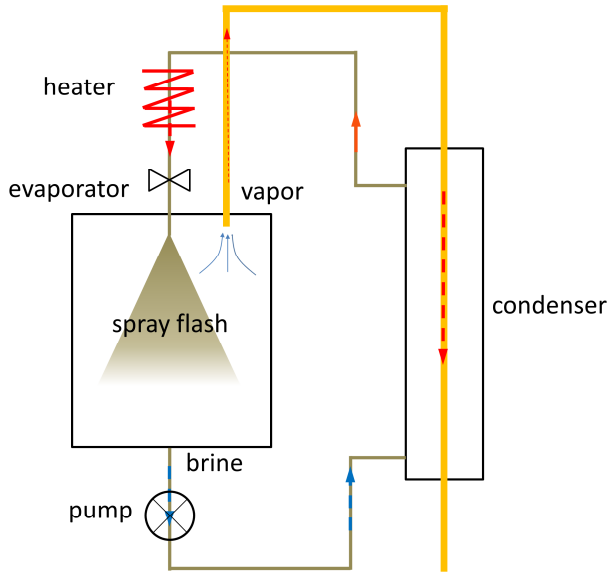

Figure 2.1. The evaporation-condensation processing unit of our technology.

In Figure 2.1, the evaporation-condensation process unit consists of one evaporator and one condenser. The brown path is brine circulation, and the orange path is vapor path. The distillation process is realized by a unique actively vacuumed spray flash evaporation, in which an active vacuum source is directly connected with the evaporator through the orange path to realizing both vacuuming and vapor extraction. The brine, circled within this unit via a cyclic pump following the brown path, is heated by an external heat input (or heater) before entering the evaporator. In each evaporator, spray nozzles are installed

for realizing an atomized spray from the brine inlet. Once the superheat brine is sprayed into this depressurized environment, a spray flash evaporation process will occur. Uniquely, for this kind of high thermal non-equilibrium spray flash process realized by active vacuuming, a temperature gap will form between yield hotter vapor and cooler spray residue (this process will be explained and studied in latter sections). As a result, heat recovery can be further achieved via a condenser between the hotter outlet vapor and cooler outlet brine. As shown in Figure 2.1, the circulated brine will recover some heat from the yield vapor in the condenser for better energy efficiency.

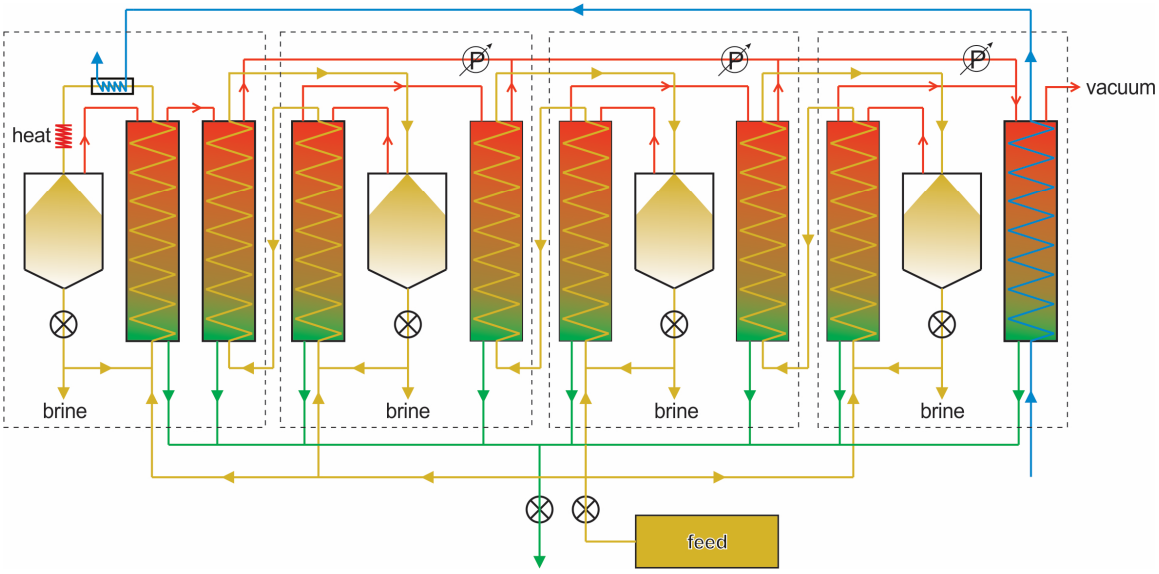

Figure 2.2 An exemplary four-stage actively vacuumed spray flash distillation system.

Now, a schematic diagram of our technology is exemplarily presented in a four-stage system as Figure 2.2, which consists of four of such an evaporation-condensation unit. The stage is defined by the vapor path of each evaporation chamber before entering the final condenser. In this figure, each stage is indicated by a black-dash frame, as one to four from left to right. The brown paths are brine circulations, which are driven by a pump

after the evaporator. The red paths are vapor paths, which are extracted by the vacuum source. For each stage, there is one evaporator and two condensers. The entire system is powered by a heating input in the first stage, located in the brine circulation right before the first evaporator. Next, the yield vapor via the spray flash evaporation process will be extracted out following the red path and go through two condensers within the stage for heat recovery. Except for the first condenser used for the internal heat recovery within the stage, as explained previously, the second condenser is for realizing an inter-stage heat recovery, in which the heat from hotter vapor is released to the cooler brine as an external heat input for the next stage. As we can see, instead of a serial stage arrangement in current systems, all stages are arranged parallelly in our system and connected with the same vacuum source to realize the active vacuuming for each stage. The green path is the path of yield water, which is obtained by vapor condensation in each condenser. Please be noticed, unlike the first three stages, the second condenser in the last stage is the final condenser that collects the vapor residue from all stages and is connected with an open-flow coolant to make sure a full condensation of any vapor residue. The stages between the first and the last stages are the inter-stage, which are identical with each other. Theoretically, more stages we have, better thermal efficiency the system will be.

The system and method for distillation and desalination of the current design provides many benefits. The vacuum vaporization distillation process disclosed herein is a thermal distillation where a vacuum is used to reduce the temperature needed for water to vaporize, without the use of membranes. The disclosed system not only is structurally simple and scalable but also requires no expensive replacement parts such as membranes and pre-filters required in other systems like Membrane Distillation (MD) and Reverse

Osmosis (RO) systems. In addition, the present invention may use only low-temperature energy resources for low pressure steam generation. Thus the system is cost efficient in both facility and operation.

Furthermore, the disclosed vacuum vaporization distillation and desalination system and method are also a thermal distillation process. In one embodiment, the process employs interconnected paths for active vapor extraction in each and every stage by a vacuum system. This active vacuum operation prevents the accumulation of non-condensable gases in each stage by removing the unwanted non-condensable gases through the vapor paths. The disclosed process also uses atomized spray under a depressurized environment to vaporize liquid in space without surface contact. This avoids the surface scaling or fouling problem. With active vapor extraction, the locally superheated atomized droplets are the heat source for the latent heat of vaporization, instead of exchangers or heaters, and residue droplets from the spray release latent heat and cool down during vaporization. The active vapor extraction also promotes a non-thermal-equilibrium vaporization process during which the vapor generated and residue droplets eventually possess different averaged temperatures. The temperature difference between the vapor generated and residue droplets is larger than the temperature difference produced in a thermal-equilibrium vaporization process, which makes the self-condensation (i.e., vapor condensed by cooling from residue droplets), an extra-distillation, that is feasible within the same vaporization process.

In addition, the disclosed system and method for distillation employs a vacuum source for active vapor extraction during the distillation process. For example, while commercial vacuum pumps may serve as the source of vacuum, a system and method for

multi-level vacuum generation and storage has an integrated system to take full advantage of ability to operate with low-quality energy source for quietly generating a vacuum. The heat produced during vacuum generation for distillation as well as the benefit of scalability is also an advantage. The condensation-induced vacuum technology disclosed therein operates with steam generated from a steam boiler or waste steam from other applications. Since the steam for generating the vacuum with this technology only needs to be saturated at a slightly-above atmospheric pressure, solar or wind generated power or heat from other green energy and waste heat resources could be used for producing the steam.

The latent heat of the source steam is recovered through coolant used in the vacuum generation. This latent heat is the heating source in the disclosed distillation system. Furthermore, the disclosed system requires no expensive replacement parts (i.e., such as membranes and pre-filters required in MD and RO systems). In addition, the disclosed system has the benefit of using only low-temperature energy resources for low-pressure steam generation as well as having a high operation tolerance to the variety of distillation solutions (e.g., alkaline or acidic fluids) or even slurries with fine solids.

However, in order to realize this design concept and develop the technology, we have to first obtain a better understanding of two curial processes involved in this system, namely as, 1) highly non-equilibrium spray flash evaporation process for realizing distillation; 2) non-linear pressure drop process of vapor condensing within the condenser. Next, based on the processes studies, we further build an overall systematic model for system optimization and scale-up study.

CHAPTER 3

HIGHLY NON-EQUILIBRIUM SPRAY FLASH EVAPORATION

The highly non-equilibrium spray flash evaporation under active vapor extraction is the most fundamental process in our proposed spray flash distillation system. In this section, a modeling and experimental study regarding this curial spray flash evaporation and its processing characteristics are performed to achieve a better understanding of the physical mechanism of our distillation process.

The spray flash an intense phase-changing process with great potential in efficient low-temperature evaporation and high evaporation capacity. In a vacuuming spray flash with active vapor extraction and absence of external heating, the latent heat is self-supplied by the evaporating droplets, resulting in a temperature difference between continued cooling droplets and the hotter yield vapor along with the spray transport. Understanding such thermal non-equilibrium between vapor and droplets is curial and beneficial to desalination industry for improving evaporation efficiency and energy recovery. In this section, an integrated experiment-modeling methodology to study the spray flash and its thermal non-equilibrium under active vacuuming is established. Various effects on the spray flash, including the polydispersion of atomized sprays, the heat conduction coupled evaporation of droplets, as well as the non-uniformity in vapor transport, are discussed. The proposed methodology is based on a Lagrangian-Eulerian modeling approach, which is calculated by a simplified process model. Two experimental systems are developed: One is for calibrating droplets' velocity and size distribution; the other is a lab-scale vacuum spray flash system for measuring the evaporative characteristics. The process model meets

good agreements with experiments. Case studies of the operation parametric effects on flash characteristics are demonstrated via both modeling predictions and experimental measurements. The results indicate that the temperature difference between the extracted vapor and the discharged water can be effectively generated during the process. Such a gap is positively impacted by the operating vacuum level and the initial spray temperature. The reported thermal non-equilibrium phenomenon indicates highly efficient evaporation of spray flash in an active-vacuuming environment, and such potential can be further utilized in our desalination technology.

3.2 Introduction

Spray flash desalination is one of the most promising thermal distillation methods for solving the global water scarcity [6]–[8], in which the vapor separation is realized by the process of spray flash [9]. Therefore, studying and understanding the mechanisms of spray flash evaporation is crucial for us to improve and optimize the industrial processes of spray flash desalination.

Flash evaporation is a very fast evaporation phenomenon that occurs when a liquid medium becomes superheated due to a sudden environmental change, such as by directly contacting a superheated solid surface or by being exposed to a space of under-saturated pressure (such as a vacuum environment). However, realizing the flash evaporation by direct surface contact in the industry not only requires a superheated surface, such as heat exchanger tubes with steam superheating, but also leads to surface scaling problems that may significantly reduce the heat and mass transfer efficiency [10]. Therefore, in most industrial applications of desalination, the flash evaporation is usually generated via the

second way (in an under-saturated pressure environment) to avoid scaling problems[11]–[13], with typical modes of pool flash or spray flash [13]. Pool flash, a more traditional distillation method, can be a steady-state evaporation process with continued heating to the evaporating liquid and continued extraction of generated vapor [14]. Compared to that, spray flash is typically an unsteady-state evaporation process with continued cooling of droplets since the latent heat is mostly self-supplied from the internal energy of droplets [15]. Taking advantage of a dramatically increased specific area for evaporation in an atomized spray [16], the spray flash can achieve a much higher evaporation rate than the pool flash [9].

Specifically, spray flash in a vacuuming environment is a special mechanical process of droplet evaporation, where an atomized liquid spray is injected into a vacuum chamber whose pressure is maintained by a vacuum pump by extracting the generated vapor out of the chamber [17]. This simple spray flash has many unique advantages, including the low-temperature evaporation, high evaporation rate within a relatively compact chamber, and no scaling problems [13]. Nevertheless, such a simple process involves very complicated phase transfer and transport mechanisms, with the integrated coupling of mass, momentum, and energy among different phases of droplets and vapor under highly non-equilibrium and non-uniform transport conditions.

According to previous experimental studies in recent decades, the evaporation process in a spray flash can be affected by many spray characteristics, such as the initial temperature of sprayed droplets [18], the direction and velocity of injection [19], [20], and the spray flow rate [21]. For example, a higher level of superheating of the injected spray normally leads to higher levels of evaporating rate, amount, and efficiency. Even a spray

flash with a low level of superheating, for instance, 2°C, may also be effectively completed [20]. Likewise, a spray upwardly injected against gravity may also evaporate better than a downward one due to a longer residence time of droplets in the transport and evaporation process [20]. While the experimental studies can result a few semi-empirical correlations of some parametric effects, a comprehensive understanding and reliable quantitative predictions of the evaporation and transport characteristics of a spray flash have to be obtained from the first-principle-based mechanistic modeling.

In theory, droplet evaporation is basically governed by two coupled mechanisms: the heat transfer to the interface from the inner liquid side, and the heat and mass transfer on the evaporating interface from the gaseous ambient [22]. In the case of droplet flash evaporation of pure substance in a vacuuming environment, the evaporation rate can be limited by the heat transfer from the liquid side due to the intense heat consumption of phase change by vacuuming and no avail of heat transfer to the evaporating surface from the ambient side [23]. Although the relative motion between droplets and extracted vapor flow may cause asymmetric and enhanced convection [24], such asymmetry and enhancement can be ignored when the pressure difference between the saturated vapor-liquid phase on the evaporating surface of the droplet and the vacuuming environment is orders-of-magnitude higher than that induced from the vapor flow over the droplets [16].

So far, all evaporation models are based on the phase transfer theories under idealized conditions such as near phase equilibrium (where Chapman-Enskog theory can be applied, or Boltzmann probability distributions become valid) and ideal gas approximation for the vapor phase[22], [25]–[31]. In such approaches, the evaporation rate models are represented by the kinetic theory model [26], [32] and diffusion-controlled

model [29], whereas the evaporation heat must be provided from the coupled heat transfer models governed by the heat transfer from the vapor side (by conduction or convection) and ambient environments (such as thermal radiations), heat conduction from droplet (with or without considerations of internal motions) or a combination of all heat transfer modes. It must be noted that neither the vacuuming flash is near phase equilibrium nor the saturated vapor on the evaporation surface follows the ideal gas law. Nevertheless, there has been no better modeling available for the estimation of droplets evaporation rate in a vacuuming flash. As a result, both kinetic theory model and diffusion-controlled model have been extended into the evaporation modeling of spray flash [2], [5], [33]–[37].

A very important feature in flash evaporation modeling of an atomized spray is its polydispersion or non-uniform distributions in droplet size, droplet velocity, injection angle, as well as the number density of droplets or flow rate [4], [38], [39]. The polydispersion, especially in typically widely-distributed droplet sizes, causes a strong non-uniformity in flash evaporation via the significant differences in exposed evaporation area as well as in the transport characteristics (such as residence time) of droplets of different sizes or injection velocities [16]. Unfortunately, this polydispersion depends not only on the types of nozzles and physical mechanisms of atomization but also on the operation conditions, which leads to the nonexistence of universal modeling to predict the atomized spray characteristics at the nozzle tip or injection inlet [16], [40]. Consequently, the details in spray polydispersion have to be experimentally determined case-by-case. The polydispersion in atomized spray also imposes greater challenges to the associated evaporation and transport modeling. For example, an overall averaged equivalent diameter for hydrodynamic transport (such as the hydraulic equivalent diameter of all droplets) can

be quite different from an overall averaged surface-area equivalent diameter for evaporation. That means no single averaged diameter can reasonably reflect both hydrodynamic transport and evaporation characteristics in the modeling of an atomized spray flash. So far, most models in spray flash ignore such polydispersion for simplicity by assuming all droplets have the uniform size, mass flux, and velocity [33], [41], [42].

However, spray polydispersion may have a significant impact on the flash evaporation under certain circumstances. For example, for a spray flash in an evaporation chamber of limited dimension, some fine droplets may be able to complete their evaporation within the chamber, while larger ones may not have enough time to complete the vaporization before colliding onto the chamber boundary or exiting out of the chamber. Using a uniform size for the droplet evaporation and transport (even averaged over a droplet size distribution) may misrepresent the total surface area of evaporation or phase transfer and the non-uniformity in phase transport. Hence a proper modeling consideration is needed to account for this polydispersion effect, such as adopting a set of sub-grouped droplet sizes and mass fluxes to mimic the polydispersed spray transport. Consequently, in this study, a combined experiment-modeling methodology is established to introduce the polydispersion effect of atomized sprays and the vacuuming effect on the evaporation capacity in a spray flash, which is realized by adopting the Lagrangian approach for the discrete phase of droplets [17].

In a vacuum spray flash that is absent of external heating, the latent heat is self-supplied by the evaporating droplets, resulting in a continued decrease in droplet temperature. Moreover, with the vapor extraction by vacuuming, the extracted vapor is expected to possess a higher temperature than the remaining droplets or liquid residue.

Such a temperature difference will demonstrate such a high thermal non-equilibrium process is very efficient in evaporation, which could benefit many industrial processes such as thermal distillation. Moreover, the thermal energy in the vapor of higher temperatures could also be recovered to further improve energy efficiency [43]. However, in most industrial multi-stage flash desalination plants, the superheat level of the liquid in each evaporator remains relatively low, in which the vapor extraction is passively condensation controlled by the next stage [44]–[48]. Therefore, in this study, the evaporation chamber is directly connected with a vacuum source on purpose (named active vapor extraction) to obtain a high thermal non-equilibrium condition during spray flash. Meanwhile, this study aims to investigate such interesting thermal non-equilibrium between the extracted vapor and discharged spray residue, characterized by the temperature difference between the two, during a vacuum spray flash.

In conclusion, to study the thermal non-equilibrium phenomena existed in a spray flash with active vapor extraction, an integrated experiment-modeling methodology is proposed in this section, and several sub-tasks need to be achieved following the research logic: (1) determination of polydispersion characteristics of atomized nozzle spray; (2) establishment of an experimental system for measurements of some spray flash characteristics, which is also used for model validations; (3) development of a Lagrangian-Eulerian process model to investigate multiple parametric effects on the vacuum spray flash; (4) determination of the evaporation coefficient used in the evaporation model, which represents an empirical correction for the flash non-equilibrium and various non-uniformities in an atomized spray (such as droplet shape and size); Specifically, the polydispersed size distribution from spray atomization is experimentally determined via a

laser-scanning aided technology. The polydispersed size distribution is then implemented into the process model and CFD model as input conditions of spray. A lab-scale experimental spray flash evaporation system has been set up for the determination of the evaporation coefficient as well as model validation, in which the vacuumed evaporator is connected to a vacuum pump to realize a timely vapor extraction. The extracted vapor is condensed via external condensers and analyzed. With the evaporation coefficient empirically determined under spray flash in a vacuum, the evaporation model is then implemented into the process model.

3.3 Experimental Study

The main objectives of experiments include the measurements of total evaporation rate, the temperature of feed-in atomized spray, the temperature of extracted vapor, the temperature of liquid discharged from evaporation chamber, the temperature profile of spray flash along with the chamber height, the pressure of vacuum chamber, the flow rate of feed-in spray, as well as the atomized spray characteristics such as injection velocity and droplet size distribution.

Figure 3.1 shows a schematic diagram of the vacuum spray flash system. The main components of the system consist of a feed circulation pump (Warren Rupp double diaphragm pumps, manufacture (Mfr.) number: WR10PP6XPP9), a heater of feed heating (Vulcan immersion heater, Mfr. number: AUW250B), a nozzle (Bete Fog Nozzle, Mfr. number:1/4WL1-1/2-60) for generating atomized spray, a vacuum-maintained evaporation chamber, a feed mixer of replenished supply and spray residue, a vapor condenser, a yield chamber, and a vacuum pump. As shown in Figure 3.1, the system has two main flow

paths: the feed-spray path (marked as blue) and the vapor-condensate path (marked as dotted green). The feed is pressurized and heated-up into a flowrate-temperature regulated nozzle that is inserted into the evaporation chamber. An atomized spray is injected from the nozzle into the evaporation chamber, where spray flash is formed due to the significant pressure differences between the super-saturated droplets and the depressurized environment. The evaporation chamber is thermally insulated, with ports of vapor extraction and spray residue discharge. The discharged spray residue from the evaporation chamber is mixed with replenished feed in the mixer (with a discharging port for the optional discharge of some or all feed residue) and then recirculated, through the pump and heater, back to the nozzle. The vapor, generated from spray flash, is extracted into a condenser where the vapor condensate is collected. The evaporation chamber, vapor-condenser, and a vacuum-regulator are connected in series to the vacuum pump. Coolant flow is used to ensure sufficient heat removal and hence vapor condensation in the condenser. An insignificant amount of non-condensable gases (NCG), degassed or co-vaporized from spray flash, cannot be condensed by the condenser and hence are extracted into the vacuum pump and discharged into the ambient.

In this study, the temperature measurements are based on thermocouples and thermocouple profile probe. The temperature profile probe (Omega ten sensing type k thermocouple profile probes) measures the temperature distribution (along the probe direction) during the spray flash process[9], [18]. The pressure measurements are obtained using vacuum pressure gages (IFM pressure sensor, model number: PG2794). The flow rates of inlet spray and feed replenishment are regulated by flow meters (IFM efector magnetic inductive flow meter, model number: sm6004). The feed heating is maintained

by an electric-powered heater. To reduce the surface scaling and limit the amount of NCG, regular tap water is used as the feed liquid, which is also helpful for the model validation since the feed is now a single-component condensable liquid without the complication in concentration-related concerns.

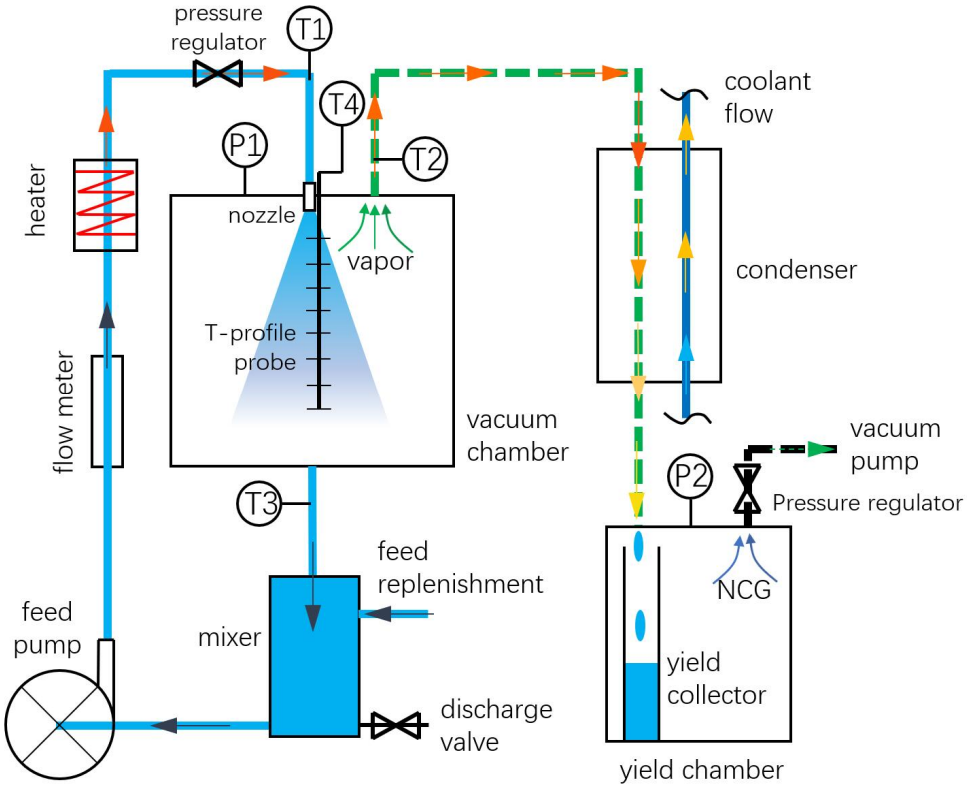

Figure. 3.1 Schematic diagram of vacuum spray flash system.

For a spray flash, the atomization characteristics from a nozzle spray majorly depend on two curial parameters, Weber number and Reynolds number, respectively representing the surface tension and the viscous effects with respect to the inertia effect [49]–[54]. Specifically, it will strongly depend on the type of nozzle, the feed liquid, and various operating conditions, including the nozzle pressure, ambient pressure, flowrate, and feed temperature in our case [16]. Hence, the atomization characteristics such as

polydispersion are highly case-sensitive. In this study, we have developed a spray measurement system, which is based on combined concepts of laser marked shadowgraphy (LMS) [55], paralleled laser sweeping (PLS) [56], and particle image velocimetry (PIV) [40], [57].

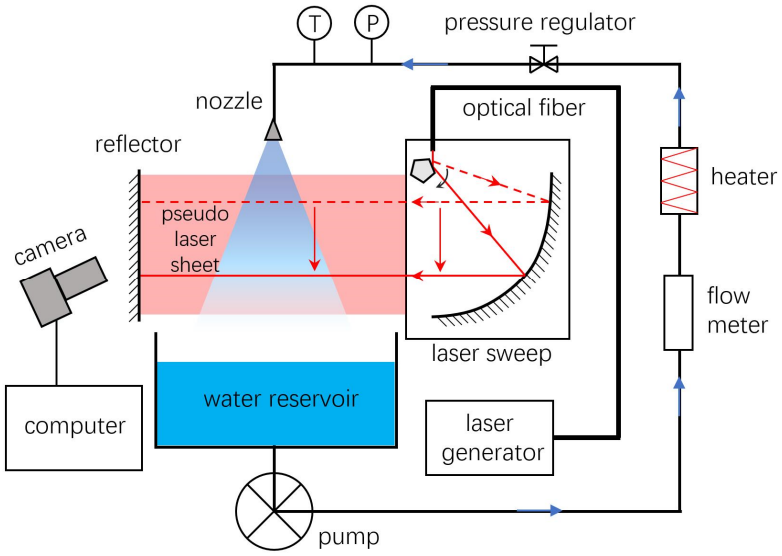

Figure 3.2 Schematic experimental system for characterizing atomized spray.

Figure 3.2 shows a schematic diagram of the experimental system for characterizing atomized spray. An atomized spray is illuminated by a pseudo-laser-sheet, which is further enhanced by a reflector normal to the laser beam. This pseudo laser sheet is formed by a vertically sweeping laser beam from a laser scanner with a high sweep frequency [56]. The laser sheet is arranged crossing the medium vertical plane of the spray. The images of droplets within the illumined volume of a laser beam are recorded by a digital camera, as shown in more detail in Figure 3.3. The feed spray is preheated by a heater and regulated by a pressure regulator. The pressure drop across the nozzle spray is

measured by a differential pressure gauge, whereas the feed spray temperature and flowrate are measured, respectively, by a thermocouple and a rotameter.

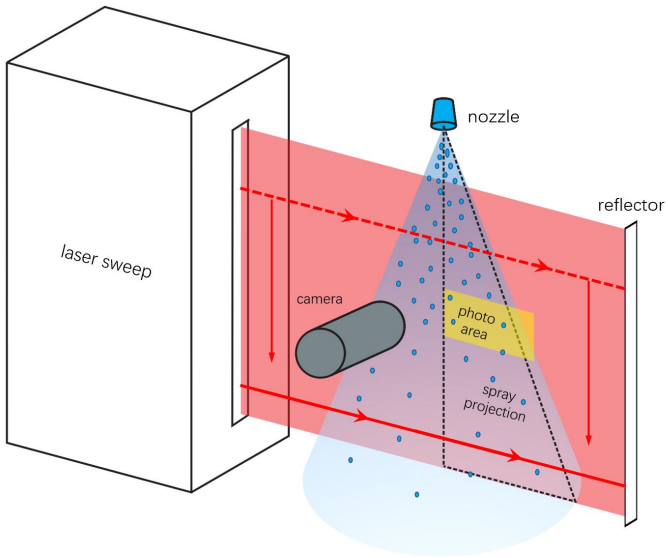

Figure 3.3 Laser-sweeping-aided particle image system.

Similar to the droplet-marking principle in LMS [55], [58], a targeted droplet can be marked with glaring points by a laser beam with reflection. The image is pre-calibrated by a scale located on the laser sheet, and once the marked droplet is obtained, the size will be determined based on pixel analysis. The sizes of these laser-marked droplets can thus be determined through the recorded high-resolution images. It should be noted that a string of multiple exposures of the same droplet in a recorded image can also be used to determine the velocity of the droplet. The difference between the size photographing and the velocity photographing of droplets is how to coordinate the expose time of the camera and the sweep frequency of the laser beam. For size determination, the exposure time of the camera must be short enough to capture a sharp image, meanwhile it still needs to be long enough for the laser beam to finish one sweep of the view field. For velocity determination, the

exposure time becomes non-critical, however the sweep frequency should be faster enough to sweep over multiple times of the tracked droplet during the exposure.

In our case, the laser beam is generated by Laser Physics Reliant 1000m argon laser, and the laser sweep is realized by Optical Flow System laser sweeper (Model: SCN-CN2A). The photography area (marked as yellow zone in Figure 3.3) by the camera (Canon EOS 6D Mark II) is located at 139-259mm along the vertical direction (defining nozzle exit is 0), and 0-179mm along the horizontal direction (defining spray central axis is 0). Figure 3.4 illustrates an example of captured images of laser-marked droplets for helping further explanation. Here the red spots are the mark point on the droplet by laser (Helium-Neon in this case). Figure 3.4(a) shows a string of five images of a droplet, with the camera exposure time is five times longer than the sweep period of the laser. This original image is captured in the dark environment, but the background color is inverted for a better presentation. During this exposure time, any droplets moving vertically along the sweeping plane will be highlighted five times by the laser beam, and generate a string of five highlight points in the digital picture recorded. Thus, based on the camera shutter speed, laser scanning period, and inter-point distance (or numbers of pixels covered), the instantaneous velocity of the droplet can be obtained. The average droplet velocity of the spray is determined by averaging multiple sets of data from different trajectories. Figure 3.4(b) shows a case with the camera exposure time is about the same as one period of the laser sweep. In that case, any droplets on the laser sheet are highlighted only one-time by the sweeping laser beam. Such an image is used for droplet size determination. In Figure 3.4(b), two red spots are identified by circled marks. It is noted that many unfocused droplets represent the ones outside either the laser sheet or the focal zone of the camera.

Assuming the spray is steady-state, we can take many images for the determination of droplet size distribution.

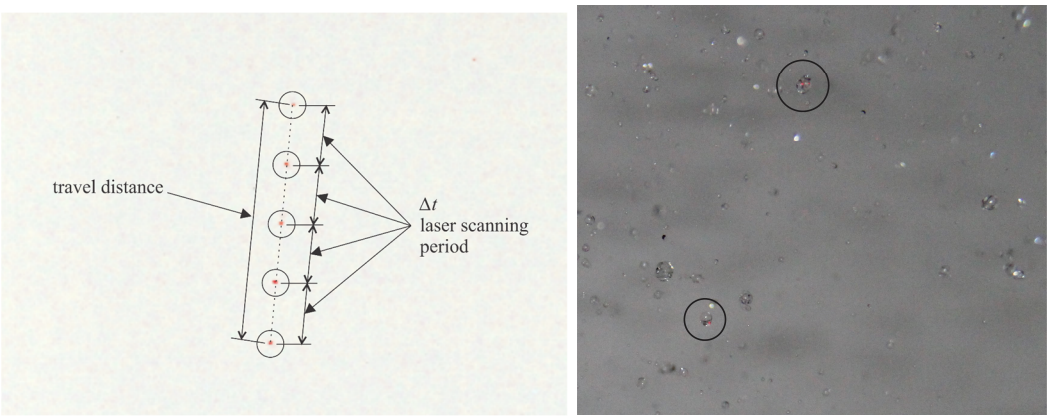

(a) a string image of a droplet trajectory (b) images of multiple droplets

Figure 3.4 Examples of images from spray measuring system.

3.4 Vacuum Spray Flash Model

The modeling of spray flash aims to quantify various parametric effects and process characteristics on the spray evaporation, which is crucial to optimize the design and operation of the spray flash system. The key parameters include the atomized spray characteristics (such as droplet size/velocity distribution and mass flowrate), geometric system arrangements (such as chamber shape, size and orientation, spray nozzle insertion, ports of vapor extraction, and liquid discharge), as well as operating conditions (such as spray temperature and vacuuming pressure).

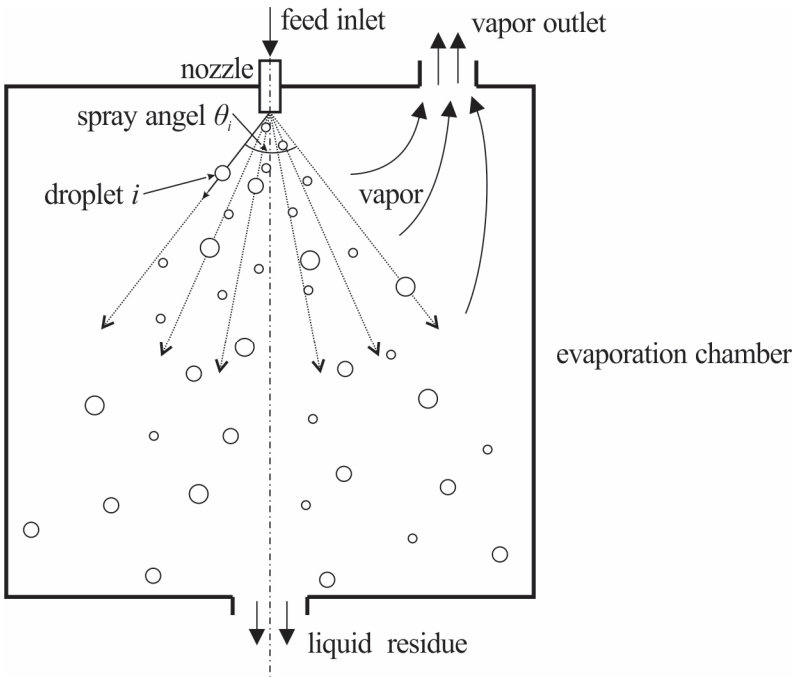

Figure 3.5 Schematic droplet-vapor transport in a vacuum spray flash.

Spray flash is a droplet-vapor two-phase flow transport, with intense non-equilibrium phase changes (evaporation). In spray flash, the specific sensible heat change is typically at least two order-of-magnitude smaller than the specific latent heat [22]. For atomized spray of high inertia (such as of large droplet size and/or high injection velocity), the droplet transport is dominated by the droplet inertia from initial nozzle injection, with minor influences of droplet-vapor interactions (especially in a vacuuming environment) and droplet-droplet interactions (due to fast dispersion and a tiny volumetric fraction of droplet phase in the droplet-vapor flow), as schematically described in Figure 3.5. In the vacuum spray flash, the vapor phase is solely formed from spray-dispersed droplet evaporation. Hence, the vapor flow is governed by the spatial distribution of vapor generation sources (from both droplet transport and accompanied evaporation) as well as by the vacuuming extraction.

In the two-phase flow modeling of vacuum spray flash, it is convenient to adopt a hybrid Lagrangian-Eulerian approach, in which the droplet transport is described by Lagrangian trajectory modeling (starting from the nozzle tip). Meanwhile, the vapor flow is described in an Eulerian framework (bounded by the evaporation chamber). The Lagrangian model yields the spatial dispersion of sprayed droplets and results in the spatial distribution of vapor generation rate, which are implemented into the Eulerian equations of vapor flow. For simplicity, in the Lagrangian model, the interactions of droplet-droplet and droplet-wall are ignored, and the droplet trajectory is assumed to be predetermined based on droplet inertia.

3.4.1 Lagrangian Model of Individual Droplets

While the disintegrated elements in an atomized liquid spray can be highly non-spherical at the initial nozzle injection [59], the surface tension will quickly contract the elements into droplets[60]. For simplicity, we ignore this initial-stage of non-sphericity and assume all droplets are spherical without breakup or coalescence during their transport.

In the Lagrangian model, the dynamic motion of an individual droplet is governed by the overall momentum transfer to the droplet. Conceptually, these momentum transfer terms include the drag force, gravity, buoyancy, and forces due to acceleration such as added mass force and Basset force [61]. However, due to the large density ratio of the droplet to vapor (about 10^3), the buoyancy, added mass force, and Basset force are negligibly small compared to the drag force. Hence, the equation of motion of i^{th} droplet is expressed by:

$$\frac{d\left(m_{di}\mathbf{u}_{di}\right)}{dt} = m_{di}\mathbf{g} + C_{Di}A_{di}\frac{\rho_v}{2}\left|\mathbf{u}_v - \mathbf{u}_{di}\right|\left(\mathbf{u}_v - \mathbf{u}_{di}\right) \tag{3.1}$$

where the subscript "*i*" denotes the i^{th} droplet, m_d is the mass of droplet; $\boldsymbol{u}_d$ and $\boldsymbol{u}_v$ denote, respectively, the droplet and vapor velocities; $\boldsymbol{g}$ is the gravitational acceleration; C_D is the drag coefficient; A_d is the cross-sectional aera normal to the droplet trajectory; and ρ_v is the vapor density.

At high droplet Reynolds number (*e.g.*, $30 < Re_{dm} < 200$), with the correction of evaporation [22] and the Hadamard-Rybcyznski correction of a fluid particle [62], the drag coefficient C_d can be estimated by:

$$C_d = \frac{24.432}{\mathrm{Re}_{d,m}^{0.721}}\left(1+\frac{c_{p,m}(T_v - T_d)}{h_{fg}}\right)^{-0.27}\left(\frac{3\mu_d + 2\mu_{v,m}}{3\mu_d + 3\mu_{v,m}}\right) \tag{3.1a}$$

where h_{fg} is the latent heat; $Re_{d,m}$ is the droplet Reynolds number, modified with the vapor film viscosity $\mu_{v,m}$, and is defined by:

$$\mathrm{Re}_{d,m} = \frac{\rho_v d_d}{\mu_{v,m}}\left|\mathbf{u}_d - \mathbf{u}_v\right| \tag{3.1b}$$

The droplet diameter d_d is related to the droplet mass m_d by:

$$m_d = \rho_d \frac{\pi}{6} d_d^{\,3} \tag{3.2}$$

The change rate of droplet mass is determined from the evaporation rate of the droplet:

$$\frac{dm_d}{dt} = -\dot{m}_v \tag{3.3}$$

In vacuum spray flash, the evaporation rate is governed by the pressure difference between the saturated vapor pressure at the droplet surface and the ambient pressure controlled by vacuuming. Hence, assuming no temperature slip over the droplet interface (*i.e*, surface vapor temperature is the same as the surface droplet temperature), the evaporation rate could be determined from the modified Hertz-Kundsen relation [26]:

$$\dot{m}_v = \alpha \pi d_d^{\,2} \sqrt{\frac{M_v}{2\pi R_u T_{d,s}}} \left(P_{sat} - P_\infty \right) \tag{3.4}$$

where α is the evaporation coefficient (which is a case-sensitive empirical constant to be determined from the experiment), M_v is the molecular weight of the vapor, R_u is the universal gas constant of ideal gases, P_{sat} is the saturated vapor pressure at droplet surface, P_∞ is the ambient pressure, and T_{ds} is the droplet surface temperature. With the further approximation of ideal gas for the saturated vapor and the gas phase only consists of evaporated vapor, the saturated vapor pressure can be related to the droplet surface temperature by Clausius-Clapeyron equation [63]:

$$\ln \frac{P_{sat}}{P_\infty} = -\frac{h_{fg} M_v}{R_u} \left(\frac{1}{T_{d,s}} - \frac{1}{T_\infty} \right) \tag{3.5}$$

where T_∞ is the saturated temperature at P_∞. Alternatively, in order to account for the non-ideal gas behavior of saturated vapor, Equation (3.5) can be replaced with an empirical correlation of the corresponding pressure and temperature of saturated vapor for better or more realistic modeling.

The droplet surface temperature is determined from the overall heat transfer to the droplet surface for the latent heat required by the flash-induced evaporation. In the absence of external heating, especially under convective cooling due to lower ambient temperature, the latent heat for the droplet evaporation has to be derived from the thermal energy of the droplet itself. Assuming the heat conduction within the droplet is spherically-symmetric, the heat conduction equation within the droplet can be expressed in the spherical coordinate:

$$\frac{\partial}{\partial t} \left(\rho_l c_l T_l \right) = \frac{1}{r^2} \frac{\partial}{\partial r} \left(r^2 k_{eff} \frac{\partial T_l}{\partial r} \right) \tag{3.6}$$

where r is the radial coordinate centered in the droplet, T_l is the time-dependent local liquid temperature within the droplet, c_l is the specific heat of the liquid, and k_{eff} is the effective thermal conductivity in flash evaporation [64]:

$$k_{eff} = 1.86k + 0.86k \tanh\left[2.245 \log_{10}\left(Pe/30\right)\right] \tag{3.6a}$$

where k is the molecular conductivity, and Pe is Peclet number of the droplet. The initial condition is given by spray temperature at nozzle injection:

$$T_l(r,0) = T_{d,0} \tag{3.6b}$$

The boundary conditions are given by the symmetric condition at the droplet center and heat transfer balance at the droplet surface, respectively expressed as:

$$\frac{\partial T_l}{\partial r} = 0 \qquad at\ r = 0 \tag{3.6c}$$

$$\pi d_d^2 k_{eff} \frac{\partial T_l}{\partial r} = -h_{fg}\dot{m}_v + h_m \pi d_d^2 (T_v - T_l) \qquad at\ r = \frac{d_d}{2} \tag{3.6d}$$

where h_m is the convective heat transfer coefficient, which may be approximated using Ranz and Marshall correlation with vapor-film properties and relative droplet velocity [63]. In which the Nusselt number is determined by:

$$\overline{Nu}_d = 2 + 0.6 \mathrm{Re}_{d,m}^{1/2} \mathrm{Pr}^{1/3} \tag{3.6e}$$

Thus, the Lagrangian model of a droplet flash and transport is established. With six governing equations (Equation (3.1) – Equation (3.6)) for six unknowns (m_d, $\boldsymbol{u}_d$, d_d, T_l, P_{sat} and m_v), the problem is closed.

The hydrodynamic transport and evaporation of different-sized droplets, predicted by the individual droplet evaporation model, can behave quite differently. In a vacuum chamber, the smaller droplets are likely to achieve higher evaporation completeness due to

a larger specific surface and longer time duration, and the larger droplets will have less evaporation completeness. As a result, using one average droplet size (such as Sauter mean diameter) to simulate polydispersed spray evaporation may result in a severely biased estimation of the overall evaporation rate. Therefore, in the Lagrangian modeling of a polydispersed spray, droplets are sub-grouped into N size-based groups (i.e., droplets in the same group will have similar sizes) according to the droplet size distribution, which helps to account for this polydispersion effect on the spray transport and evaporation.

3.4.2 Eulerian Model of Vapor Flow

One of the major objectives of this study is to estimate the extracted vapor temperature and other vapor transport properties. The vapor flow is modeled using the Eulerian approach, with the coupling of evaporating sprays from the Lagrangian trajectory model. It is assumed that the droplets are treated as point sources in the vapor flow so that the volumetric effect of droplets is ignored in the vapor flow.

The mass conservation equation is given by:

$$\frac{\partial \rho}{\partial t} + \nabla \cdot (\rho \mathbf{u}_v) = S_m \tag{3.7}$$

where the S_m is the vapor generation rate per volume, which is the sum of individual vapor generation rates of all droplets within the control volume V_{cell}. For a polydispersed spray, S_m can be expressed by:

$$S_m = \frac{1}{V_{cell}} \left(\sum_{j=1}^{N} \sum_{i=1}^{N_j} \dot{m}_{v,ij} \right) \tag{3.7a}$$

where subscripts i and j denote the i^{th} droplet of j^{th} size group (or on j^{th} trajectory), N_j is the total number of droplets of j^{th} size-group within V_{cell}, N is the total number of

droplet size groups, and m_v is the evaporation rate of an individual droplet which is previously solved from the Lagrangian model. N_j depends on the local number density of droplets of group j, n_j, by:

$$N_j = V_{cell} n_j \tag{3.7b}$$

Assuming there is no droplet breakup or coalescence, the mass conservation leads to a droplet number density conservation, which is expressed by:

$$\nabla \cdot \left(n_j \mathbf{u}_j \right) = 0 \tag{3.7c}$$

The momentum conservation equation is given by [65]:

$$\frac{\partial}{\partial t}\left(\rho \mathbf{u}_v \right) + \nabla \cdot \left(\rho \mathbf{u}_v \mathbf{u}_v \right) = -\nabla p + \nabla \cdot \left(\left(\mu + \mu_T \right) \nabla \mathbf{u}_v \right) + \rho \mathbf{g} + \mathbf{F}_{vd} \tag{3.8}$$

Where the $\boldsymbol{F}_{vd}$ is the droplet-vapor momentum transfer per volume, which is roughly approximated by the sum of individual drag forces of all droplets within the control volume V_{cell}. For a polydispersed spray, $\boldsymbol{F}_{vd}$ can be expressed by:

$$\mathbf{F}_{vd} = \frac{1}{V_{cell}} \left(\sum_{j=1}^{N} \sum_{i=1}^{N_j} \mathbf{F}_{ij} \right) \tag{3.8a}$$

where $\boldsymbol{F}_{ij}$ is given by:

$$\mathbf{F}_{ij} = C_{d,ij} A_{d,ij} \frac{\rho_v}{2} \left| \mathbf{u}_{ij} - \mathbf{u}_v \right| \left(\mathbf{u}_{ij} - \mathbf{u}_v \right) \tag{3.8b}$$

The energy equation is approximated by [65]:

$$\frac{\partial}{\partial t}\left(\rho c_p T_v \right) + \nabla \cdot \left(\rho c_p \mathbf{u}_v T_v \right) = \nabla \cdot \left(\left(K + K_T \right) \nabla T_v \right) \tag{3.9}$$

The equation of state is given by:

$$P = \rho_m R_u T_v \tag{3.10}$$

The turbulent viscosity μ_T can be determined by a turbulence model, such as the k-ε model. The turbulent thermal conductivity K_T can be related to μ_T by gas kinetic theory.

Thus, for the Eulerian model, there are four independent equations (3.7-3.10) matching four independent variables (ρ, $\boldsymbol{u}_v$, p and T_v), which can be solved by coupling with the Lagrangian model of droplets.

3.5 Results and Discussion

In the following, a case study accompanied with both theoretical calculations and experiments is used to illustrate some unique characteristics and effects in a vacuum-assisted spray flash, including the spray polydispersion and its impact on flash evaporation rate, the operational parametric effects (initial temperature and operating pressure) on the spray flash, and the non-uniform phase distributions of spray flash inside the evaporation chamber. The basic operational and geometric information is summarized in Table 2, with a basic system layout schematically described in Figure 3.1. The heat losses via the chamber to the ambient are insignificant (less than 1%), judged by the experimental estimation of enthalpy imbalance between the inlet feed and outlets of vapor and liquid.

Table 3.1 Key Geometric and Operational Parameters

Parametric	Value	Unit
Spray nozzle	Full-cone	-
Spray angle	57	°
Nozzle location	Top center	-
Spray injection velocity	3.23	m/s
Spray liquid	water	-
Spray flow rate	44.1	ml/s

Table 3.1 Key Geometric and Operational Parameters (continued)

Chamber height	0.5	m
Chamber diameter	0.3	m
Vapor outlet diameter	0.75	inch
Liquid outlet diameter	0.5	inch
Spray initial temperature	70 - 100	°C
Chamber vacuum pressure	0.25 - 0.8	atm
Chamber material	Stainless steel with insulation	N/A
Thermal resistance of chamber	2.16	$K \cdot m^2/W$

3.5.1 Polydispersion Effect

The most important polydispersion characteristics of a liquid spray is the co-existence of various initial droplet sizes, typically by a simultaneous liquid breakup from the combined actions of jet-induced shear-tearing and turbulent instability[38], [52]. Due to the lack of reliable modeling and complexity in various nozzle design [59], operation conditions, and liquid properties, the droplet size distribution is mostly determined via experimental means, such as using the laser-sweeping aided photographic system in Figure 3.3. Because the spray needs to be determined as the initial condition, measurements were performed in a normal room-environment in order to minimize the effect of intense evaporation on droplets sizes [66], [67]. As mentioned in Table 3.1, the only major variable in our case that influences polydispersion characteristics between each different operating condition is the different spray initial temperature, which might noticeably affect temperature-dependent physical properties of the surface tension and the viscosity [38]. Therefore, the droplet size distribution has been calibrated for specific operations distinguished by the inlet spray temperature. Based on the experimental results and previous work, the experimental data are most likely to be best-fitted (by using the least-square method) into

a Rosin-Rammler size distribution [38], [68], [69], which is expressed in terms of probability density function(PDF) by

$$f(d)=\frac{\kappa}{\delta}\left(\frac{d}{\delta}\right)^{\kappa-1}\exp\left(-\left(\frac{d}{\delta}\right)^{\kappa}\right) \tag{3.11}$$

where κ and δ are two fitting parameters, respectively for shape and scale.

In this work for all cases, a full cone spray nozzle without swirling (Bete 1/4WL1-1/2) is used, with a water flow rate of 44 ml/s under a specific temperature. Figure 10 illustrates an example of droplet size distribution corresponding to the operation of 94°C initial spray temperature (used in model validations and CFD), which is obtained from an analysis of 933 measured droplets (similar to those in Figure 4). The droplet size range is shown to be between 0.4 and 2.0 mm, with κ=4.432 and δ=1.099.

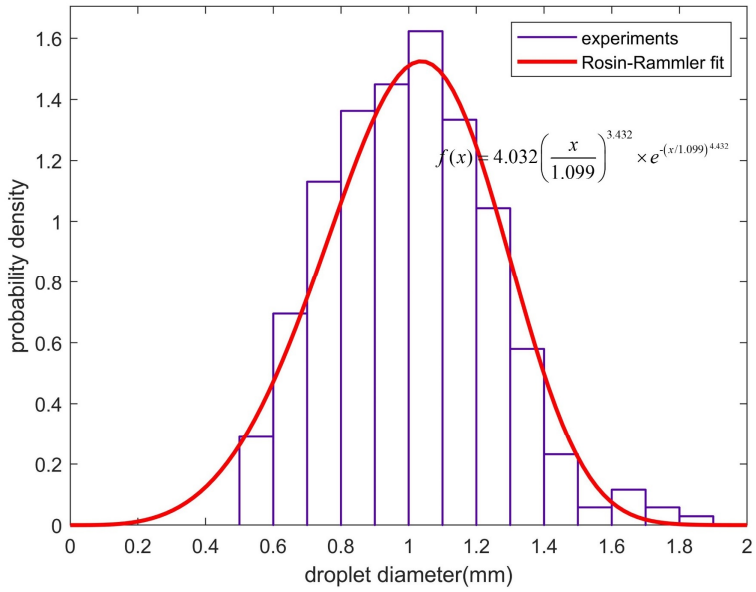

Figure 3.6 Example of the PDF of droplet sizes.

3.5.2 Operation Parametric Effects

One of the most important objectives of this study is to investigate the thermal non-equilibrium or temperature difference between the extracted vapor and the liquid residue after a vacuum spray flash process. Such thermal non-equilibrium is most likely to be affected by the key operation conditions, including the initial spray temperature and the ambient vacuum pressure inside the evaporation chamber.

For the parametric analysis, the Lagrangian trajectory model described in Section 3.3 may be approximated by simplifying the droplet-vapor phase interactions, i.e., assuming the vapor is moving up uniformly within the chamber. This simplification is justifiable under the current case study, in which the cross-section averaged vapor velocity (e.g., less than 0.04 m/s) is much less than the spray velocity (e.g., about 3.3 m/s), and the calculation of our model indicates the convective heat transfer is at least four orders-of-magnitude smaller than the latent heat transfer during the droplet evaporation. Such a simplification enables the spray model to be directly solvable without considering the cross-sectional non-uniformity of the vapor phase, which is adopted as the process model in this paper.

The effects of inlet spray temperature and pressure in the vacuum chamber on the temperatures of extracted vapor and water residue is shown in figures 3.8 and 3.9, with the inlet spray temperature varying from 70 to 100 °C and the operating pressure varying from 25 to 80 kPa, respectively. Each experimental data is averaged from six sets of measurements, with the error bar indicating the standard deviation of the group. Since the theoretical results are calculated case by case, the dash-line interlinked each point is just for showing a tendency instead of a real continued result curve.

Figure 3.8 shows at the same inlet spray temperature, a higher operating pressure (or lower vacuum level) will result in a narrower temperature difference between vapor and water, which means the thermal non-equilibrium level (temperature gap) is positively related to the superheat level of the spray. Under the same vacuuming pressure, the vapor temperature increases linearly with the inlet spray temperature while the water residue temperature remains close to the equilibrium temperature, which also indicates the evaporation process is nearly completed in all cases. However, we can see the temperature difference can be effectively generated even under a low superheat level of the spray, which indicates the process of spray flash with active vapor extraction is highly efficient in evaporation (discharged heat from hotter vapor to cooler droplets during the process is little). The result presents quantitative relations between superheat level of the spray and thermal non-equilibrium level of the two phases. Such a relation will be a very critical parameter for desalination system design if the heat is expected to be further recovered from hot vapor to cool residue via a heat exchanger, in which the heat recovery efficiency has to depend on that temperature difference.

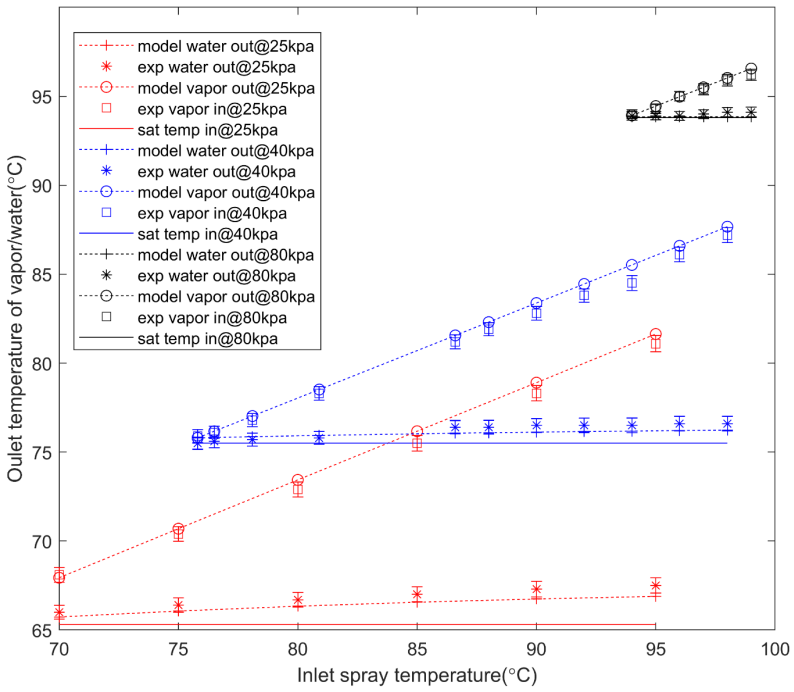

Figure 3.8. Effects of spray inlet temperature and operating pressure on temperatures of extracted vapor and water residue.

Figure 3.9 shows the superheat of the droplets (T_{in}-T_{sat}) and the temperature difference ($T_{v,o}$-$T_{w,o}$) follow a linear relationship based on modeling and experimental results. The slopes of different operations are quite close to each other, with an average value of about 0.47. The tiny variations on the slopes of each operation are appeared due to the non-linear relation between the saturated pressure and temperature of the water/vapor. We can also notice the deviation between experiments and modeling predictions increases with rising the superheat degrees of the spray, in which the experimental measurements are lower than computational results. Such errors may be caused by enhanced local mixing of heat and mass between the two phases, which cannot be fully considered by this simplified process models.

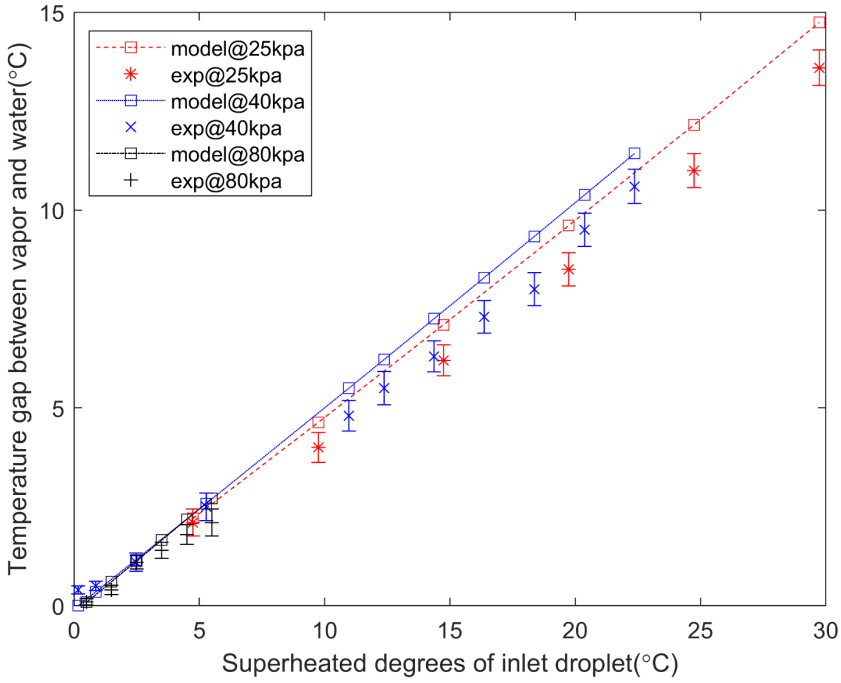

Figure 3.9 Superheat level vs temperature difference of two exit phases.

It is noted that the stronger superheating of spray means a bigger pressure difference between the saturated vapor from droplet evaporation and the vacuuming environment. Due to such significant non-equilibrium in pressure, the evaporative coefficient α in Equation (4) needs to be calibrated since the evaporate rate equation is derivated from the assumption of pseudo-equilibrium. Based on the experimental results of the case of 60 kPa, the α is calibrated as 0.01. Assuming the evaporation coefficient remains unchanged within the vacuuming range in this study, the modeling predictions on the droplet temperature distributions along with the chamber centerline (where a multi-point thermocouple probe is located) can be compared to the measured temperature profile, as shown in Figure 3.10. The good agreement between the modeling predictions and measurements also partially verifies the assumption of an unchanged evaporation coefficient. We can also notice, the more intense the evaporation is (the higher superheat level the spray is), the larger deviation

is obtained during the experimental measurements. We believe such error results from the larger fluctuation of temperature measurements and the larger deviation to the ideal hypothesis of queso-thermal-equilibrium in theoretical modeling, due to the increased uniformity of local energy and momentum transports as well as the thermal non-equilibrium between two phases. The averaged temperature profile along the chamber centerline of the spray from the specific CFD case is also plotted and compared in the figure. In all cases, the droplets approach the thermal equilibrium about half-way (0.25m) before their exit from the chamber, indicating a sufficient length in the chamber design for the spray flash. However, to focus on the evaporating moment more clearly, the plot range is cut-off at 0.3m.

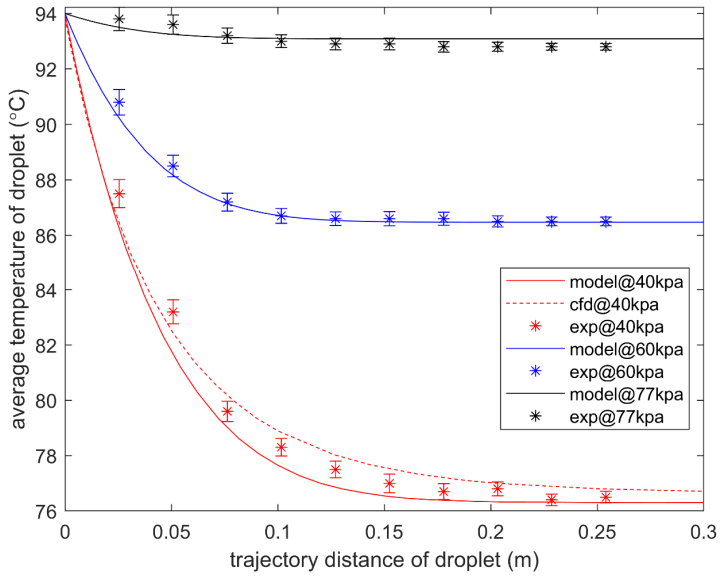

Figure 3.10 Spray temperature profile along the chamber centerline.

3.6 Conclusions

In this study, process characteristics of active vacuum aided spray flash evaporation are investigated by an integrated experimental-modeling-simulation approach. A Lagrangian-Eulerian modeling approach is developed, which is then numerically solved for a case study using ANSYS FLUENT modified with UDF. Two experimental systems are developed in this study: one is to measure the spray flash characteristics such as evaporation rate, temperatures of extracted vapor and liquid residue, and the droplet/vapor cooling along the vertical axis of the chamber; the other one is based on a combined technology of laser marked shadowgraphy (LMS), paralleled laser sweeping (PLS), and particle image velocimetry (PIV) for the determination of droplet size distribution of atomized spray.

The thermal non-equilibrium phenomena in temperature are conspicuously obtained via both experiments and theoretical predictions, which demonstrated the feature of highly efficient evaporation in spray flash under active vacuuming. Such a non-equilibrium between phases has the potential to be utilized in designing a desalination system for achieving better thermal efficiency and yield capacity. Case studies of the operation parametric effects on the spray flash characteristics are demonstrated via both modeling predictions and experimental measurements. The operational pressure in vacuum chamber varies from 25 kPa to 80 kPa, while the operating range in inlet spray temperature varies from 70 to 100°C. The droplet size distribution of water spray can be well fitted into a Rosin-Rammler distribution, with a size range between 0.4 and 1.8 mm and a median size of 1.03 mm. The temperature difference between the extracted vapor and the discharged spray residue can be significantly impacted by the active vacuum extraction and

the superheating of input spray. For example, the temperature difference is linearly increased with the superheating level of input spray, with a slope of 0.47. Both simplified process model and full-scale CFD simulation yield similar spray flash characteristics (with experimental validation), such as spray cooling profile, evaporation rate distribution, and the overall temperature difference between the extracted vapor and liquid residue, which partially verify the very weak vapor-droplet interactions on the droplet flash.

CHAPTER 4

SPATIALLY DEPENDENT SALINITY EFFECT

The previous chapter studied the process characteristics of highly non-equilibrium spray flash evaporation based on pure water. However, in distillation processes, the spray must contain non-volatile fractions (such as salt), and such effects in our highly non-equilibrium flash process can be curial but remain unknown. Therefore, in this section, we developed our spray flash distillation model by introducing the spatially dependent salinity effect into the previous spray flash evaporation model. Meanwhile, such an effect on our processing characteristics has also been parametrically studied.

Our intensive evaporation can lead to a strongly coupled temperature-salinity polarization near the surface region within droplets, which in turn reduces the evaporation rate. In a spray flash desalination chamber with active vacuuming of vapor extraction, the reduced evaporation rate by such a polarization also weakens the thermal non-equilibrium between the extracted hot vapor and the discharged cooler feed residue. In this section, an integrated modeling-experiment methodology is established to study the salinity-influenced droplet evaporation and its effect on crucial process characteristics of spray flash desalination, such as the evaporation rate and efficiency, the coupled internal heat conduction and salt diffusion within droplets, the thermal non-equilibrium between vapor and feed, as well as the non-uniformed vapor flow from vacuum extraction. Specifically: a heat conduction and salt diffusion coupled droplet flash model is proposed; a Lagrangian-Eulerian spray flash desalination model with 1-D Eulerian modeling of vapor flow is proposed for parametric studies; an experimental system of spray flash desalination with

active vacuuming is developed for model validations. The evaporation rate and the thermal non-equilibrium are found to be positively related to the initial superheat levels of the spray but negatively impacted by the initial salinity. Modeling predictions indicate that ignoring the spatial dependence of salinity can over-estimate the flash rate by up to 30% in high salinity cases of salty-water distillation. The thermal non-equilibrium between vapor and feed can be effectively generated under active vacuum, even with a low initial superheat level and high salinity. Increasing feed salinity from 0% to 10% in different cases will narrow the temperature gap between outlet vapor and feed residue by about 10% on average. For typical industrial flash desalination (with salinity up to 10%), with or without considering the spatial dependence of salinity will cause relatively minor differences (less than 5%) on the prediction of evaporation rate.

4.1 Introduction

Flash desalination is an advantaged thermal distillation process based on the physical phenomenon of flash evaporation. It is usually achieved by three different approaches in industry, pool flash, film flash, and spray flash [70]. The spray flash desalination is typically realized by spraying the superheated droplets into a depressurized environment and the droplets intensively evaporate due to the sudden over-saturated status transition [9]. Comparing with pool flash and film flash, the spray flash desalination has a much faster evaporation rate and required less space because of the dramatic increase of the effective evaporation area [11], [16], [20], [71]. Other benefits of spray flash desalination for industrial applications include better evaporation efficiency, better controllability of the flash process, and improving scaling problems [13].

Understanding and quantifying the evaporating mechanism of spray flash desalination has been an academic challenge for decades. Spray flash desalination consists of numerous single-droplet-flash within a bounded environment. In reality, such a droplet flash is a very complicated phenomenon that involves heavily-coupled integrated exchanges of mass, momentum, and energy between multi-components (volatile and non-violate fractions) and phases (liquid and gas). Generally speaking, in a salty droplet flash process under depressurized environment, the evaporation rate of the volatile fraction (water) can be determined by the modified Hertz-Kundsen relation [72], as expressed by :

$$\dot{m}_v = \alpha \pi d_d^{\,2} \sqrt{\frac{M_v}{2\pi R_u T_{d,s}}} \left(P_{sat,v} - P_0 \right) \tag{4.1}$$

The detailed explainition of this equation will be discussed later in the modeling section. Equation (4.1) reveals that the flash rate is positively related to the pressure difference between the corresponding saturated vapor pressure at the droplet surface $P_{sat,v}$ and the ambient pressure P_0. Since the droplet contains dissolved non-volatile substance (salt), $P_{sat,v}$ needs to be corrected based on Raoult's law due to the effect of boiling-point elevation [45], which can be determined as

$$P_{sat,v} = N_w P_{sat} \tag{4.2}$$

where P_{sat} is the saturated pressure of pure water at the temperature on the evaporation surface of droplet, N_w is the mole fraction of water on the evaporation surface of droplet. Hence, a salty (multi-component) droplet flash can be very different from a single-component droplet flash (like pure water) due to the coupled effect of salt concentration.

A salty droplet flashing in a spray flash desalination process is majorly governed by three coupled mechanisms: the heat transfer within the droplet; the heat and mass transfer between the evaporating interface and ambient; and the mass diffusion of the volatile substances inside the droplet due to the concentration gradient created by the evaporation [22]. As a result, the slowest one of above three processes will dominate the overall flash rate. In general, the internal salt diffusion and the mass transfer of the vapor can be hysteretic comparing against the internal heat conduction during a droplet vaporization [22], [29]. However, in a droplet flash with the aid of active vacuuming, the mass transfer of the vapor to the ambient is greatly enhanced, which leaves the internal salt diffusion to be the major limiting factor to the evaporation rate.

Due to the complicated mechanism, modeling of spray flash has been accompanied by certain compromised assumptions, such as constant droplet radius, ignored interactions between droplets and vapor, lumped heat capacity approximation for determining droplet temperature, etc. Therefore, continuous attempts are being made in modeling spray flash desalination process to achieve a more truthful physical meaning by considering more process characteristics, such as size variation of droplets [73], internal heat conduction within the droplet [33], the non-spatial multi-component effect (salt) within the droplet [36], the interaction (convection, radiation, and momentum transports) between droplets and gaseous phase [5], [35], [74], [75], and the polydisperse effect from different droplet sizes contained in a spray [5].

Previous works achieved an in-depth understanding of the spray flash phenomenon. However, one key mechanism during a flash of salty droplets, the internal salt diffusion within the droplets, has been ignored before, and its effect on process characteristics of the

flash remains unknown. Specifically, in previous models, the internal salt diffusion process during the flash is assumed to be infinitely fast that the droplet salinity is a spatial irrelevance value, which is simply determined as a transient volume average. However, this assumption is constantly beyond reality. As mentioned above, the concentration gradient of salt within the droplet is determined by the coupled mass diffusion process and evaporation process. During the flash, the surface evaporation will continuously leave the non-volatile fraction (salt) within the droplet and hence increase its concentration, especially near the surface. Meanwhile, a mass diffusion of salt from the droplet surface to the inner-center will be formed for rebalancing such a local concentration elevation based on Fick's law [29]. In fact, since the internal salt diffusion can be many orders of magnitude slower than the internal heat conduction in a droplet flash, the salt will accumulate around the evaporating interface during the process due to the hysteretic mass diffusion against the evaporation [22]. According to Equation (1) and (2), such a locally increased salinity will further weaken the droplet evaporation rate and efficiency by enhancing the effect of boiling-point elevation to the volatile fraction (water) [15], [47]. As a result, ignoring this salinity polarization phenomenon by adopting a simplified volume average during the calculation will overestimate the evaporation rate. Therefore, in our work, to achieve a more solid physical meaning and a better prediction, the non-uniformed spatially dependent salinity effect coupled with both internal heat conduction and surface flash evaporation is considered in the modeling.

In addition, in a spray flash process with active vapor extraction, a unique thermal non-equilibrium phenomenon exists between the yield vapor and droplet residues [3]. Specifically, in a thermally insulated spray flash process, the droplet temperature will

continuously decrease due to the evaporation latent heat extracted from the droplet phase. Therefore, with the help of active vacuuming for vapor extraction, a temperature gap between the yield hotter vapor and cooler spray residue will be effectively generated during the process. Since the evaporation rate is influenced by salinity, the effectiveness of such a thermal non-equilibrium in a spray flash desalination has not been investigated yet. Hence, in this work we investigated such thermal non-equilibrium characteristics under the impact of different salinities in an actively vacuumed spray flash desalination.

In summary, this paper aims to propose an integrated experiment-modeling methodology to study the spatially dependent salinity effect in an actively vacuumed spray flash desalination process. Specifically, the following sub-tasks are achieved: (1) develop a flash evaporation model of a single salty droplet, which is spatially dependent upon both internal salt diffusion and effective heat conduction; (2) proposed a simplified Lagrangian-Eulerian approach for developing the polydispersed spray flash desalination model based on single droplet models; (3) set up an experimental system of spray flash desalination with active vacuuming for model validations; (4) perform parametric studies via the process model to investigate the spatially dependent salinity effect on crucial process characteristics of spray flash desalination, such as the evaporation rate and efficiency, the coupled internal gradient of temperature and salt concentration, the overall thermal non-equilibrium between extracted vapor and discharged feed residue;

4.2 Spray Flash Desalination Model

For the two-phase flow modeling of spray flash desalination, it is convenient to adopt a hybrid Lagrangian-Eulerian approach, in which the droplet transport is described by Lagrangian trajectory modeling, and the vapor flow is described in an Eulerian framework.

The Lagrangian model yields the spatial dispersion of sprayed droplets and results in the spatial distribution of vapor generation rate, which are implemented into the Eulerian equations of vapor flow. For simplicity, in Lagrangian modeling (single droplet modeling), the droplet formation at the very beginning near the nozzle tip, and interactions of droplet-droplet and droplet-wall are ignored. Based on such simplicities, the spray flash desalination process within an actively vacuumed chamber is schematically described in Figure 4.1.

In this section, the modeling of spray flash desalination includes two parts: (1) the spatially dependent flash model of a single salty droplet (SDM) governed by partial differential equations; (2) an overall polydispersed spray model based on the droplets model and a simplified 1-D Eulerian modeling of vapor flow.

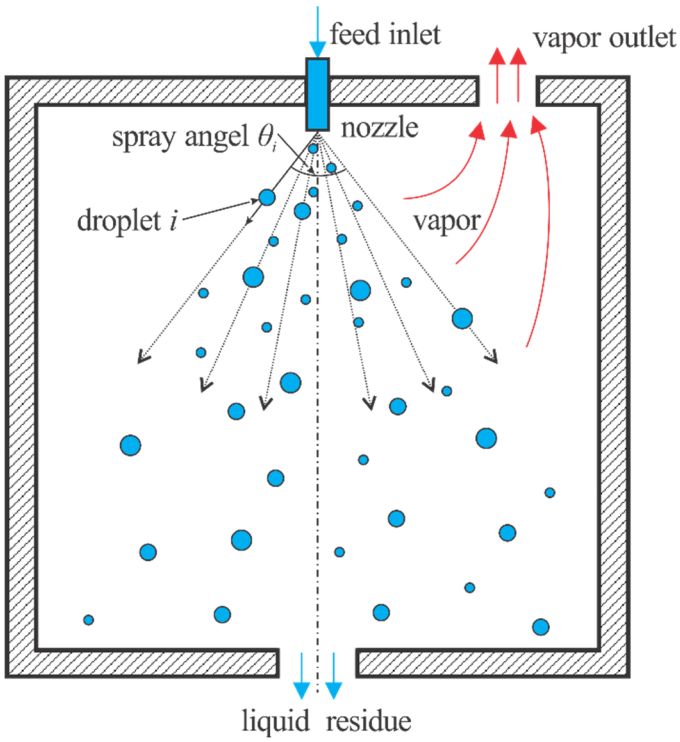

Figure 4.1 Schematic droplet-vapor transport in a vacuum spray flash.

4.2.1 Spatially Dependent Salty Droplet Flash Model (SDM)

While the disintegrated elements in an atomized liquid spray can be highly non-spherical at the initial nozzle injection [59], the surface tension will quickly contract the elements into droplets [60]. For simplicity, we ignore this initial stage of non-sphericity and assume all droplets are spherical without breakup or coalescence during their transport. The schematic spatial distributions of temperature (T) and salt molar concentration (c) in a droplet with flash evaporation are shown in Fig. 4.2, where r, u_d, and m_v represent droplet radius, velocity, and evaporation rate, respectively. In theory, such temperature and salinity distributions will form a spherically symmetric gradient within the droplet due to the internal heat conduction and salt diffusion during the evaporation [22].

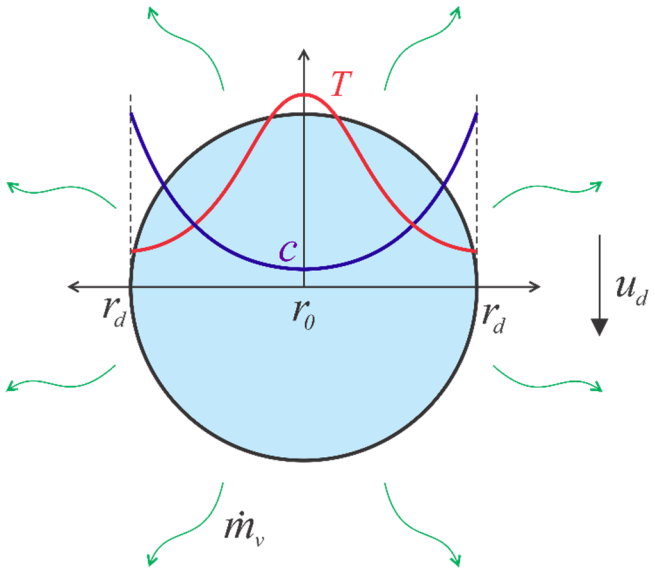

Figure 4.2 Spatial concentration-temperature distributions in a flashing droplet.

In a flash spray where the droplets evaporate without external heating, the latent heat is self-supplied by the droplet. Therefore, the flash intensity will be majorly dominated by the internal heat conduction rate within the droplet to the surface. Assuming the thermal

property of the droplet is spherically-symmetric, the internal heat conduction can be expressed in the spherical coordinate:

$$\frac{\partial}{\partial t}\left(\rho_l c_l T_d\right)=\frac{1}{r^2}\frac{\partial}{\partial r}\left(r^2 k_{eff}\frac{\partial T_d}{\partial r}\right) \tag{4.3}$$

where r is the radius of the droplet, T_d is the time-spatial dependent temperature, ρ_l and c_l are the density and specific heat of liquid, and k_{eff} is the effective thermal conductivity in flash evaporation [64]:

$$k_{eff}=1.86k+0.86k\tanh\left[2.245\log_{10}\left(Pe/30\right)\right] \tag{4.3a}$$

where k is the molecular conductivity, and Pe is Peclet number of the droplet. The initial condition is given by spray temperature at nozzle injection:

$$T_d(0,r)=T_{d0} \tag{4.3b}$$

According to the symmetric condition of heat transfers at the droplet center and the droplet surface, the boundary conditions can be respectively expressed as:

$$k_{eff}\frac{dT_d}{dr}\Big|_{r=0}=0 \tag{4.3c}$$

$$\pi d_d^2 k_{eff}\frac{dT_d}{dr}\bigg|_{r=d_d/2}=-h_{fg}\dot{m}_v+h_m\frac{\pi}{4}d_d^2(T_v-T_d) \tag{4.3d}$$

where h_m is the convective heat transfer coefficient, which may be approximated using Ranz and Marshall correlation with vapor-film properties and relative droplet velocity [63]. In which the Nusselt number is determined by:

$$\overline{Nu}_d=2+0.6\,\mathrm{Re}_{d,m}^{1/2}\,\mathrm{Pr}^{1/3} \tag{4.3e}$$

As mentioned in the introduction, the evaporation rate can be determined with Equation (4.1) and Equation (4.2):

$$\dot{m}_v=\alpha\pi d_d{}^2\sqrt{\frac{M_v}{2\pi R_u T_{d,s}}}\left(P_{sat,v}-P_0\right) \tag{4.1}$$

$$P_{sat,v}=N_w P_{sat} \tag{4.2}$$

where α is the evaporation coefficient of the evaporation (which is a case sensitive empirical constant that needs to be calibrated from the experiment), M_v is the molecular

weight of vapor, R_u is the universal gas constant, $P_{sat,v}$ is the corresponding saturated vapor pressure at the droplet surface, and P_0 is ambient pressure. The mole fraction of water, N_w , can be further expressed as:

$$N_w = \frac{1}{1+\frac{MW_w}{MW_s}(\frac{C_s}{1-C_s})} \tag{4.2a}$$

Where MW_w is the molar weight of water, and MW_s is the molar weight of salt. C_s is the local mass fraction of salt on the evaporating droplet surface, which can be given by governing relations of Equation (4.4).

With the further approximations that the gas phase is ideal gas and consists only of evaporated and saturated vapor, the saturated pressure can be related to the droplet surface temperature by Clausius-Clapeyron equation [63]:

$$\ln \frac{P_{sat}}{P_0} = -\frac{h_{fg}}{R}(\frac{1}{T_d}-\frac{1}{T_0}) \tag{4.2b}$$

In previous works, the salinity of the droplet is usually adapted by a homogenous average for the calculation. But in reality, along with the on-going evaporation, the salt will accumulate on the droplet surface and result in a higher local concentration, which negatively affects the flash rate. Meanwhile, an internal salt diffusion process is also happening within the droplet due to the local concentration difference between the droplet center and its surface. Assuming the salt concentration within the droplet is spherically-symmetric, according to the Fick's second law, the local molar concentration change rate of salt in spherical coordinates can be expressed by:

$$\frac{\partial c}{\partial t} = D\frac{1}{r^2}\frac{\partial}{\partial r}(r^2\frac{\partial^2 c}{\partial r^2}) \tag{4.4}$$

Where D is the diffusion coefficient and c is the molar concentration of the non-volatile fraction. For example, with a dilute solution of 1:1 electrolytes (NaCl), the diffusion rate can be theoretically determined as [29]:

$$D_{NaCl} = \left[\frac{2}{1/D_{Na+} + 1/D_{Cl-}} \right] \tag{4.4a}$$

The initial condition is given by the initial salinity of the spray at nozzle injection:

$$c(0, r) = c_0 \tag{4.4b}$$

Where c_0 is the initial mole concentration of salt. According to the symmetric condition of salt diffusions within droplets, the boundary conditions can be respectively expressed as:

$$\frac{dc}{dr}\Big|_{r=0} = 0 \tag{4.4c}$$

$$4\pi r^2 D \frac{dc}{dr}\Big|_{r=d/2} = \frac{\dot{m}_v C_s}{MW_s} \tag{4.4d}$$

In addition, the conversion between the molar concentration of salt and its mass fraction follows by:

$$c = \frac{\rho_d C_s}{MW_s} \tag{4.5}$$

It is worth mentioning, if the initial droplet salinity is large enough, the salt crystallization may happen on the droplet surface due to the local salt accumulation from the evaporation [76]. In theory, the salt crystallization during a droplet flash is very complicated and would negatively affect the evaporation rate by reducing the effective

evaporative area [77], [78]. However, since the major operating salinity of the brine in industrial desalination is 3% ~ 7% [70], [79], the salt crystallization is unlikely to happen during the process due to such a low initial salinity and limited evaporation amount from a self-heat supplied flash evaporation (this has also been proved in the result section). Therefore, this work ignores impacts from salt crystallization and assumes the local salinity will not change anymore once it achieves saturation (its equilibrium solubility). In that case, the local salt concentration will be determined by the specific equilibrium solubility, which is insensitive to the pressure [80] and can be polynomial fitted according to the experimental data in terms of the local temperature [81], [82].

In the Lagrangian model, the dynamic motion of an individual droplet is governed by the overall momentum transfer to the droplet. Conceptually, these momentum transfer terms include the drag force, gravity, buoyancy, and forces due to acceleration, such as added mass force and Basset force [61]. However, due to the large density ratio of the droplet to vapor (about 10^3), the buoyancy, added mass force, and Basset force are negligibly small compared to the drag force. Hence, the momentum equation of a single droplet is expressed by:

$$\frac{d\left(m_{di}\mathbf{u}_{di}\right)}{dt} = m_{di}\mathbf{g} + C_{di}A_{di}\frac{\rho_v}{2}\left|\mathbf{u}_v - \mathbf{u}_{di}\right|\left(\mathbf{u}_v - \mathbf{u}_{di}\right) \tag{4.6}$$

where the subscript "*i*" denotes the i^{th} droplet in a spray, m_d is the mass of droplet; $\boldsymbol{u}_d$ and $\boldsymbol{u}_v$ denote the droplet and vapor velocities, respectively; $\boldsymbol{g}$ is the gravitational acceleration; C_D is the drag coefficient; A_d is the cross-sectional area normal to the droplet trajectory; and ρ_v is the vapor density.

At high droplet Reynolds number (*e.g.*, 30 < Re_{dm} < 200), with the correction of evaporation [22] and the Hadamard-Rybcyznski correction of a fluid particle [62], the drag coefficient C_d can be estimated by:

$$C_d = \frac{24.432}{\mathrm{Re}_{d,m}^{0.721}}\left(1+\frac{c_{p,m}(T_v - T_d)}{h_{fg}}\right)^{-0.27}\left(\frac{3\mu_d + 2\mu_{v,m}}{3\mu_d + 3\mu_{v,m}}\right) \tag{4.6a}$$

where h_{fg} is the latent heat; $Re_{d,m}$ is the droplet Reynolds number, modified with the vapor film viscosity $\mu_{v,m}$, and is defined by:

$$\mathrm{Re}_{d,m} = \frac{\rho_v d_d}{\mu_{v,m}}\left|\mathbf{u}_d - \mathbf{u}_v\right| \tag{4.6b}$$

The droplet includes two components in this model, the volatile and the non-volatile fractions (water and NaCl in our case). In previous works, the volume occupation of salt is often ignored for simplicity. However, the density ratio of salt over water is about 2.16, which is comparable. Therefore, the volume of salt should not be ignored, especially for cases with high salinity. Assuming the solution is ideal, hence the averaged density of the droplet is defined as:

$$\bar{\rho}_d = \frac{\rho_s \rho_w}{C_s \rho_w + (1 - C_s)\rho_s} \tag{4.7}$$

where $\bar{\rho}_d$ is the average density of the droplet, ρ_s is the density of salt, ρ_{w} is the density of water, C is the salinity (mass fraction of salt). Further, the droplet mass m_d is expressed by:

$$m_d = m_s + m_w = \bar{\rho}_d \frac{\pi}{6} d_d^{\,3} \tag{4.8}$$

Assume there is no entrainment of salt during the flash, the mass balance of the droplet calls for:

$$\frac{dm_d}{dt} = -\dot{m}_v \tag{4.9}$$

Finally, the spatially dependent droplet flash model (SDM) is established with nine governing equations (Equation (4.1) – Equation (4.9)) for nine unknowns (m_v, $P_{sat,v}$, T_d, c, C_s, u_d, ρ_m, d_d, and m_d). Thus the problem is closed, and equations become solvable with proper initial conditions.

4.2.2 Lagrangian-Eulerian Polydispersed Spray Flash Model

The overall spray flash model within an evaporator can be developed by extending the single droplet flash characteristics into an overall spray flash process, with coupled energy and momentum interactions between droplets and vapor. Such a model can be realized by a Lagrangian-Eulerian approach, in which the Lagrangian trajectory model of all individual droplets from the spray are coupled with the Eulerian modeling of vapor flow. However, a fully described 3-D Eulerian modeling of vapor flow (considered the spatial non-uniformity) is complicated for solving, which requires a specific construction of control volumes [83]. Hence it is not practical to utilize in parameter studies due to a high computational cost. In order to simplify the modeling mathematics and avoid constructing control volumes for calculation, in this section we proposed a simplified 1-D Eulerian modeling for the vapor flow to realize an overall spray flash desalination model.

Figure 4.3 shows schematically the 1-D Eulerian modeling of vapor flow. The generated vapor is assumed to be uniformly flowing upward (along the x-direction only) within the evaporator during the process and the volumetric effect of droplets is ignored in the vapor flow. Considering the flash desalination process usually happens under

depressurized environments with relatively low vapor densities, this simplification is likely acceptable and will be evaluated later against the results from the fully expressed 3-D approach (CFD). Further, for the Lagrangian modeling of droplets, we assume the spray formation at the very beginning and interactions among droplets (such as coalescence and breakup) can be ignored [22], in which the droplets size distribution and initial injection velocity are pre-determined from the spray characteristics via experiments.

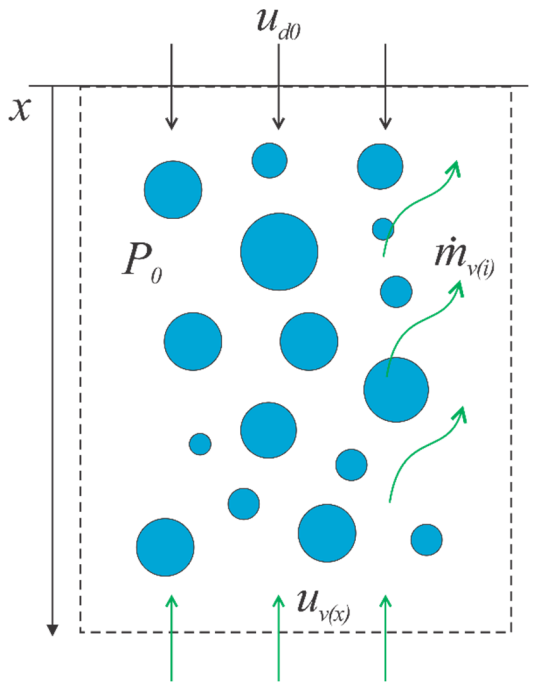

Figure 4.3 One-D Eulerian modeling schematic of polydispersed spray flash.

In the case of steady-state 1-D vapor flows, the time-based Lagrangian frame for the droplets flash dynamics can be converted into the Eulerain frame in terms of the vertical direction (x) only：

$$\frac{d}{dt} = \mathbf{u}_d \frac{d}{dx} \tag{4.19}$$

where x is a space coordinate along the gravity.

Further, since both the hydrodynamic transport and the evaporation rate can behave quite differently for individual droplets due to their different sizes during the spray flash evaporation [83], the spray model needs to consider the polydispersed effect by sub-grouping all the droplets into *N* categories based on different sizes. For each sub-group *(i)*, given the mass flow rate, droplet size and injection velocity, the initial droplets number density can be determined as:

$$n_{d0}(i) = \frac{\dot{m}_t(i)}{m_{d0}(i)\mathbf{u}_{d0}(i)} \tag{4.20}$$

where m_t is the total mass rate of the sub-group, m_{d0} and $\mathbf{u}_{d0}$ is the initial droplet mass and velocity. Based on the assumption of no droplet breakup or coalescence, the mass conservation leads to a droplet number density conservation along the vertical direction, expressed by

$$\frac{d}{dx}\left(n_d(i)\mathbf{u}_d(i)\right) = 0 \tag{4.21}$$

In the spray model, the impact of up-flowing fresh vapor within the chamber should be considered in the droplet transport equations. Based on the highly dilute condition, the volumetric effect of droplets can be ignored, by assuming pointed sources of droplet-vapor interaction in the governing equations of vapor. The mass conservation of vapor can be conveniently expressed in an Eulerian form:

$$\frac{d\left(\rho_v u_v\right)}{dx} = \sum_{i=1}^{N}\left(n_d(i)\dot{m}_v(i)\right) \tag{4.22}$$

While the energy equation takes the form:

$$\frac{d(\rho_v c_{pv} u_v T_v)}{dx} = \sum_{i=1}^{N} \left(n_d(i) \left[\dot{m}_v(i) c_{pv} T_d(i) + h(i) \frac{\pi}{4} d_d^2(i) (T_d(i) - T_v) \right] \right) \tag{4.23}$$

This 1-D Eulerian vapor flow model (equations (4.19) – (4.23)) can be combined with the Lagrangian droplet models (SDM) to become a spray flash desalination model, in which u_v, m_v, T_v, and T_d are the shared parameters from both two model and needs to be determined in couple. Now we have (9N+3) equations (equations (4.1) - (4.9) for droplets of each subgroup, and equations (4.21) - (4.23) for vapor) to establish a process model of the overall spray flash desalination, corresponded to (9N+3) coupled variables ($m_v(i)$, $P_{sat,v}(i)$, $T_d(i)$, $c(i)$, $C_s(i)$, $u_d(i)$, $\rho_m(i)$, $d_d(i)$, $m_d(i)$and $n_d(i)$, u_v and T_v). Thus, the model is closed; these equations are solvable with proper initial and boundary conditions.

4.3 Experimental Study

A lab-scale spray flash desalination system is built in this study to achieve a steady flash desalination process with constant salinity for validating the salinity effect and the thermal non-equilibrium between droplets and vapor. The major measured parameters during the experiments include the total evaporation rate, the feed-in temperature, pressure, and flow rate of the spray, temperatures of the discharged feed and extracted vapor, the temperature profile of spray flash along with the chamber height, the operating pressure of vacuum chamber, the replenish flow rate of water, and the electric conductivities for both cyclic feed and yield water.

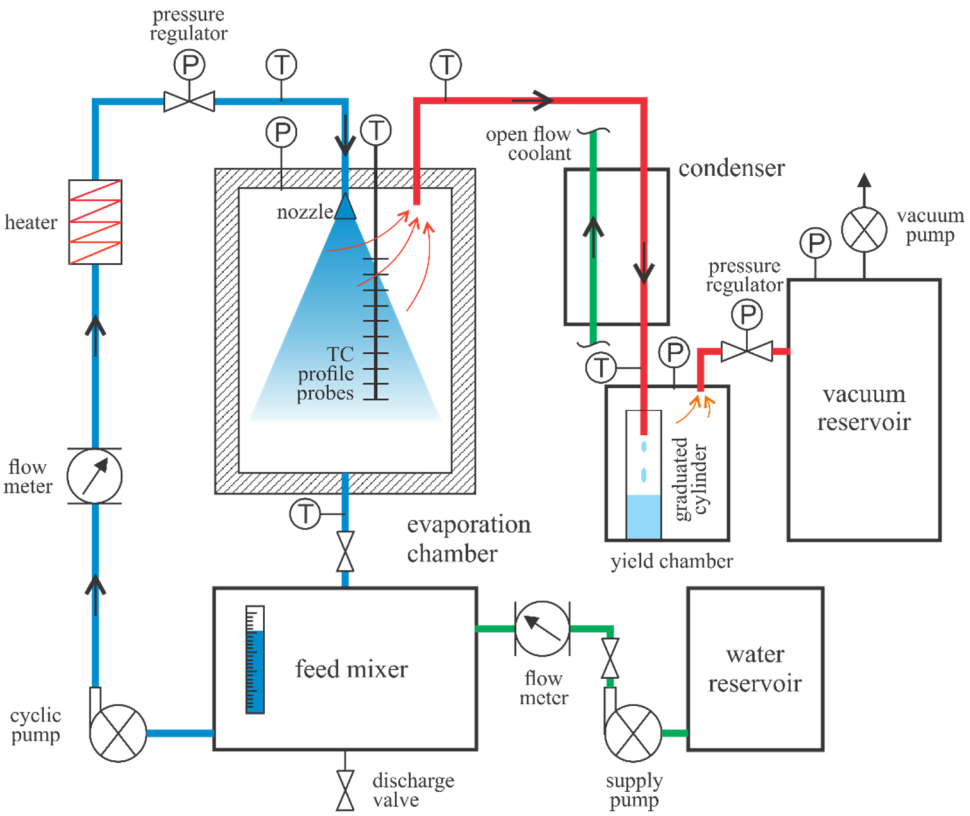

Figure 4.4 Schematic diagram of spray flash desalination system.

Figure 4.4 shows a schematic diagram of our spray flash desalination system. The main components of the system consist of a vacuum-maintained and thermal insulated evaporation chamber, a feed mixer of replenished supply (water) and cyclic solution residue, a vapor condenser, a yield chamber, a water reservoir of replenished supply, a vacuum reservoir, a feed circulation pump (Warren Rupp double diaphragm pumps, manufacture number (Mfr.): WR10PP6XPP9), a water pump for replenished supply (Gol pump, Mfr.:WWB-09127), a heater of feed heating (Vulcan immersion heater, Mfr.: AUW250B), and a spray nozzle (Bete Fog Nozzle, Mfr.:1/4WL1-1/2-60) for generating atomized spray.

As shown in the figure, the system has two main flow paths: the feed-spray path (marked as blue) and the vapor-condensate path (marked as red). An initial volume of feed

solution (salty water) stored in the feed mixer is pressurized via the cyclic pump, heated up via the feed heater, and then injected into the vacuumed evaporation chamber via a flowrate-temperature regulated nozzle. An atomized spray is formed through the nozzle, followed by a spray flash process inside the chamber due to the depressurized environment. The evaporation chamber is thermally insulated, with two ports for vapor extraction and spray residue discharge, respectively. The discharged liquid residue from the chamber will be mixed with replenished water in the feed mixer for maintaining a constant salinity during the process. In order to do so, the replenished water is added to the feed mixer by the supply pump with a regulated flow rate that equals the instantaneous evaporation rate from the spray flash. Then, the mixed feed will be continuously recirculated by the cyclic pump for maintaining the spray flash process. The generated vapor from the spray flash will be extracted from the top port of the evaporator into the vapor condenser. In the condenser, the vapor is fully condensed by an open flow coolant channel. The condensate is further collected into a graduated cylinder within the yield chamber. The inlet flow temperature and pressure of the yield chamber will be monitored to make sure the vapor is fully condensed within the condenser. Under a steady-state operation, the increased rate of water level within the graduated cylinder will be monitored to determine the evaporation rate of the process. An insignificant amount of non-condensable gases (NCG), degassed or co-vaporized from spray flash, will be further discharged out of the system into the ambient by a vacuum pump. The vacuuming extraction is also pressure regulated and baffled by a vacuum reservoir to avoid pressure fluctuations.

During experiments, the temperature change of the spray along the vertical direction is measured by a temperature profile probe (Omega ten sensing type k

thermocouple profile probes). Since the evaporation chamber is thermal insulated, the latent heat needed for the evaporation is self-supplied by droplets. Therefore, such a temperature change along its traveling trajectory can reflect the evaporation rate [9], [18]. The chamber operating pressures are measured by vacuum pressure gages (IFM pressure sensor, model number: PG2794). The volume flow rates of inlet spray and feed replenishment are regulated by flow meters (IFM efector magnetic inductive flow meter, model number: sm6004). The feed heating is maintained based on the outlet temperature of the feed from the heater. The salty water used as the feed solution is made by mixing NaCl with regular tap water, and the feed replenishment was using regular tap water. Before and after each experiment, the conductivities of both feed solution and yield water are measured by the conductivity meter (Extech EC400 ExStik2) to ensure the salinity remained unchanged for the solution and no salt was entrained into the yield water by the vapor flow during the experiment.

4.4 Results and Discussion

A case study with both theoretical calculations and experiments is used to investigate some unique processing characteristics under salinity effects in an actively vacuumed spray flash, including the evaporation rate and efficiency, the internal polarization of temperature and salinity within the droplet, the salinity sensitivity, the thermal non-equilibrium of the process.

The basic operational and geometric information regarding the flash process within the evaporation chamber is summarized in Table 4.1 The heat dissipation via the chamber to the ambient is insignificant (less than 1%), judged by the experimental estimation of

enthalpy imbalance between the inlet feed and outlets of vapor and liquid. The spray characteristics (droplet size distribution and velocity) of experiments are measured to calibrate the initial conditions for model validation [83]. Since in most industrial desalination processes, the brine salinity ranges from 3% to 7% in different stages of a multi-stages distillation plant [70], [79], [84]. Therefore, in this work the initial salinity of the spray is mainly studied from 0% to 10%. In addition, an upper limited case (before surface crystallization happens) of 23% initial salinity is also briefly discussed.

Table 4.1 Key Geometric and Operational Parameters

Parametric	Value	Unit
Spray nozzle	Full-cone	-
Spray angle	57	°
Droplets size distribution	Rosin-Rammler distribution: κ=4.413 and δ=1.097	-
Nozzle location	Top center	-
Spray injection velocity	3.3	m/s
Spray liquid	Salty water	-
Initial salinity	0% ~ 10%	-
Spray flow rate	45.0	ml/s
Chamber height	0.5	m
Chamber diameter	0.3	m
Vapor outlet diameter	0.75 (19.05)	Inch (mm)
Liquid outlet diameter	0.5 (12.7)	Inch (mm)
Spray initial temperature	70 - 100	°C
Chamber vacuum pressure	0.25 - 0.8	atm
Chamber material	Stainless steel with insulation	N/A
Thermal resistance of chamber	2.16	$K \cdot m^2/W$

4.4.1 Salinity Effect on Evaporation Rate

In this section, the salinity effect on the evaporation rate in a spray flash desalination process has been discussed via the process model (SDM with 1-D vapor flow) accompanied by experimental validations. In a thermally insulated spray flash desalination that the latent

heat is self-supplied by the spray, the evaporation process can be reflected as the temperature decrease of droplets. Such a temperature change has been a curial experimental characteristic for measuring the flash process [2], [5], [9], [19], [20]. Hence in this work, the spray temperature along the central vertical direction of the evaporator is measured to reflect the processing rate of a spray flash. The process model is validated with experiments under the same operating conditions but various operating pressures (0.4 atm and 0.6 atm) and different salinity (3.5% and 10%), as shown in Figure 4.5.

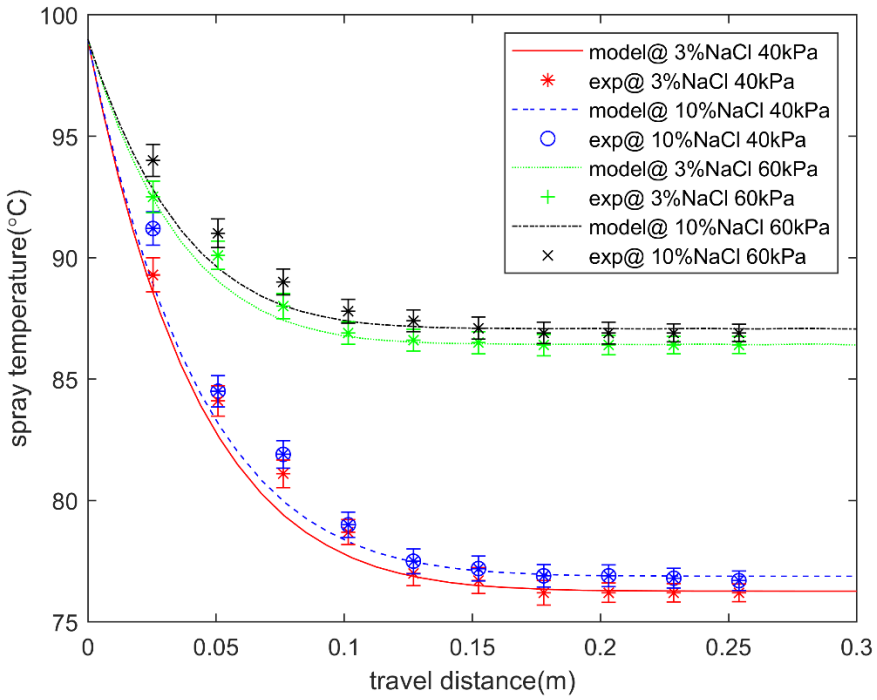

Figure 4.5 Spray temperature vs. travel distance during the flash.

For the model validation, the empirical evaporation coefficient α in Equation (4.1) is adopted to be 0.1 based on the experimental pre-calibration. In addition, the droplets from the polydispersed spray are re-grouped into seven categories of different sizes, shown in Table 4.1. The modeling result plotted in Fig. 4.5 is the averaged temperature from all

groups along the axial direction of the chamber to represent the overall flash progress of the spray. The experimental result of each operation is averaged from five independent measurements to ensure its stability and repeatability, in which error bars (represented by the standard derivation) are also plotted in the figure. Also, from the temperature decreasing curve we can see the process happens very fast that it only takes about half-depth of the chamber (0.25m) to achieve the saturated status, therefore the travel distance is cut off at 0.3m for a better illustration. It can be seen that the process model produced a good agreement with experiments under various operating conditions. The evaporation rate of flash desalination is negatively impacted by either the salinity or the operating pressure. Moreover, either increasing the operating pressure or the salinity will elevate the corresponding saturated temperature of the droplet in a flash process.

4.4.2 The Non-uniformity of Internal Salinity

In previous works, the internal salinity of the droplet is assumed to be uniformly distributed all the time during a spray flash process. But in reality, the intensive flash evaporation will accumulate non-volatile factions (salt) near the droplet interface and further generate an internal concentration gradient within the droplet. Such a surface salt concentration will worsen the flash rate and efficiency. Meanwhile, the droplet flash will also result in an internal thermal non-uniformity (or temperature gradient). Obviously, the non-uniformity of both internal temperature and salinity will increase along with the increased process intensity. As a result, both internal distributions of temperature and salinity are coupled together to conjointly affect the flash evaporation rate. In this section, a parametric study is performed based on the process model to investigate the flash performance of a droplet under the effect of non-uniformed internal salinity.

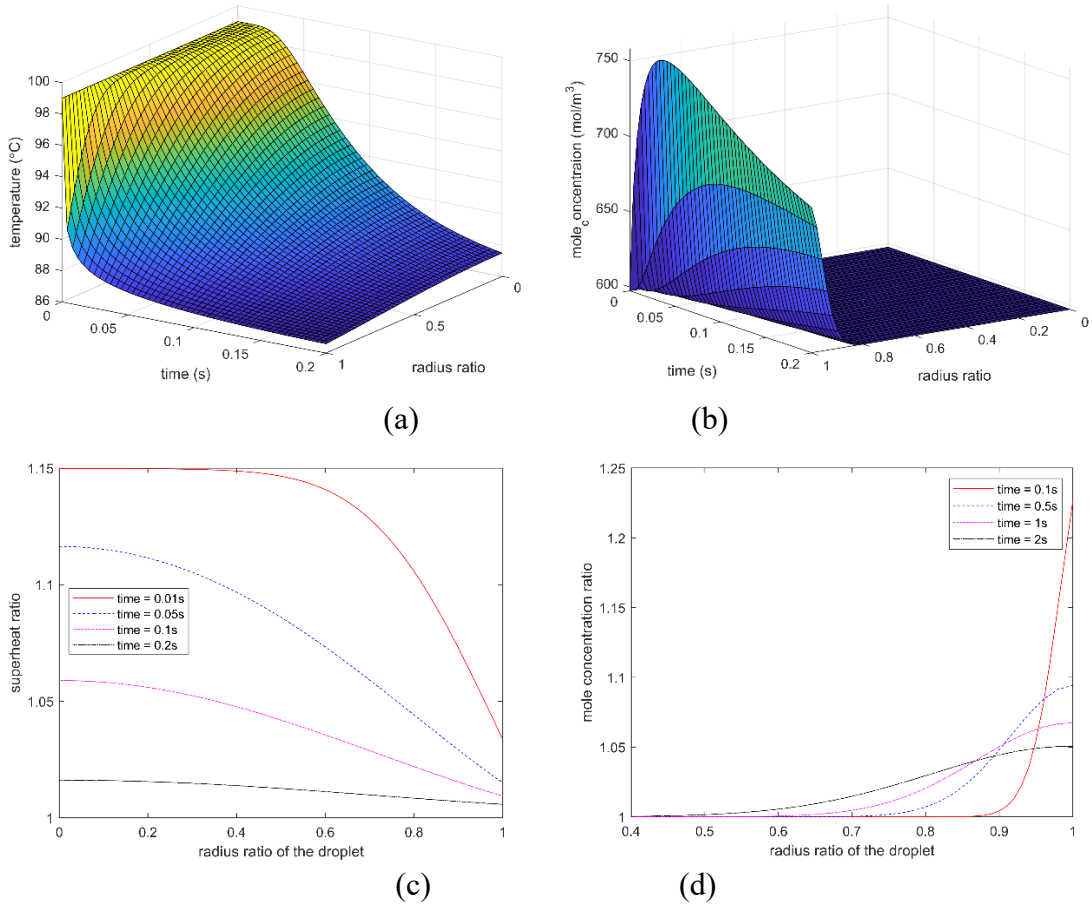

Figure 4.6 Thermal-salinity coupled internal polarization (a) internal temperature contour of the droplet; (b) internal molar concentration contour of NaCl within the droplet; (c) internal temperature distribution at different processing time; (d) internal molar concentration of NaCl at different processing time.

Figures 4.6(a)-(d) show modeling results of an example case (1mm droplet, 99°C initial spray temperature, 3.5% salinity, and 60kPa operating pressure). Figures 4.6(a) and (b) present the internal contours of temperature and salt molar concentration over time within the droplet during the process, respectively. Figures 4.6(c) and (d) illustrate the radial internal distributions of the superheat ratio and the NaCl molar concentration ratio at different processing times, respectively. In these figures, the radius ratio is a dimensionless number defined as:

$$x = \frac{r_x}{r_d} \tag{4.24}$$

Which r_x is the distance between the droplet center and the objective location in a spherical coordinate, and r_d is the droplet's radius. The radius ratio 0 represents the droplet center and the radius ratio 1 means the droplet surface. The dimensionless numbers of the superheat ratio and the mole concentration ratio appeared in figures 8(c) and (d) are defined as below, respectively:

$$\theta^* = \frac{T_{d,x}}{T_{sat}} \tag{4.25}$$

$$c^* = \frac{c_{d,x}}{c_0} \tag{4.26}$$

Where $T_{d,x}$ is the internal temperature at location x, T_{sat} is the saturated temperature corresponding to the operating pressure, $c_{d,x}$ is the molar concentration at location x, and c_0 is the initial uniformed molar concentration of the droplet.

In figures 4.6(a), (b), and (c), the resulting plots stop at 0.2s when the flash process is almost completed, indicated by the radial temperature distribution that has already uniformly closed to the saturated value. However, since the NaCl diffusion is much slower than the heat conduction, the processing time is extended to 2s in Figure 8(d) to fully illustrate such a process tendency. Also the plotting position is focused near the surface area (the radius ratio starts from 0.4).

These results indicate the flash evaporation of a droplet will cause an obvious non-uniformity of internal thermal and salinity distributions. Such thermal non-uniformity will decrease along with the process going on. However, for the salinity non-uniformity, as expected, it will increase firstly at the beginning due to the salt concentration effect near

the droplet surface from the evaporation. Yet with the process going on and the evaporation becoming less intense, the inward salt diffusion rate will exceed the surface salt accumulation rate and decrease the overall salinity non-uniformity within the droplet.

On the other hand, although the salinity distribution will eventually become uniform, such a process will take much longer (about 25 times slower in this case) than the re-uniform process of the temperature, due to the orders of magnitude difference between heat conduction rate and diffusion rate. As a result, for the spray flash desalination in most cases, an obvious salinity non-uniformity within the droplet will constantly exist during the flash.

Another case is also calculated to judge when salt crystallization will happen under this same operating condition. It turns out, with the initial salinity of 23%, the peak local salt concentration on the droplet surface will achieve the corresponding equilibrium solubility of 27.7%. However, this initial value is beyond the scope of this study and typical spray flash desalination.

4.4.3 Effects of Internal Salt Diffusion

The droplet flash rate and efficiency are affected by its internal salt diffusion process. But such an effect is a not yet quantified and remains unknown. To answer this question, parameter studies regarding the flash rate and efficiency under various salt diffusivities have been performed via the process model. In theory, the salt concentration rate on the droplet surface during the flash process is positively related to the droplet evaporation rate and initial salinity, yet negatively associated with the inward salt diffusion rate. Therefore, we looked into a case with a high initial superheat ratio and salinity of the droplet to discover the impacts of salt concentration in a more apparent way.

In Figure 4.7, internal salt diffusion effects on the evaporation rate (in terms of the superheat ratio T^*) and efficiency are studied with five different diffusivities under the case of a 1mm droplet with 100°C initial temperature and 10% initial salinity evaporating under 20kPa operating pressure. The diffusion coefficient of NaCl in an aqueous solution can depend on many factors such as salinity, pressure, and temperature [29]. For a dilute NaCl aqueous solution (such as seawater) in typical desalination processes, its diffusion coefficient is around 1.6×10^{-9} m^2/s [85]. In the figure, the infinite diffusivity represents the simplest ideal case with the assumption that no salt accumulated on the droplet surface. The salt concentration is evenly distributed within the droplet all the time. The diffusivity of 1.6×10^{-9} m^2/s represents a typical realistic case. The three other coefficients, 1.6×10^{-8} m^2/s, 5.3×10^{-10} m^2/s, and 1.6×10^{-10} m^2/s, correspond to 10 times, 0.3 times, and 0.1 times of a typical value, which may never be realistic, are only included for parametric study.

The evaporation efficiency in this study is defined by the ratio of the real consumed heat over the maximum potential heat for evaporation after a certain processing time, which is mathematically expressed by:

$$\eta = \frac{\theta_0^* - \theta_t^*}{\theta_0^* - \theta_{t,D=\infty}^*} \tag{4.27}$$

Where θ_0^* is the initial superheat ratio of the droplet, subscript t corresponding to a specific processing time t, and subscript $D=\infty$ indicates the ideal case with infinite diffusivity, which represents the minimum terminal superheat ratio (or the maximum evaporation efficiency) can be potentially achieved without any salt concentration effect on the droplet surface.

In Figure 4.7, two horizontal black dash-lines mark the superheat ratios of 1.665 and 1.015, respectively, which indicate the complete theoretical range of the evaporation efficiency from 0 to 1 for this process. The figure shows a smaller diffusivity will lead to a lower evaporation rate and efficiency, and elevate the terminal temperature (saturated temperature) of the process. Because slowing the salt diffusion will enhance the internal salt polarization within the droplet and increase the local salt concentration on the droplet surface. However, compared with the ideal infinite diffusivity, the evaporation rate and efficiency in the realistic case have not reduced much (about 1.5% lower) in this case. Also, the magnitude of such a decrease is negatively related to the diffusivities. The impact from salt polarization becomes more noticeable in cases with smaller diffusivities. For example, the evaporation efficiency drops from 98.7% to 91.9% when the diffusivity becomes ten times smaller (1.6×10^{-10} m^2/s) than the realistic value. Of course, the evaporation efficiency will eventually achieve 100% in all cases as long as the processing time is long enough, but that may not be the case in industrial applications.

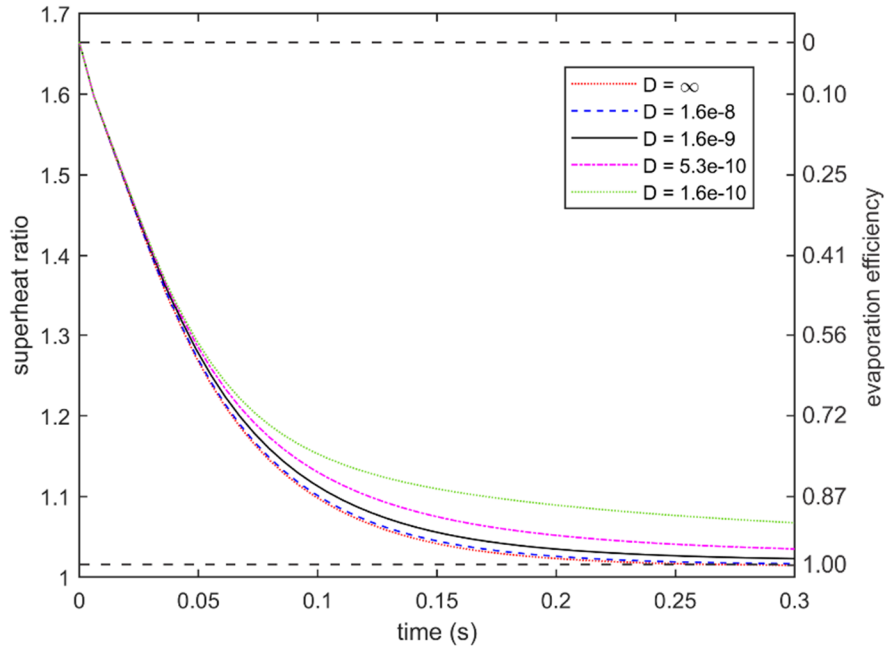

Figure 4.7 Evaporation rate and efficiency of droplet flash under various diffusivity.

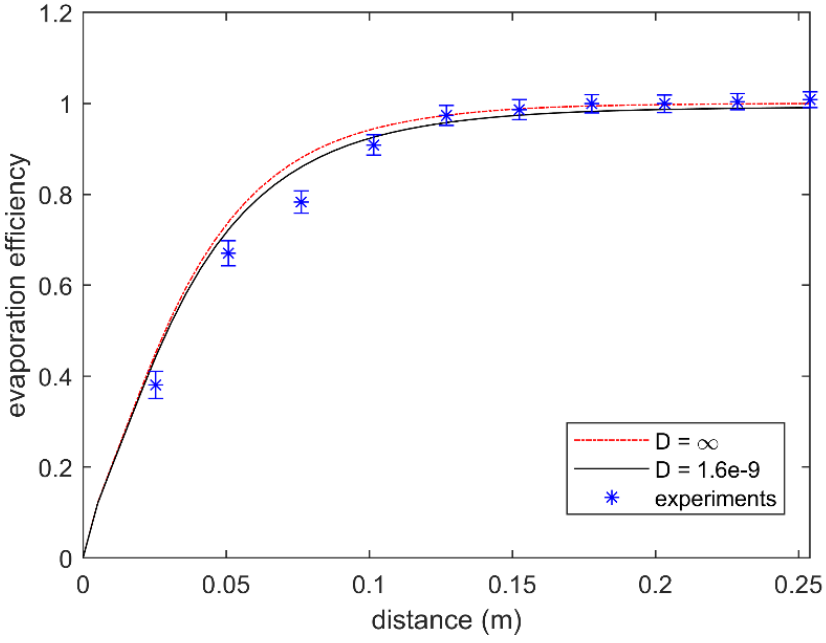

Figure 4.8 Evaporation efficiency of cases with/without internal salt polarization.

As shown in Figure 4.7, the negative impact from internal salt polarization on the droplet evaporation rate and efficiency is not significant, yet it can be further smaller in more typical flash desalination cases with lower initial superheat ratio and salinity. Figure 4.8 shows the spray flash desalination with two NaCl diffusivities (infinite large vs. realistic value) in a more typical operating condition (same as in Figure 4.7 but a higher operating pressure of 40 KPa). It presents an averaged local status from the polydispersed spray validated with the experiment. The experimental result is calculated and averaged from five measurements in term of the spray temperature, in which the error bar represents the standard deviation. According to the result, we can see the theoretical difference regarding evaporation efficiency between the two diffusivities is very small (about 1%), which cannot be justified since measuring errors are more significant. Although the case of realistic diffusivity indeed is closer to the experiments in terms of the evaporation rate (indicated by the curve gradient), such a difference may not be worth the consideration to include salt polarization due to the increased mathematical complexity during modeling.

The reason for the little impact of internal salt polarization during the flash process in these cases is the total amount of evaporation is relatively small due to limited thermal storage for phase change in each droplet. Hence the salt concentration on the droplet surface during the process is not dramatic. Therefore, for most spray flash desalination processes in the industry (salinity ranges from 3.5%~7%), the salt polarization can be safely ignored for modeling simplicity. However, in cases with high initial salinity such as 23%, ignoring the salt polarization will over-estimate the evaporation rate by about 30%. Hence the simplification needs further justification when used in high salinity cases.

4.4.4 Salinity Effect on Thermal Non-equilibrium of Two Phases

The previous study reported a spray flash evaporation process will generate a thermal non-equilibrium (temperature gap) between the hotter yield vapor and the cooler liquid residue due to the self-heat consumed droplets evaporation. Such a thermal non-equilibrium is positively related to the initial superheat level of the spray. However, this previous work only investigated with pure water, which cannot be directly adopted in spray flash desalination that contains non-volatile fractions (salt). In theory, the salinity effect will reduce such a thermal non-equilibrium between phases due to the decreased evaporation efficiency. Hence the salinity effect to such a thermal non-equilibrium phenomenon in a spray flash desalination is specifically investigated in this section under various initial superheat levels and salinities.

In Figure 4.9, the average temperatures of outlet vapor and outlet spray residue from the chamber after spray flash desalination are plotted corresponding to various initial spray temperatures in three cases of identical salinity (3.5%) but different operating pressures (40kPa, 60kPa, and 80 kPa). The theoretical results are calculated case by case via the process model and presented as data points. Dash lines have been added to interlink each modeling result for showing the tendency. The modeling results are compared with the experimental data, in which each one is averaged from six sets of measurements with the error bar indicating the standard deviation. The solid lines in the figure indicate the saturated temperatures of the pure water corresponded to each operating pressure, without boiling point elevation from the salinity effect.

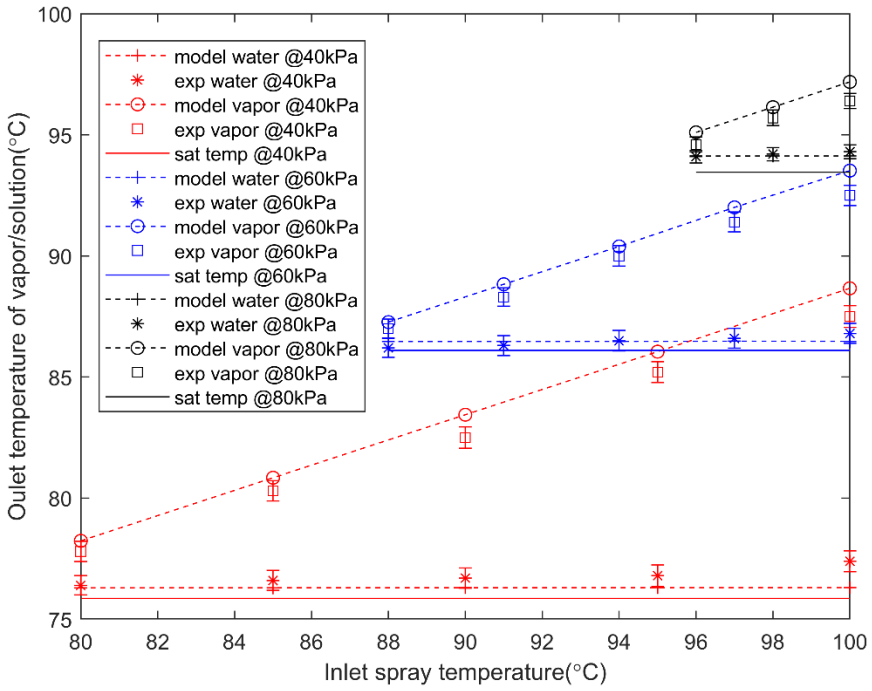

Figure 4.9 Thermal non-equilibrium of two phases under various operating pressures.

In the Figure, an apparent temperature gap between the two outlet phases (vapor and spray residue) can be seen in all cases, which indicates a thermal non-equilibrium between the two phases constantly exists in spray flash desalination. Such a gap is almost positively proportional to the initial spray temperature and could be effectively generated even with low initial superheat levels of the spray. The outlet solution temperature is saturated in all cases, which indicates all those flash processes are completed within the evaporation chamber. It shows the thermal non-equilibrium is positively related to the superheat level of the inlet spray. In addition, theoretical results show larger temperature gaps than experimental results. Such an error could be caused by ignoring the heat interaction between vapor and droplets in the simplified process modeling.

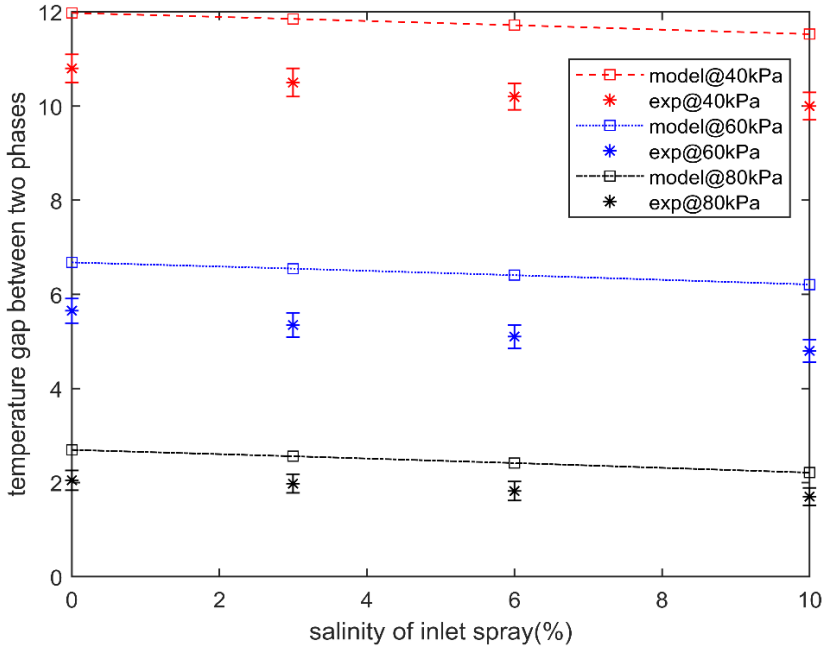

Figure 4.10 Initial salinity vs. temperature gap under various operating pressures.

In addition to the initial superheat level, salinity also plays an important role in affecting the thermal non-equilibrium of the two phases. In Figure 4.10, the outlet temperature difference between vapor and spray residue corresponding to four different initial salinity of the spray (0%, 3%, 6%, and 10%) are plotted under three operating pressures (40kPa, 60kPa, and 80kPa) according to both the process model and the experiments. The inlet spray temperature of these cases is 100℃. Figure 4.10 shows that the initial salinity of the spray negatively impacts the temperature gap. From salinity 0% (pure water) to salinity 10%, the temperature gap in all cases narrows about 10% on average. More specifically, in the figure, the dash-line interlinked each theoretical result is slightly steeper under the case with higher operating pressure, which indicates such a temperature gap in cases with a smaller initial superheat ratio is more sensitive to the salinity variation. That is because such cases have smaller heat storage for evaporation based on Equation (4.1). Nevertheless, the variation of salinity impact (named as “salinity

sensitivity" below) between different superheat levels seems to be small. It is almost unnoticeable in experimental results under the scale of the direct temperature difference ($T_{v,o}$-$T_{w,o}$).

To further evaluate the salinity sensitivity in thermal non-equilibrium of two phases under different superheat levels. Figure 4.11 plots the relations between the thermal non-equilibrium ratio of the two-phase and the initial salinity of the spray by the same cases presented in Figure 4.10. Here, the thermal non-equilibrium ratio is a dimensionless value defined as:

$$\gamma^* = \frac{T_{v,o} - T_{w,o}}{T_0 - T_{sat}} \tag{4.30}$$

Where numerator is the temperature difference between the outlet vapor and the outlet spray residue, the denominator is the temperature difference between the initial spray temperature and the corresponding saturated temperature of pure water. Such a ratio represents a fraction of the thermal non-equilibrium degrees over the maximum superheat degrees in potential (without salt effect). In this way, it is more apparent to see the dash-line becomes negatively steeper in cases with higher operating pressures.

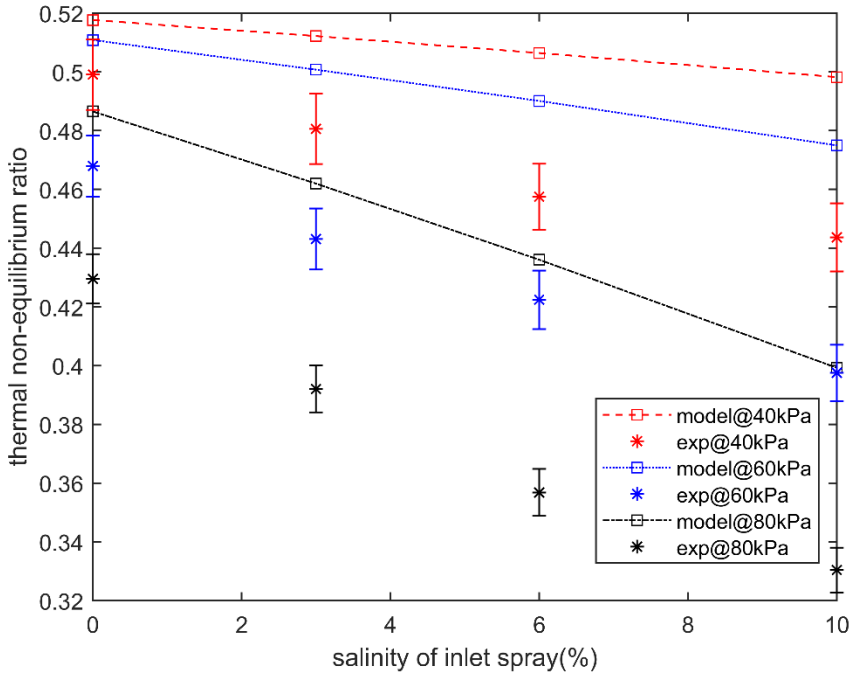

Figure 4.11 Initial salinity vs. temperature gap under various operating pressures.

In Figure 4.11, the thermal non-equilibrium ratios for the three initial salinity values (3%, 6%, and 10%) drop 4%, 7%, and 18% under operating pressures of 40kPa, 60kPa, and 80 kPa, respectively in modeling predictions. While the experimental results show the same tendency with the ratio decrease of 10%, 15%, and 23%, respectively. In summary, the thermal non-equilibrium level between the outlet vapor and spray residue from a spray flash desalination process is negatively impacted by the spray salinity, and such a salinity effect is more sensitive to cases with a lower initial superheat level of the spray.

4.5 Conclusions

In this section, the salinity effect on the process characteristics of spray flash desalination is investigated by an integrated experimental-modeling approach. The process model of spray desalination are proposed via the Lagrangian-Eulerian modeling approach. The

process model comprises the spatially dependent droplets model (SDM) coupled with the 1-D Eulerian vapor flow model. To validate modeling results, an experimental system of static spray flash desalination is built with the active vacuuming extraction. The salinity impacts on curial characteristics of the spray flash process, included evaporation rate and efficiency, internal non-uniformity (or polarization) of thermal and salinity, and thermal non-equilibrium between the two-phase, are parametrically investigated via the process model with experimental validation.

The results show that the evaporation rate of a spray flash desalination process is negatively related to the salinity and positively related to the initial superheat level of the spray. The spray flash desalination can generate apparent thermal and salinity gradients within the droplet. The thermal gradient is continuously reduced along with the process; the salinity gradient will increase first then mitigate due to the coupled effects between the surface salt concentration caused by evaporation and internal salt diffusion. Moreover, although internal salt polarization negatively impacts the evaporation rate and efficiency, such effects can be small (less than 5%) in most industrial spray flash desalination processes. Therefore, it can be safe to approximate the uniformed internal salinity during the modeling to simplify the mathematical complexity and save the computational cost in those applications. However, for cases with high salinity, the salinity polarization can noticeably decrease the process rate and efficiency and cannot be ignored. The thermal non-equilibrium phenomena between phases (vapor and droplets) are conspicuously obtained during the spray flash desalination. Such a thermal non-equilibrium can be effectively generated even with a very low superheat level of the spray and is negatively affected by the salinity. Increasing the salinity from 0 to 10% will reduce the temperature

gap between outlet vapor and spray residue by 10% on average, in cases with various initial superheat ratios from 1.4 to 1.1. The thermal non-equilibrium ratio is more sensitive to the salinity change in cases with higher operating pressure. In other words, the salinity impact on the thermal non-equilibrium phenomena is more noticeable in cases with lower initial superheat levels.

CHAPTER 5

POINT-BASED DROPLET FLASH MODEL

The proposed partial differential equations governed droplet flash models in previous chapters considered the effects of the coupled internal salt diffusion and heat conduction during the flash. However, its mathematical expression is complicated and requires the independent control volume for each droplet to solve. Such a requirement limits the modeling feasibility for many applications, especially in CFD. For CFD simulation of spray flash desalination, the numerous droplets within the spray are usually simplified as non-physical points (such as discrete phase modeling) to reduce the computational cost. Therefore, those point-based droplets can only be modeled by lumped heat capacity method (LHCM). However, the LHCM approximation in flash evaporation will constantly exceed the physical reality and overestimate the evaporation rate due to ignoring the internal heat transfer and salt diffusion. Since a CFD simulation is necessary for this study to investigate the complex non-uniformed vapor-droplet interactions, a point-based modeling methodology of droplet flash is proposed with experimental validation in this chapter.

Specifically, using lumped heat capacity model (LHCM) to describe a droplet evaporation process is one of the most convenient and simplest approaches. However, its assumption of infinitely fast heat conduction within the droplet is constantly beyond the reality in droplet flash cooling, in which the process is typically dominated by the internal heat conduction. Alternatively, an effective heat conduction model (EHCM) considers the limited heat conduction with temperature non-uniformity within the droplet and hence more physics-sound than LHCM. Yet, its governing equations are also much more

complicated than the ones of LHCM. Consequently, applying EHCM could be very difficult in the parametric modeling of many spray flash applications, especially in the point-based discrete phase modeling and associated numerical simulation. Therefore, this paper proposes a modified LHCM for spray flash cooling, which preserves both the accuracy of EHCM and the mathematical simplicity of LHCM. Specifically, a non-dimensional EHCM for droplet flash is developed to provide guidance for determining a case-independent modified evaporation coefficient of LHCM, accompanied with four dimensionless parameters, namely, Fourier number (Fo), flash number (β^*), Biot number (Bi), and radiation number (E*), which are reflecting the characteristic time and heat transfer intensities of latent heat, convection, and radiation, respectively. The corrective coefficient represents the ratio of predicted evaporating rates between EHCM and LHCM, which is a function of Fo and affected by other three operating parameters (β^*, Bi, and E*). The prediction on droplet cooling characteristic (temperature) by modified LHCM matches those of EHCM and available experimental data. The relative errors between the modified LHCM and EHCM are evaluated in cases of a wide operating range (droplet diameters from 0.01 to 1mm, superheat levels from 1.06 to 1.67), and their values are within 3.4%. Parametric studies show the value of the modified coefficient follows a negative correlation with β^* and a positive correlation with Fo. Meanwhile, the heat convection and thermal radiation have negligible impacts (less than 0.1%) on the flash cooling process in our cases, in which values of Bi and E* are relatively small. The most dominant parameter β^* can be used to judge the importance in adopting the corrective coefficient on LHCM.

5.1 Introduction

The flash cooling process of a single-component droplet in a gaseous ambient environment is dominated by two coupled mechanisms: the internal heat transfer of the droplet and the heat and mass transfer between the droplet and its ambient [22]. Specifically, the overall evaporating rate is affected by three factors: the heat transfer within the droplet, the heat transfer (convection and radiation) to/from the ambient, as well as the mass diffusion of vapor in the ambient gas [22], [29]. All the above factors vary with operating conditions, and the one with the slowest transfer rate dominantly limits the evaporating rate.

So far, many mechanistic models have been developed in recent decades to describe the droplet flash cooling process in a depressurized environment, which are based on either lumped heat capacity modeling [35], [39] or heat conduction modeling [33], [34], [42]. The lumped heat capacity model (LHCM) is one of the earliest and most convenient methods to express the droplet evaporation process for the sake of its mathematic simplicity by assuming an infinitely large thermal conductivity of the liquid so that the temperature within the droplet is spatially independent and changed instantaneously [63]. For cases where a droplet evaporates moderately in a non-depressurized environment, such an approximation is tolerable since the heat conduction of the liquid side is usually much faster compared to the heat transfer rate caused by evaporation on the droplet surface [4], [29], [39]. However, when the droplet evaporates intensely and the latent heat is self-supplied by the droplet, such as in the droplet flash cooling, the evaporation rate in the early stage of the process is typically limited by the heat conduction rate within the droplet [5]. In that case, LHCM can be under a very untruthful physical basis and results in numerous errors due to ignoring the limitation of heat conduction rate within the droplet

[42], [64]. Using LHCM to approximate a droplet flash cooling process could dramatically over-estimate the evaporating rate.

The effective heat conduction model (EHCM) can avoid such an over-estimation as well as account for more comprehensive physical mechanisms by considering the heat conduction within the droplet during the evaporation process [22], [42], [64], [86]. However, this method also introduces some inevitable limitations due to the increased mathematical complexity (such as dealing with geometric or control volume details within the droplet and solving partial differential equations), which will significantly increase the computational complexity, if not unendurable, in modeling applications. For example, in order to simulate a spray evaporation process that involves numerous particles (droplets), most computational fluid dynamics (CFD) studies have to adopt the "point-treated" simplification of droplets by discrete phase modeling to reduce the computational cost [2], [17], [71], [83], [87]–[89]. In that case, introducing EHCM into CFD will either require extra individual sub-control volume or introduce additional physical expressions for each droplet, which will dramatically increase the computational cost or even become impossible to realize [90]. Therefore, it is very desirable to search for a more general approach to modify the LHCM of droplet flash cooling while keeping the mathematical simplicity of the modeling.

Improving LHCM has been attempted for cases other than flash cooling [91]–[94]. One way is using trapezoid rule and Hermite approximation to transform the original partial differential problems into a series of ordinary differential problems [91], which has been shown to be efficient in certain applications [92]–[94]. However, as an interpolating data method, that treatment requires a volumetric element (multiple physical nodes) during the

calculation. Therefore, such an approximation not only still remains relatively complicated in mathematical form, but also cannot be realized in our objective application (spray flash cooling via Lagrangian-Eulerian based CFD), in which the discrete phase (droplets) is treated as a single non-spatially physical-node.

In conclusion, to improve the accuracy of LHCM in predicting droplet flash cooling process while keeping the same mathematical simplicity, a modeling methodology to correct LHCM is proposed as the modified LHCM in this section. Firstly, EHCM of droplet flash cooling with Hertz-Knudsen evaporating expression is presented to provide referential results. Then, to realize the case-independent modification, the EHCM is converted into dimensionless forms, accompanied by newly-defined dimensionless parameters for categorizing process behaviors in mass transfer, thermal convection and radiation in the energy and evaporation equations and associated boundary conditions. Further, the modified LHCM is established by introducing a corrective coefficient on the evaporation equation based on the original LHCM. Such a coefficient is determined by analyzing the results of evaporation residue between EHCM and the original LHCM. Predictions of both EHCM and modified LHCM are validated against experiments and meet a good agreement. Results of the original LHCM are also plotted as a contrast to show computational improvement in predicting instantaneous droplet temperature during the process by modified LHCM. The predicted tolerance of modified LHCM against EHCM is compared and discussed under a wide range of under typical operating conditions. To investigate the effect of major operating characteristics in typical flash cooling (*e.g.*, droplet velocity, droplet size, initial droplet temperature, and operating pressure) on the process intensity, as well as the correlations between dimensionless parameters and the

corrective coefficient, a series of parametric studies are performed. A polynomial-fitted empirical relation for determining the coefficient value under specific droplet size and characteristic time (Fourier number) is exemplified for a typical case. To investigate whether convection and radiation can be ignored for mathematical simplification, their heat transfer weighting during the process is also parametrically accessed.

5.2 Effective Heat Conduction Model and Its Nondimensionalizaiton

In this section, the original LHCM is modified by introducing a modification coefficient to the evaporation equation to improve the accuracy in predicting a droplet flash cooling process. Such a coefficient is determined based on the comparison of predictions between LCHM and ECHM. Therefore, an EHCM of droplet flash cooling needs to be developed first to provide referential results.

Consider a single-component droplet is under flash evaporation and cooling in a thermal-insulated depressurized environment. Assuming: (1) the droplet formation is instant and perfectly spherical; (2) the transport phenomena and physical properties of the droplet are symmetrical; (3) the internal cavitation is ignored so that all evaporation happens on the droplet surface. Meanwhile, since the momentum effect on heat/mass transfer characteristics during the process can be approximated as model-insensitive [5], velocities of the droplet and its surrounded vapor are predetermined in both LHCM and EHCM for simplification to focus on the comparison of heat/mass transfer. Then the heat conduction within the droplet of EHCM is:

$$\frac{\partial}{\partial t}\left(\rho_d c_d T_d\right)=\frac{1}{r^2}\frac{\partial}{\partial r}\left(r^2 k_{eff}\frac{\partial T_d}{\partial r}\right) \tag{5.1}$$

where r is the radial coordinate centered in the droplet, T_d is the time-dependent local temperature within the droplet, c_d is the specific heat of the droplet, and k_{eff} is the effective thermal conductivity, which is determined as [95]:

$$k_{eff} = 1.86k + 0.86k \tanh\left[2.245 \log_{10}\left(\mathrm{Pe}/30\right)\right] \tag{5.1a}$$

where Pe is the Peclet number of droplet. Assume that the initial temperature within the droplet is uniform so that:

$$T_d(r,0) = T_{d0} \tag{5.1b}$$

The boundary conditions are given by the symmetric assumption at the droplet center and heat transfer balance at the droplet surface, respectively expressed as:

$$\frac{\partial T_d}{\partial r} = 0 \qquad at\ r = 0 \tag{5.1c}$$

$$\pi d_d^2 k_{eff} \frac{\partial T_d}{\partial r} = -L_{fg}\dot{m}_v - h_m \pi d_d^2 (T_d - T_v) - \frac{\delta\left(T_d^4 - T_{ch}^4\right)}{\left(\frac{1-\varepsilon_d}{\varepsilon_d \pi d_d^2} + \frac{1}{\pi d_d^2 F_{d,ch}} + \frac{1-\varepsilon_{ch}}{\varepsilon_{ch} A_{ch}}\right)} \quad \text{at } r = \frac{d_d}{2} \tag{5.1d}$$

where L_{fg} is the latent heat, h_m is the convective heat transfer coefficient, which may be approximated using Ranz and Marshall correlation [63] with vapor-film properties and relative droplet velocity. The third term on the right hand is the radiation between the droplet and chamber. T_{ch} is the temperature of chamber wall, and A_{ch} is the surface area of chamber wall.

The evaporation rate is governed by the pressure difference between the saturated vapor pressure at the droplet surface and the ambient pressure controlled by vacuuming. Hence, assuming no temperature slip over the droplet interface (*i.e.*, surface vapor

temperature is the same as the surface droplet temperature), the evaporation rate could be determined from the modified Hertz-Knudsen relation [26]:

$$\dot{m}_v = \alpha \pi d_d^{\,2} \sqrt{\frac{M_v}{2\pi R_u T_{ds}}} \left(P_v - P_\infty \right) \tag{5.2}$$

where α is the evaporation coefficient (which is an empirical constant to be determined from the experiment [5], [72], [96]), M_v is the molecular weight of vapor, R_u is the universal gas constant of ideal gases, P_v is the saturated vapor pressure at droplet surface, P_∞ is the ambient pressure, and T_{ds} is the droplet surface temperature.

It should be noted that Equation (5.2) is established on the evaporation over a flat interface, without the consideration of the surface tension effect [97]. In reality, the curvature of the droplet will introduce a higher pressure in the liquid side by surface tension and require higher surface energy to realize evaporation, compared with the case on a flat surface [98]. Therefore, the P_v in Equation(5.2) needs to be corrected by Kelvin equation [99]:

$$\ln \frac{P_v}{P_v^\infty} = \frac{4\sigma V_m}{R_u T_{ds} d_d} \tag{5.3}$$

where P_v^∞ is the saturated vapor pressure on a flat surface (infinite radius), T_d is the temperature on droplet surface, σ is the surface tension, and V_m is the molar volume of the liquid.

The Surface tension σ in Equation(5.3) is also related to droplet size and temperature [100]. The size effect to surface tension for a spherical isotropic liquid drop can be approximated by Tolman equation [60], [101]:

$$\sigma = \frac{\sigma^{\infty}}{1 + 4\delta / d_d} \tag{5.3a}$$

where σ^{∞} is the surface tension of a flat surface, and δ is the Tolman length, which is represented by the difference between the tensional surface and the equimolar surface [102]. In addition, the temperature effect on surface tension can be determined by a polynomial fit of experimental data, in which the measurements are performed under a thermal-equilibrium status of water evaporation [103]. It is worth mentioning that the correction of evaporative pressure caused by surface tension usually is only necessary for very small droplets (*e.g.*, of a few micrometers or at nanometer scale) and can be ignored in most applications with relative bigger droplets (*e.g.*, at millimeter scale), in which the Tolman length is usually six orders of magnitude smaller than the droplet radius [102], [104].

With the further approximation of ideal gas for the saturated vapor and the gas phase only consists of evaporated vapor, the saturated vapor pressure can be related to the droplet surface temperature by Clausius-Clapeyron equation:

$$\ln \frac{P_v^{\infty}}{P_{\infty}} = -\frac{L_{fg} M_v}{R_u} \left(\frac{1}{T_{ds}} - \frac{1}{T_{\infty}} \right) \tag{5.3b}$$

where T_{∞} is the saturated temperature at P_{∞}.

During the evaporation, the droplet size keeps decreasing due to the mass loss from the phase change. According to the mass balance as well as the volume-diameter relationship, we have:

$$\frac{dm_d}{dt} = -\dot{m}_v \tag{5.4}$$

$$m_d = \rho_d \frac{\pi}{6} d_d^{\,3} \tag{5.5}$$

Eventually, the closed form of ECHM of droplet flash cooling is established, with five governing equations (Equation (5.1) – Equation (5.3), Equation (5.4), and Equation (5.5)) for five unknowns (T_d, m_v, P_v, m_d, and d_d).

However, to parameterize the model and establish a generalized correcting criterion for LHCM that is case-independent, the energy and evaporation equations in EHCM should be expressed in a dimensionless format. Therefore, a dimensionless EHCM is proposed below, accompanied by new defined dimensionless parameters for categorizing process behaviors in mass transfer, convection, radiation, etc. According to the above equations, the EHCM and its boundary conditions expressed in the dimensionless form are:

$$d^{*2} \frac{\partial \theta^*}{\partial Fo} = \frac{1}{r^{*2}} \frac{\partial}{\partial r^*} \left(r^{*2} \frac{\partial \theta^*}{\partial r^*} \right) \tag{5.6}$$

$$\theta_0^* = \frac{T_0}{T_\infty} \qquad \text{at} \quad \mathrm{Fo} = 0 \tag{5.6a}$$

$$\frac{\partial \theta^*}{\partial r^*} = 0 \qquad \text{at } r^* = 0 \tag{5.6b}$$

$$\frac{1}{d^*} \frac{\partial \theta^*}{\partial r^*} = \beta^* \left\{ \frac{1 - O^* \exp\left(\frac{L^*(1-\theta^*)}{\theta^*} \right)}{\sqrt{\theta^*}} \right\} + \mathrm{Bi}\left(1 - \theta^*\right) + \mathrm{E}^* d^* \left(\theta^{*4} - Y^* \right) \text{ at } R^* = 1 \tag{5.6c}$$

where the dimensionless superheat ratio, radius ratio, Fourier number, reduced diameter, and the ratio of chamber wall temperature over thermal equilibrium temperature of vapor are respectively defined by:

$$\theta^* \equiv \frac{T_d}{T_\infty} \qquad r^* \equiv \frac{2r}{d_d} \qquad \mathrm{Fo} \equiv \frac{4k_{eff}t}{\rho_d c_d d_0^2} \qquad d^* \equiv \frac{d_d}{d_0} \qquad Y^* = \frac{T_C^4}{T_\infty^4} \tag{5.6d}$$

It is noted that β*, O*, L* and Bi are all dimensionless parameters, which stand for, flash evaporation, the coefficient of effective vapor pressure, latent heat as well as the effective Biot number of heat convection, respectively:

$$\beta^* \equiv \frac{L_{fg}\alpha d_0 P_\infty}{2k_{eff}}\sqrt{\frac{M_v}{2\pi R_u T_\infty^3}} \qquad O^* \equiv \frac{4\sigma V_m}{R_u T_d d_d} \qquad L^* \equiv \frac{L_{fg}M_v}{R_u T_\infty} \qquad \mathrm{Bi} \equiv \frac{h_m d_0}{2k_{eff}} \tag{5.6e}$$

Also, the dimensionless parameter E* in radiation item is defined as:

$$\mathrm{E}^* = 1/\left[\frac{2k_{eff}}{\sigma T_\infty^3 \pi d_0}\left(\frac{1-\varepsilon_1}{\varepsilon_1} + \frac{1}{F_{12}} + \frac{(1-\varepsilon_2)A_1}{\varepsilon_2 A_2}\right)\right] \tag{5.6f}$$

Meanwhile, the reduced diameter, d^*, is a time-dependent variable due to evaporation. By substituting Equation (5.2) and Equation (5.6) into Equation (5.5), the reduced diameter is governed by:

$$\frac{dd^*}{d\mathrm{Fo}} = -\mathrm{Ja}\beta^*\left(1 - O^*\exp\left(\frac{L^*(1-\theta^*)}{\theta^*}\right)\right)\Big/\sqrt{\theta^*} \tag{5.7}$$

where Ja is the Jakob number, defined by

$$\mathrm{Ja} \equiv \frac{c_l T_\infty}{L_{fg}} \tag{5.7a}$$

Finally, the closed form of dimensionless EHCM is established by the non-dimensionalization of energy equation (Equation (5.6)) and evaporation equation (Equation (5.7)) with two unknowns θ^* and d^*.

5.3 Modified Lumped Heat Capacity Model

Although the dimensionless EHCM provides a parameterized way to evaluate process characteristics, the specific corrective coefficient for modifying LHCM needs to be determined case by case due to the mathematical complexity. In this section, a general analysis methodology of coefficient determination for modified LHCM is proposed and explained with the help of an exemplary case study. This case considers a typical droplet evaporating in a spray flash cooling process. Specifically, a droplet of 1mm diameter, with an initial temperature of 100℃, is suddenly injected and settles by gravity in a 0.6 atm depressurized environment filled with saturated vapor.

Based on dimensionless EHCM, a typical result is illustrated in Figure 1 under process parameters of β^*=78.8, Bi=0.0069, and E*=1.113×10^{-9}. It reveals the relationships among the superheat ratio (θ^*), dimensionless radial position (r^*), and the characteristic time (Fo), clearly showing a transient process from an initial state of strong thermal non-equilibrium and non-uniformity within the droplet toward an equilibrium state with uniformity.

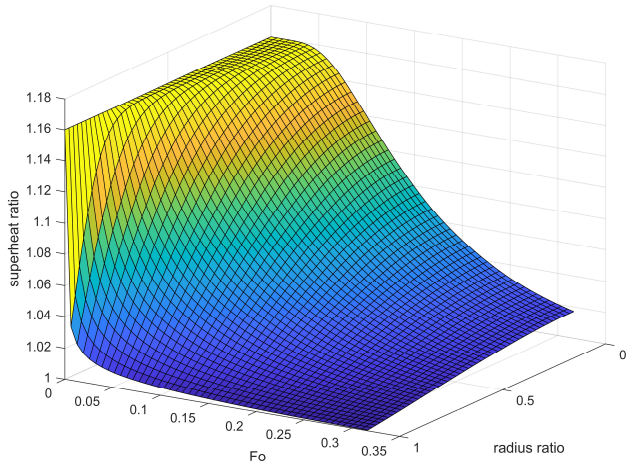

Figure 5.1 Typical dimensionless distributions of superheat within a droplet vs. time.

Next, the difference in droplet evaporation predicted by LHCM and EHCM under the same operating conditions can be calculated. It is noted that, based on Equations (5.2), (5.5) and (5.6), the evaporation residue can be defined in terms of reduced diameter as

$$m_d^* \equiv \frac{m_d - m_{d\infty}}{m_{d0} - m_{d\infty}} = \frac{d^{*3} - d_\infty^{*3}}{1 - d_\infty^{*3}} \tag{5.8}$$

where m_{d0} and $m_{d\infty}$ represent the initial and the equilibrium droplet mass, respectively. Such a comparison is exemplified via Figure 5.2. In the figure, LHCM shows a higher evaporation rate compared with EHCM, which is due to its problematic assumption of uniform temperature distribution that over-estimates the surface temperature during the droplet evaporation. A sampling range is defined from the evaporation residue of 1 to 0.01, representing the flash process up to 99% completion in evaporation. Within this range, the evaporation residues from both models decrease in a nearly exponential trend along with Fourier number (or linearly in the semi-log scales as shown in Figure 5.2), which further suggests:

$$m_d^* = \exp\left(-\lambda \mathrm{Fo}\right) \tag{5.9}$$

where λ is the slope in the linear curve fitting in the semi-log scales. Further, based on the fitted trending line, we have:

$$\ln m_{dE}^* = -\lambda_E t \quad \text{and} \quad \ln m_{dL}^* = -\lambda_L t \tag{5.10}$$

$$m_{dE}^* = m_{dL}^* \exp\left(-(\lambda_E - \lambda_L)t\right) \tag{5.10a}$$

where the subscripts E and L stand for the effective conduction model and lumped heat capacity model, respectively.

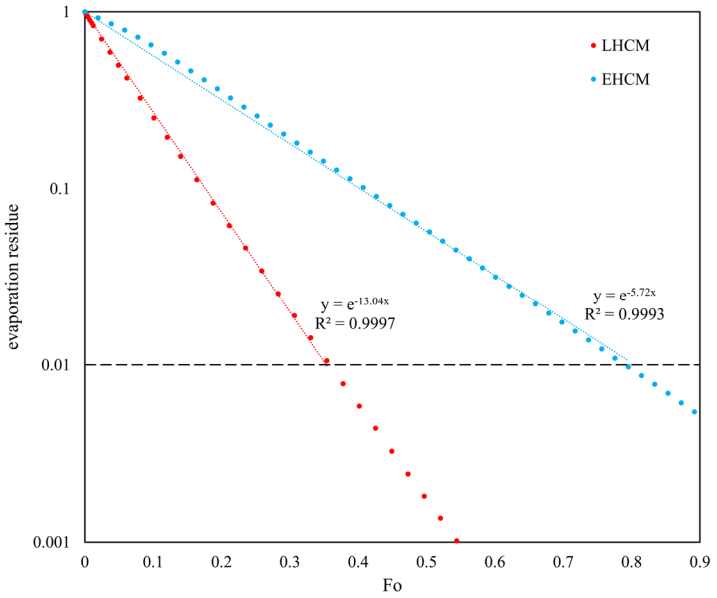

Figure 5.2 An exemplary linear fitting of evaporation residue vs. Fo (β*=78.8, Bi=0.0069, and E*=1.113×10^{-9}).

Therefore, a corrective coefficient (α_L) on the droplet evaporation rate predicted by LHCM to approach the value predicted by the effective heat conduction model can be defined by:

$$\frac{\dot{m}_{vE}}{\dot{m}_{vL}} = \frac{\left(\frac{dm_d}{dt}\right)_E}{\left(\frac{dm_d}{dt}\right)_L} = \frac{dm^*_{dE}}{dm^*_{dL}} = \frac{\lambda_E}{\lambda_L}\exp\left(\left(\lambda_L - \lambda_E\right)\mathrm{Fo}\right) \equiv \alpha_L \tag{5.11}$$

Further, the energy equation to express the droplet flash cooling in modified LHCM can be determined as:

$$m_d c_d \frac{dT_l}{dt} = -L_{fg}\dot{m}_v - h_m \pi d_d^2 (T_l - T_v) - \frac{\sigma\left(T_l^4 - T_C^4\right)}{\left(\frac{1-\varepsilon_1}{\varepsilon_1 \pi d_d^2} + \frac{1}{\pi d_d^2 F_{12}} + \frac{1-\varepsilon_2}{\varepsilon_2 A_2}\right)} \tag{5.12}$$

where m_v now is expressed by:

$$\dot{m}_v = \alpha_L \cdot \alpha \pi d_d^{\,2} \sqrt{\frac{M_v}{2\pi R_u T_{ds}}} \left(P_v - P_\infty\right) \tag{5.13}$$

Finally, similar to EHCM, the modified LHCM is closed with five governing equations (Equation (5.12), Equation (5.13), Equation (5.3), Equation (5.5), and Equation (5.6)) for the corresponding five unknowns (T_d, m_v, P_v, m_d, and d_d).

5.4 Results and Discussion

In this section, the predicted results of EHCM and modified LHCM are validated with the experiments. The prediction tolerance of the modified LHCM is discussed and compared against EHCM. The modified LHCM is also compared with the original LHCM. A series of parametric studies have been performed to reveal the correlations between different processing parameters (β*, Bi and E*) and the coefficient, as well as to propose a parametrized criterion on the necessity of adopting the correction on LHCM for flash cooling applications. The internal temperature non-uniformity of the droplet and the heat transfer rates by convection and radiation during the process are also parametrically discussed.

5.4.1 Model Validation

Both predicted results of EHCM and modified LHCM are validated with experiments in this section. For a spray flash cooling process in a thermally-insulated environment, the latent heat is self-provided by the spray so that the flash evaporation process comes with the temperature decrease of droplets. Such a temperature change has been a crucial characteristic for the experimental measurements of the flash process [2], [5], [9], [19], [20]. Hence in this work, the average temperature of the droplet is measured along with the

traveling trajectory for model validations. Correspondingly, since the evaporation rate is directly proportional to the evaporating area (Equation (5.2)) while the inertia-dominated penetration is proportional to the volume of droplet, the Sauter Mean Diameter is adopted as the average size of droplets in the model computation to represent the overall evaporation and transport process of the spray, which is determined from the measured size distribution in experiments. In addition, since some physical properties of both droplets and vapor will change in certain degrees during the flash cooling process, in our work, their densities, specific heats, viscosities, and the latent heat are adopted from temperature-depended polynomial functions, which are determined from the published data of thermophysical properties table of the saturated water [63].

The setup of the experimental system and the measurement methodology are reported in previous work [83]. The experiments are performed under two operating conditions corresponding to different operating pressures, 0.4 atm and 0.6 atm, respectively. The spray characteristics (droplet size distribution and velocity) are also measured to determine the initial conditions for theoretical calculation [83]. The detailed key operating conditions of both experiments and models are listed in Table 5.1.

Table 5.1 Key Geometric and Operation Parameters

Parameter	Value	Unit
Spray pattern	Full-cone	-
Spray angle	57	°
Nozzle location	Top center	-
Spray injection velocity	3.23	m/s
Spray liquid	water	-
Spray flow rate	44.1	ml/s
Droplets Sauter mean diameter	0.42	mm
Chamber height	0.5	m

Table 5.1 Key Geometric and Operation Parameters (continued)

Chamber diameter	0.3	m
Parameter	Value	Unit
Vapor outlet diameter	0.75	inch
Liquid outlet diameter	0.5	inch
Spray initial temperature	94	°C
Chamber vacuum pressure	0.4/ 0.6	atm
Chamber material	Stainless steel with insulation	N/A

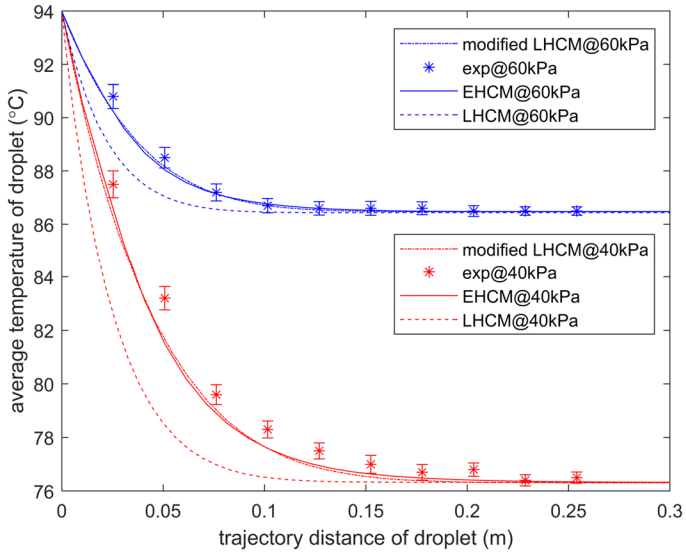

Figure 5.3 Droplet temperature vs. travel distance during the flash cooling.

Figure 5.3 shows model validations of both EHCM and modified LHCM compared against the experiments under two different operating pressures, based on the average temperature of the droplet along with its trajectory. The prediction of LHCM is also presented to show the improvement in accuracy of the modification. In these cases, the λ_E/λ_L are adopted as 5.58/13.95 and 5.77/14.73, corresponding to the operating pressures 0.4 and 0.6 atm, respectively. The modified LHCM is shown to meet a good agreement with both EHCM and experiments, compared to about 100% error margin caused by the original LHCM in terms of the processing time. A larger deviation in relative errors is noticed for the case at

40 kPa operating pressure, in which the flash evaporation is more intense. Such deviation may be resulted from the larger fluctuation of temperature measurements and/or the larger bias to the modeling hypothesis of quasi-thermal-equilibrium.

5.4.2 Accuracy and Applicability

The modeling applicability or limitation depends on the acceptance level of modeling assumptions as well as the tolerance in prediction accuracy. Although improved accuracy of our modified LHCM is realized by adding a corrective coefficient in the evaporation equation, it is not intuitive to directly compare the evaporation rate among different models for tolerance evaluation. Since the flash evaporation rate is not only determined by the evaporation coefficient, but also heavily coupled with the internal temperature gradient within the droplet as well as the pressure difference between the droplet and the environment. Alternatively, the influence of evaporation rate is related to a reduction in droplet temperature during the flash cooling process. Therefore, the accuracy in prediction by modified LHCM is evaluated in terms of droplet temperature.

The model accuracy is evaluated within an operating range (droplet size 0.01~1mm, operating pressure 0.2~0.8 atm) referenced from the application of spray flash desalination, which is one of the most common industrial processes involving droplet flash cooling (Eltawil, et al. 2009; Hou et al. 2010; Miyatake et al. 2001). Here, the relative error at a specific processing moment is defined by comparing the volume-averaged droplet temperatures between LHCM and EHCM, which varies with time (or traveling distance) during a process. Within the above operating conditions, the relative errors of the modified LHCM range from 0 to 4.6% compared against EHCM. Specifically, to evaluate the exact relative errors for an entire flash evaporation process, the maximum error, the minimum

error, and the average value of all errors are presented. Table 2 listed the error analysis in six cases with three droplet sizes (0.01mm, 0.1mm, 1mm) and two operating pressures (0.2atm and 0.8atm).

Table 5.2 Exemplified Relative Errors Between Modified LHCM and EHCM

droplet size (mm)	0.01		0.1		1	
operating pressure(atm)	0.2	0.8	0.2	0.8	0.2	0.8
maximum error (%)	0.678	0.527	1.36	1.34	4.64	4.62
minimum error (%)	0.051	0.059	0.0164	0.0196	0.0531	0.0124
average error (%)	0.0181	0.0201	0.253	0.267	0.92	1.04

Table 5.2 shows that the average error of each case noticeably follows a positive relation with the droplet size, and also slightly increases with the higher operating pressure. In fact, the predicted difference of flash rate between the original LHCM and EHCM is also following the same changing tendency (will be discussed in later sections). Therefore, to present the most significant difference in droplet temperatures between models, the case of 1mm droplet flash cooling under 0.8 atm (selected by the largest droplet size and highest operating pressure) is particularly presented in Figure 5.4. The results clearly indicate that the modified LHCM largely improves the prediction accuracy compared with the original LHCM, with the latter over-estimating the evaporation rate by almost five times. In addition, the average computational time of modified LHCM in our exemplary cases is about 66% quicker than EHCM (~0.25s vs. ~0.74s).

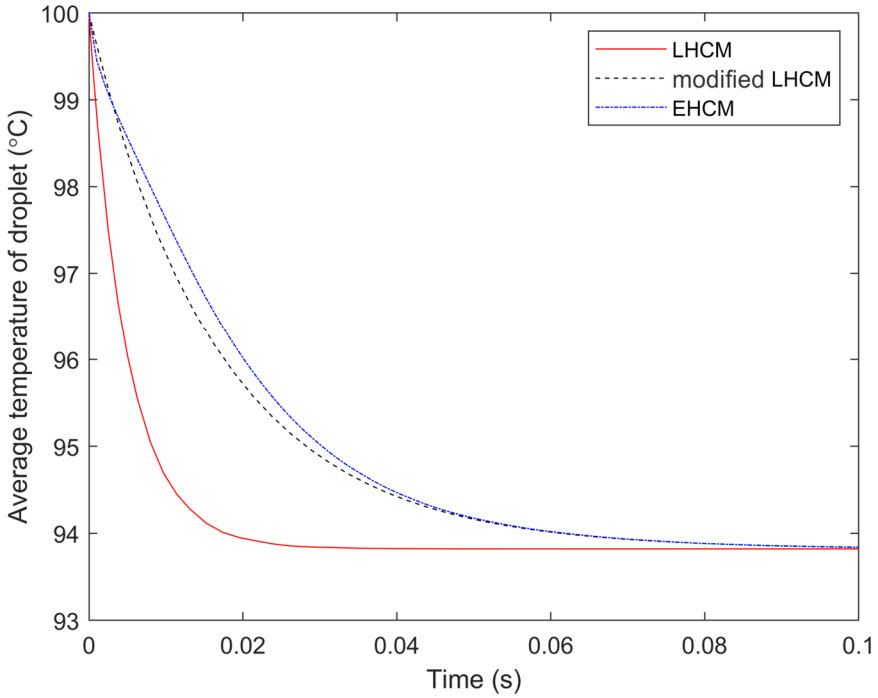

Figure 5.4 Models comparison of predicted droplet's temperature.

5.4.3. Droplet Size Effect on Model Correction

In this section, the droplet size effect on the prediction of evaporation residue (Equation(5.8)) versus Fourier number (Fo) by the original LHCM and EHCM is investigated under the same operating condition of 100°C initial temperature and 0.4 atm operating pressure with three different droplet diameters 1mm, 0.1mm, and 0.01mm. The results of LHCM and EHCM models are compared in Figure 5.5.

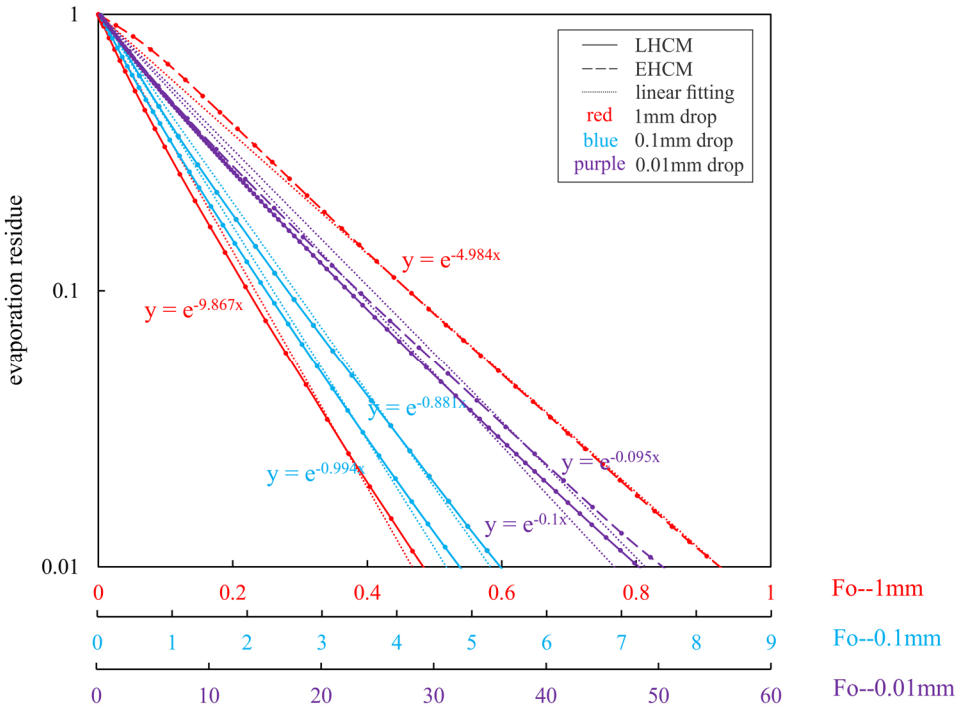

Figure 5.5 LHCM vs EHCM with different droplet sizes (red)1mm; (blue)0.1mm; (purple)0.01mm.

Based on results, with the droplet of 1mm, 0.1mm, and 0.01mm, the ratios λ_E/λ_L are 0.505, 0.886, and 0.95, respectively. With the decrease of droplet diameter, the difference in the processing rate (reflected as evaporating residue) narrows between LHCM and EHCM, indicating the approximation of LHCM is becoming better. The corresponding dimensionless parameters are: β^* = 63.09 /6.309 /0.6309, Bi = 0.011 /0.0011 /0.0011, and E* =9.8×10^{-10} /9.8×10^{-11} /9.8×10^{-12}, respectively. From the results and Equation (5.6c), it is shown that the larger values of these three dimensionless parameters represent more intense heat and mass transfer between the droplet and its surrounded environment, which indicates a larger difference in the computational results between the two models. Such a tendency is also obtained in Sub-section 5.4.4 and will be further discussed in Sub-section 5.4.5.

5.4.4 Superheat Ratio Effect on Model Correction

In a droplet flash cooling process, with a given initial temperature of the droplet, different operating pressures will determine different initial superheat ratios and affect the evaporation intensity. In this section, the superheat ratio effect is parametrically studied in the cases under the same operating condition of 100℃ initial temperature and 1mm droplet diameter with three different operating pressures 0.6atm, 0.4atm, and 0.2atm, corresponding to initial superheat ratios (θ^*) of 1.16, 1.32, and 1.67. The results of the original LHCM and EHCM are compared in Figure 5.6.

Based on results, with operating pressures of 0.6atm, 0.4atm, and 0.2atm, the corresponding ratios of $\lambda_E/\ \lambda_L$ are obtained as 0.438, 0.505, and 0.606, respectively. It indicates that, with the decrease of the operating pressure (increasing the initial superheat ratio), the computational difference in evaporating rate between two models becomes smaller, which means the approximation of LHCM is more acceptable. This makes sense because, with an increased evaporating tensity under lower operating pressure, the temperature gradient within the droplet becomes larger and results in a higher internal heat transfer rate, which will further prompt the evaporation rate in EHCM calculation. Meanwhile, such processes under different operating pressures from high to low are corresponding to different β^* (90.70 ／63.09 / 33.83) with the same Bi (0.011) and E* (9.8×10^{-10}). Hence, the higher dimensionless parameter β^* indicates a larger difference in processing prediction and requires a higher necessity of introducing the correction to LHCM. As in an agreement with Section 5.4.3, these dimensionless parameters could provide quantitative guidance on whether LHCM needs to be modified according to specific requirements in different applications.

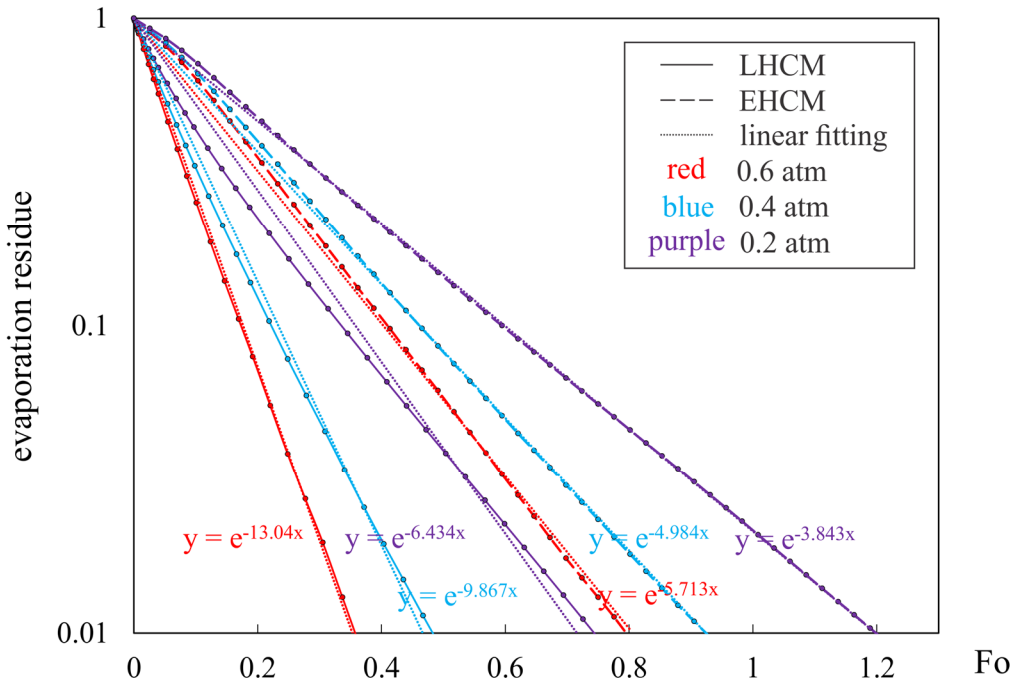

Figure 5.6 LHCM vs EHCM under different operation pressure (red) 0.6 atm; (blue) 0.4 atm; (purple) 0.2 atm.

5.4.5 Tendency of Correction vs. Fo

According to Equation (5.11), the corrective coefficient is a function of the Fourier number, which is further determined by the droplet size as well as processing time. Therefore, as long as operating conditions are given (*i.e.*, initial temperature and operating pressure), an empirical relation of the coefficient value can be determined by polynomial curves fitting based on parametric studies, which is a function of Fourier number and droplet size.

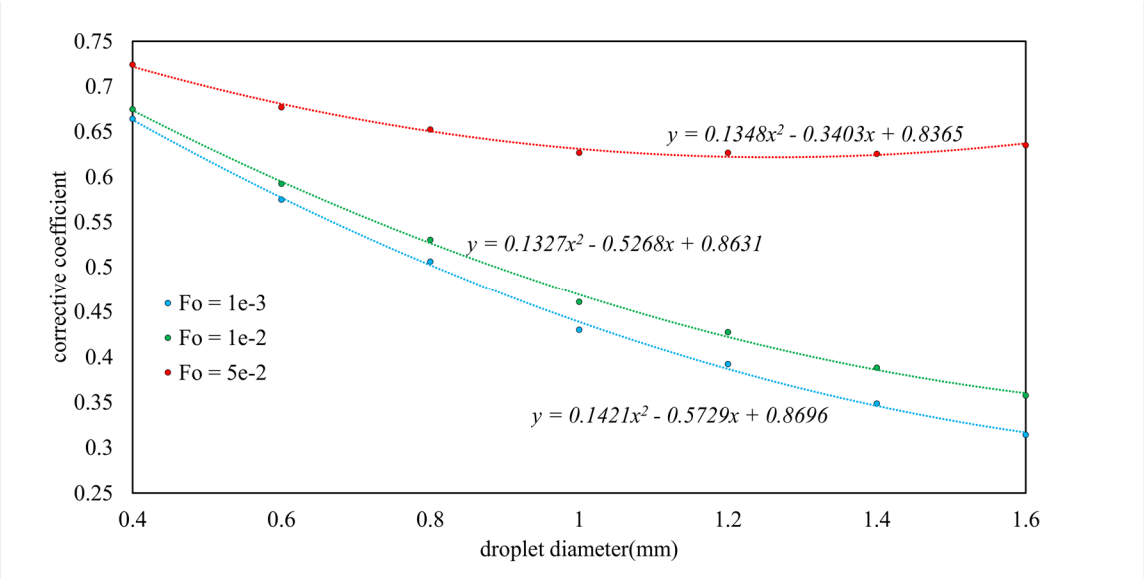

Figure 5.7 Tendency of coefficients with different Fo.

A series of empirical relations are exemplary calculated under the operating condition of 100℃ initial temperature and 0.4atm operating pressure, which are plotted according to different Fourier numbers in Figure 5.7. Three curves in the figure present the relation between coefficient values and droplet sizes under three different Fourier numbers, corresponding to three different processing moments. It shows that the coefficient value decreases with the increase of droplet size, which agrees with the discovery in Section 5.4.3. It also shows that the coefficient value increases along with the processing time, which makes sense because EHCM will remain at a relatively higher evaporating temperature in the latter period of the evaporation process and hence obtain a larger evaporation rate comparing against LCHM.

5.4.6 Temperature Non-uniformity with Different Parameters

Sub-sections 5.4.3 to 5.4.5 reveal how the three dimensionless parameters (β*, Bi, and E*) reflect heat transfer intensity between the droplet and its ambient. Similarly, these parameters can also dominate the level of temperature non-uniformity within the droplet.

According to Equation (5.6c), the more intense the flash evaporation is, the larger thermal non-uniformity will present within the droplet. Such an evaporating intensity will be majorly reflected by the value of parameter β^*, in which the impacts of convection (Bi) and radiation (E*) remain very small during the process (will be further clarified in Section 5.4.7). Therefore, only the impact of parameter β^* on temperature non-uniformity of the droplet is parametrically investigated.

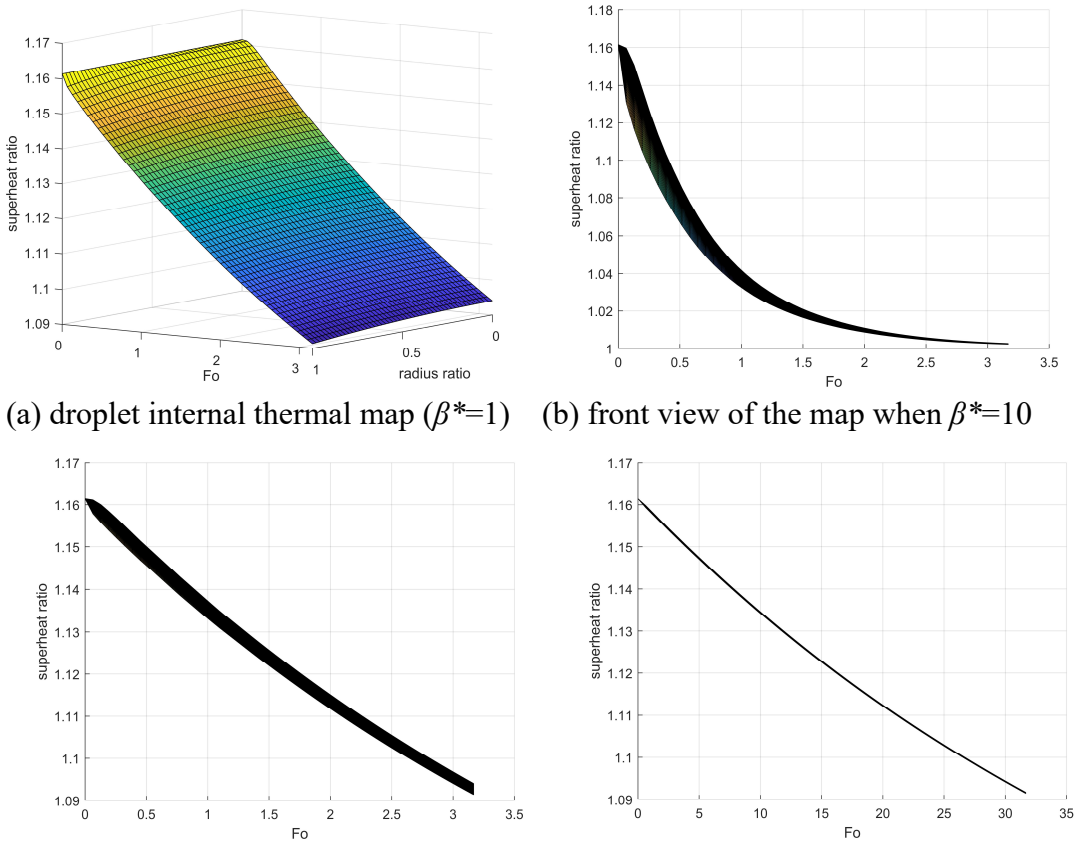

(a) droplet internal thermal map (β^*=1) (b) front view of the map when β^*=10

(c) front view of the map when β^*=1 (d) front view of the map when β^*=0.1

Figure 5.8 Dimensionless internal thermal non-uniformity of the droplet.

Figure 5.1 shows a temperature map of a flash cooling droplet under conditions of β^*=78.8, Bi=0.0069, and E*=1.113×10^{-9}, in which we can tell from the value that the latent heat contributes mostly in overall heat transfer and the evaporating rate is fairly large.

However, when the parameter β^* becomes smaller, the temperature distributions within droplets will become more uniform during the flash cooling, as illustrated in Figure 5.8(a) (β^*=1). Figures 5.8(b)-(d) show front views of temperature maps under the operating conditions of different values of β^* (10, 1, and 0.1) but with the same Bi (0.0069) and E* (1.113×10-9). In each figure, the top edge represents the local superheat ratio in the droplet center, and the bottom edge represents the local superheat ratio on the droplet surface. The gap (dark zone in figures) between such two edges represents the instant internal temperature non-uniformity (in terms of superheat level) versus characteristic time (Fo). With the decrease of β*, the temperature gradient within the droplet reduces, and the LHCM approximation becomes closer to ECHM.

5.4.7 Heat Transfer Weights of Convection and Radiation

Although the heat transfer rates of convection and radiation in a droplet flash cooling process are usually very low compared with the latent heat transfer rate, they can dramatically increase the mathematical complexity of the governing equations and the computational cost. Therefore, it is meaningful to parametrically evaluate the heat transfer weights of convection and radiation for the necessity of inclusion. The parametric study in this section simulates a simple droplet flash cooling process that assuming an initially superheat droplet settles by gravity in a thermal-insulated chamber, which is evenly filled up with the saturated vapor corresponding to the specific depressurized operating pressure. The droplet is assumed to be perfectly spherical without collision or break-up during the process. Further, in convective heat transfer, it assumes: 1. the gaseous phase (vapor) has a uniform upward relative velocity under the referential coordinates of the settling trajectory of the droplet; 2. the convective heat transfer coefficient is approximated using

Ranz-Marshall correlation with vapor-film properties and relative droplet velocity [63]. For thermal radiation, it assumes: 1. the chamber temperature is uniformly distributed and remains unchanged during the process; 2. the view factor from the droplet to the chamber wall is one; 3. the absorption, reflection, and emission of the gaseous phase (vapor) is ignored.

The heat transfer rates of convection and latent heat are compared during the flash cooling process under different operating conditions in terms of jetting velocity, droplet size, and operating pressure. Figures 5.9(a)-(c) shows the ratio of heat transfer rates between the convection and the latent heat versus superheat ratio in processes corresponding to different parameters. Figure 5.9(a) illustrates the effect of injection velocity, with a 1mm droplet at the initial temperature of 100℃ evaporating under 0.6atm operating pressure, at different injection velocities of 3m/s, 10m/s, and 30 m/s, respectively. Figure 5.9(b) shows the effect of droplet diameter, with the exemplified case of the droplet at the initial temperature of 100℃, 3m/s injection velocity, and evaporating under 0.6 atm operating pressure, with different initial diameters of 0.1mm, 0.6mm, and 3mm, respectively. Figure 5.9(c) demonstrates the effect of operating pressure, with the case of 1mm droplet at the initial temperature of 100℃, 3m/s injection velocity, and evaporating under different operating pressures 0.2, 0.4, 0.6, and 0.8 atm, respectively.

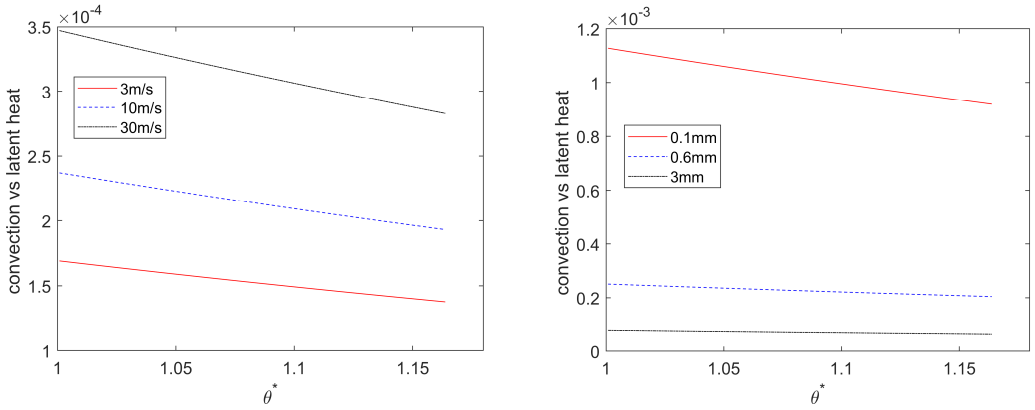

(a) effect of injection velocities (b) effect of droplet diameters

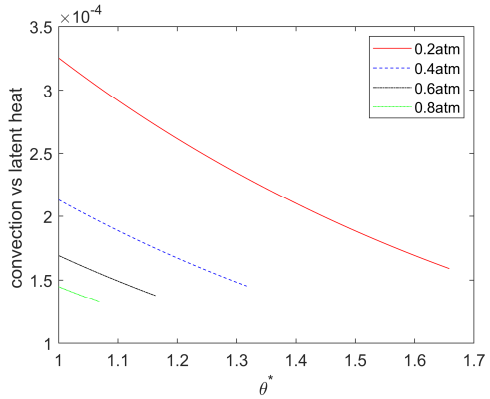

(c) effect of operating pressures

Figure 5.9 Heat transfer weight of convection against latent heat.

From the results, we can see a common tendency that, with the decrease of the superheat ratio, the heat transfer weight of the convection increase due to the evaporation becoming weak. However, even so, the maximum value can only achieve about 0.001 in the case of the smallest droplet (0.1mm) at a very low superheat level.

Similarly, the radiation heat transfer weight is also parametrically compared against the latent heat transfer rate under different operating conditions regarding jetting velocity and operating pressures (superheat level). First, Equation (5.6f) and Equation (5.6e) mathematically indicate that the radiation heat transfer rate is irrelevance with the droplet diameter. Therefore, a case of the droplet with identical size (1mm) and initial 100℃ is

parametrically studied to investigate the radiation heat transfer weight with different operating pressures and chamber temperatures, presented in Figures 5.10(a) and (b), respectively.

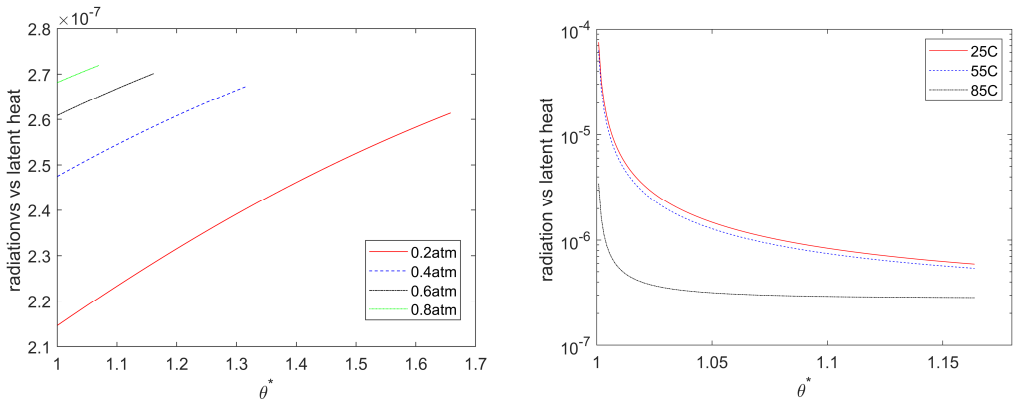

(a) effect of operating pressures (b) effect of chamber wall temperature

Figure 5.10 Heat transfer weight of radiation against latent heat.

In Figure 5.10(a), it assumes the chamber wall temperature under each operating pressure is the same as the saturated temperature of vapor. As operating pressure goes lower, the radiation heat transfer weight becomes smaller due to the increased intensity of evaporation. Moreover, with the increase in superheat ratio, the radiation heat transfer weight increases as well due to the enlarged temperature difference between the droplet surface and chamber wall. In Figure 5.10(b), all operating conditions remain the same except three different chamber temperatures are adopted as 25, 55, and 85℃, respectively. With the increase in superheat ratio, the radiation heat transfer weight decreases due to the evaporation becoming more intense. As expected, a lower chamber temperature will cause a higher radiation heat transfer weight due to the enlarged temperature difference between the droplet and chamber. However, we can see the gap between 85 to 55℃ is much larger than the gap between 55 to 25℃, that is because the radiation heat transfer rate is directly

proportional to the fourth power of temperature gradient. Overall, in all listed cases, both the heat transfer weights of convection and radiation are very small, which could be mathematically ignored for simplicity.

5.5 Conclusion

In this section, to improve the accuracy of lumped heat capacity model (LHCM) in predicting droplet flash evaporation, a modified LHCM has been proposed by adding a coefficient to the evaporation equation. The results indicate that the modified LHCM can effectively reduce the calculation error and still keeps the mathematical simplicity for applications of spray flash evaporation. Since the coefficient is determined based on the effective heat conduction model (EHCM), a dimensionless EHCM is also developed with newly-defined dimensionless parameters to deliver case-independent modification and parameterized criterion. As a result, the corrective coefficient is determined as a function of Fourier number. The coefficient value follows a positive correlation with Fourier number and is negatively related to the value of dimensionless parameters β^*, Bi, and E^*, which can also be given as empirical relations based on different Fourier numbers for specific applications.

Specifically, both EHCM and the modified LHCM are experimentally validated in terms of droplet temperature and meet good agreements. The results of LHCM are also plotted to show the improvement by the modified LHCM. In the case of maximum derivation between LHCM and EHCM (Figure 5.4), LHCM incorrectly predicts the flash cooling process five times faster than either modified LHCM or EHCM. On the other hand, the relative errors between the modified LHCM and EHCM range from 0%~3.4% in terms

of droplet instantaneous temperature under a wide operating range (droplet diameters from 0.01 to 1mm, superheat level from 1.06 to 1.67). Three dimensionless parameters (β^*, Bi, and E^*) are proposed in dimensionless EHCM to describe the heat transfer intensity of each item (latent heat, convection, radiation) during the flash cooling process. Larger values of these parameters reflect a more intense heat transfer outside the droplet and a more significant thermal non-uniform within the droplet, indicating a larger error by LHCM compared against EHCM. Parametric studies show either increasing the size or reducing the superheat ratio of the droplet will result in a larger corrective coefficient α_L in the modified LHCM. Such a coefficient follows a negative correlation with the three dimensionless parameters (majorly dominated by β^*) and a positive correlation with Fo. Meanwhile, the convection and radiation heat transfer weights during the droplet flash cooling process are also investigated compared against the latent heat transfer. The results indicate their heat transfer weights are very small, in which even the maximum value can barely achieve 0.1% in all studied cases. That means the convection and radiation could be safely ignored in most applications for the sake of modeling simplicity.

CHAPTER 6

CFD STUDY OF SPRAY FLASH DISTILLATION

Previous modeling study indicates an actively vacuumed spray flash will effectively generate a thermal non-equilibrium between yield vapor and spray residue within the evaporator. However, due to the non-uniformed distribution of vapor sources and velocities caused by spray polydispersion, as well as the thermal non-equilibrium of vapor exists in the full-field ambient all the time, the detailed energy/momentum interactions between vapor and droplets cannot be fully considered within the simplified process model. a full-scale computational fluid dynamics (CFD) study is desired to investigate such non-uniformity and thermal non-equilibrium of vapor. Therefore, in this chapter, a transient 3-D CFD case is studied for investigating the detailed processing characteristics of the continuous phase (vapor) during an actively vacuumed spray flash distillation.

Since the point-based droplet flash model proposed in last chapter is for pure water only. In this chapter, in order to simulate the spray flash distillation, first, the salinity effect is introduced into the point-based droplet flash model following the same methodology. Next, such a point-based droplet distillation model is compiled into ANSYS FLUENT via Discrete Phase Modeling (DPM) of User-Defined Functions (UDFs). The fully described interactions between the discrete phase (droplets) and the continuous phase(vapor) are also realized by UDFs. Finally, the CFD simulation is investigated with a typical case, and the numerical result is validated with experiments and compared with process modeling result. The CFD study demonstrated intense energy and momentum interactions between spray and vapor, due to the constantly existing thermal non-equilibrium and internal convection

of the vapor flow within the domain. The thermal non-equilibrium level between phases during a spray flash desalination not only depends on the spray's superheat level, but is also affected by the flowing condition within the evaporator. The results indicate CFD model has a better accuracy compared to the process model.

6.1 Introduction

For vacuum spray flash in a bounded environment with active vapor extraction, due to the non-uniformed distribution of vapor sources and velocities caused by spray polydispersion, as well as the thermal non-equilibrium of vapor exists in the full-field ambient all the time, a full-scale computational fluid dynamics (CFD) study is desired to investigate such non-uniformity and thermal non-equilibrium of vapor. Several CFD studies on spray flash have been reported based on different applications [87]–[89]. The spray flash evaporation in all these CFD studies is based on the lumped heat capacity method of the droplet, which is due to the simplified point-treatment of droplets in the discrete phase modeling. However, direct use of the lumped heat capacity model without a proper modification in evaporation rate formulation can be erroneous, especially for vacuum spray flash in which the evaporation intensity is very strong [22], [42], [64]. Nevertheless, introducing either the effective heat conduction or internal salt diffusion into droplet trajectory models in a Lagrangian-Eulerian CFD simulation requires a sub-grid description of temperature distributions within each droplet, which would dramatically increase the computational capacity requirement beyond practical reality. Therefore, based on the comparative study between the lumped heat capacity mothed and the effective heat conduction model for droplet flash in last chapter, a dimensionless corrective expression is proposed with salinity

effect in this study to modify the evaporation rate equation so that a modified lumped heat capacity model can be used into the Lagrangian-Eulerian modeling and its associated CFD simulation for spray flash distillation.

In this section, to study the detailed thermal non-equilibrium phenomena via CFD, several sub-tasks need to be achieved following the research logic: (1) development of a point-based droplet flash model used in discrete phase modeling of CFD, realized by introducing the salinity effect based on the modeling methodology of the point-based droplet flash model in Chapter 5; (2) perform a full-scale CFD simulation to study the phase coupling of non-uniformity and thermal non-equilibrium in vacuum spray flash and vapor transport inside the evaporation chamber; (3) the CFD results for a specific case is validated with experiments and compared with the process model.

6.2 Point-Based Droplet Flash Distillation Model (PBM)

For CFD simulation of spray flash desalination, the numerous droplets within the spray are usually simplified as non-physical points (such as discrete phase modeling) to reduce the computational cost [90]. Therefore, those point-based droplets can only be modeled by lumped heat capacity method (LHCM). However, the LHCM approximation in flash evaporation will constantly exceed the physical reality and overestimate the evaporation rate due to ignoring the internal heat transfer and salt diffusion [36], [64]. Since a CFD simulation is necessary for this study to investigate the complex non-uniformed vapor-droplet interactions, a point-based flash model of single salty droplet is proposed in this section via a modified LHCM approach to reduce the predicting error from the regular LHCM in CFD.

Similar to modeling of point-based droplet model, the over-estimation in evaporation rate from the LHCM in salty droplet flash distillation can be corrected by adding a coefficient on evaporating equation to modify the evaporation rate [106]. Such a coefficient is determined as the ratio of processing rates between LHCM and spatially dependent model (SDM). To realize that, a dimensionless SDM for the salty droplet flash from Chapter 4 is created to establish a case-independent correcting criterion.

According to the energy equation Equation(4.3) and its boundary conditions, the corresponding dimensionless forms can be expressed as below:

$$d^{*2}\frac{\partial\theta^*}{\partial Fo}=\frac{1}{r^{*2}}\frac{\partial}{\partial r^*}\left(r^{*2}\frac{\partial\theta^*}{\partial r^*}\right) \tag{6.1}$$

$$\theta_0^*=\frac{T_0}{T_\infty} \qquad \text{at Fo} = 0 \tag{6.1a}$$

$$\frac{\partial\theta^*}{\partial r^*}=0 \qquad \text{at } r^*=0 \tag{6.1b}$$

$$\frac{1}{d^*}\frac{\partial\theta^*}{\partial r^*}=\beta^*\left\{\frac{1-O^*\exp\left(\frac{L^*(1-\theta^*)}{\theta^*}\right)}{\sqrt{\theta^*}}\right\}+\text{Bi}\left(1-\theta^*\right) \text{ at } r^*=1 \tag{6.1c}$$

Where the dimensionless superheat ratio, radius ratio, Fourier number, and the reduced diameter are respectively defined by:

$$\theta^*\equiv\frac{T_d}{T_\infty} \quad r^*\equiv\frac{2r}{d_d} \quad \text{Fo}\equiv\frac{4k_{eff}t}{\rho_d c_d d_0^2} \quad d^*\equiv\frac{d_d}{d_0} \tag{6.1d}$$

It is noted that β*, O*, L* and Bi are all dimensionless parameters, which stand for, flash evaporation, the coefficient of effective vapor pressure, latent heat as well as the effective Biot number of heat convection, respectively:

$$\beta^* \equiv \frac{L_{fg}\alpha d_0 P_\infty}{2k_{eff}}\sqrt{\frac{M_v}{2\pi R_u T_\infty^3}} \qquad O^* \equiv 1\Big/\left(1+\frac{MW_w}{MW_s}\left(\frac{C_s}{1-C_s}\right)\right) \qquad L^* \equiv \frac{h_{fg}M_v}{R_u T_\infty} \qquad \mathrm{Bi} \equiv \frac{h_m d_0}{2k_{eff}} \tag{6.1e}$$

The dimensionless coefficient O* is time-dependent with the molar concentration of the non-volatile substance (NaCl), which will be determined by the diffusion equation. Therefore, the corresponding dimensionless forms of the diffusion Equation (4.4) and its boundary conditions can be further expressed as:

$$d^{*2}D^*\frac{\partial c^*}{\partial Fo} = \frac{1}{r^{*2}}\frac{\partial}{\partial r^*}\left(r^{*2}\frac{\partial c^*}{\partial r^*}\right) \tag{6.2}$$

$$c_0^* = 1 \qquad \text{at} \quad D^* = 0 \tag{6.2a}$$

$$\frac{\partial c^*}{\partial r^*} = 0 \qquad \text{at} \quad r^* = 0 \tag{6.2b}$$

$$d^*\frac{dc^*}{dr^*} = \beta^* c^* \frac{O^*\exp\left(L\left(1-\frac{1}{\theta^*}\right)\right)-1}{Y\sqrt{\theta^*}} \qquad \text{at} \quad r^* = 1 \tag{6.2c}$$

Where the dimensionless molar concentration of the non-volatile substance, the dimensionless diffusion coefficient, and the additional multiplier are respectively defined by:

$$c^* \equiv \frac{c}{c_0} \qquad D^* \equiv \frac{k_{eff}}{D\rho_l c_l} \qquad Y = 2\pi d_0 D h_{fg}\rho_d \tag{6.2d}$$

Where c_0 is the initial molar concentration of the non-volatile substance.

In addition, the reduced diameter, d^* is also time-dependent with evaporation, which is given by the mass conservation equation, Equation (4.8). Substituting Equation (4.7) and Equation (4.9) into Equation (4.8), then transforming to the dimensionless format, it yields:

$$\frac{dd^*}{d\mathrm{Fo}} = \mathrm{Ja}\beta^* \left(1 - O^* \exp\left(L\left(1 - \frac{1}{\theta}\right)\right)\right) \Big/ \sqrt{\theta^*} \tag{6.3}$$

where *Ja* is the Jakob number, defined by:

$$\mathrm{Ja} \equiv \frac{c_l T_\infty}{h_{fg}} \tag{6.3a}$$

Next, to compare the computational difference in processing rate between LHCM and SDM, a dimensionless parameter, the evaporation residue m_d* can be defined to evaluate the evaporation completeness as:

$$m_d^* \equiv \frac{m_d - m_{d,\infty}}{m_{d,0} - m_{d,\infty}} \tag{6.4}$$

Where $m_{d,0}$ and $m_{d,\infty}$ represent the initial and the equilibrium droplet mass, respectively.

Further, we found the evaporation residue m_d* in both models decreases in a nearly exponential trend (or linearly in the semi-log scales) along with the characteristic time Fo. Figure 6.1 exemplarily presented such a tendency in a typical case of β*=78.8, *Bi**=0.0069, and *D**= 296.9 (1mm diameter droplet with the initial salinity of 3.5% and the initial temperature of 100℃ under 0.6 atm operating pressure). In Fig. 4, LHCM (red data) shows a much steeper curve, representing a much faster flash rate than the SDM. Since the most predicting error from LHCM is obtained at the earlier stage of the flash, due to a much higher processing intensity, so rather than correcting the entire process, we focus on the earlier moment for simplicity. Therefore, a cut-off value (0.01 in this case marked as the dash line in Figure 6.1) is applied regarding the evaporation residue to define a comparison range between the two models, which indicates the modeling correction is considered until

the evaporation completeness of the flash process achieves 99%. As demonstrated, results of both models can be approximately fitted in a linear relationship between the evaporation residue m_d* and the Fo number under semi-log scale, which further suggests a relationship within the effective range:

$$m_d^* = \exp\left(-\lambda \mathrm{Fo}\right) \tag{6.5}$$

Where λ is the slope in the linear curve fitting in the semi-log scales.

Finally, a corrective coefficient on the droplet evaporation rate can be defined as the ratio of evaporation rates between SDM and LHCM:

$$\frac{\dot{m}_{v,S}}{\dot{m}_{v,L}} = \frac{\left(\frac{dm_d}{dt}\right)_S}{\left(\frac{dm_d}{dt}\right)_L} = \frac{dm_{d,S}^*}{dm_{d,L}^*} = \frac{\lambda_S}{\lambda_L}\exp\left(\left(\lambda_L - \lambda_S\right)\mathrm{Fo}\right) \equiv \alpha_L \tag{6.6}$$

where the subscripts S and L stand for SDM and LHCM, respectively. In other words, the evaporation rate predicted by LHCM could close to the results of SDM by adding this corrective coefficient on the evaporating equation (Equation (4.2)). Moreover, according to Equation (6.6), such coefficient for a spray with determined physical properties evaporated under the same operating condition (λ_S and λ_L are constants) is only depends on characteristic time (Fourier number).

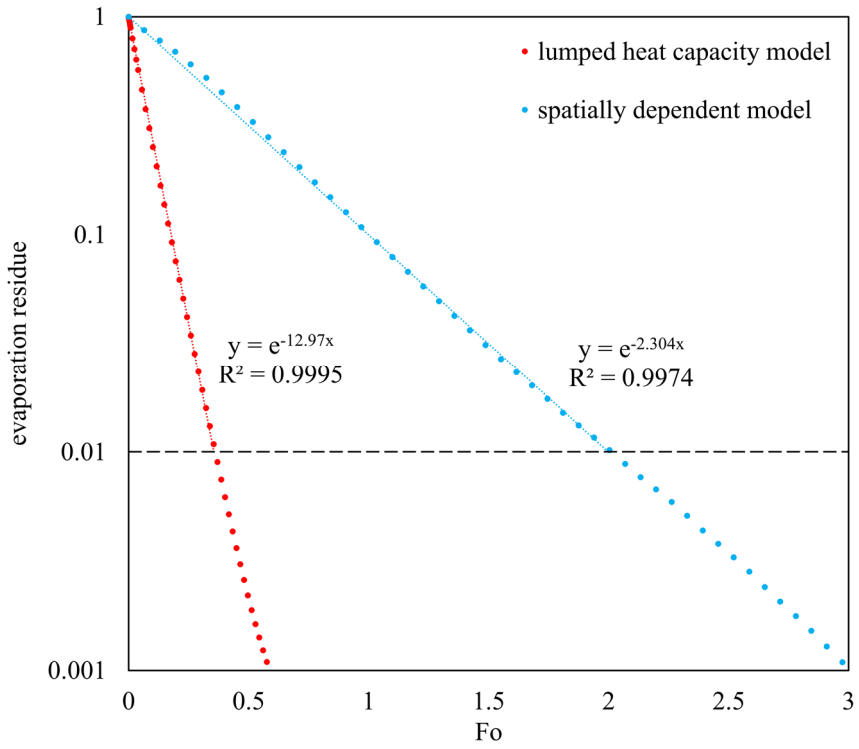

Figure 6.1 An exemplified comparison of Evaporation residue vs. Fo via two models.

Therefore the evaporating equation for the modified LHCM can be expressed as:

$$\dot{m}_v = \alpha_L \alpha \pi d_d^{\,2} \sqrt{\frac{M_v}{2\pi R_u T_d}} \left(P_{sat} - P_0\right) \tag{6.7}$$

Since both spatial distribution effects of internal temperature and salinity on evaporation rate have now been considered in the corrective coefficient α_L, the energy and salinity equations can be expressed by ordinary differential equations (ODEs) from the regular LHCM model:

$$\frac{d\left(m_d c_d T_d\right)}{dt} = -h_{fg}\dot{m}_v + h_m \frac{\pi}{4} d_d^2 (T_v - T_d) \tag{6.8}$$

$$\frac{dC_s}{dt} = \frac{C_s \dot{m}_v}{m_d} \tag{6.9}$$

Where equations (6.8) and (6.9) adopt volume-averaged properties for the internal temperature and salinity. These spatially uniformed approximations will simplify the modeling by eliminating the requirement of partial differential equations (PDEs) groups of equations (4.3-4.3d) and equations (4.4-4.4c) and erasing one variable of the molar concentration of the non-volatile fraction (Equation (4.5)) from Chapter 4.

Finally, by replacing Equation (4.1), Equation (4.2), and Equation (4.4) with Equation (6.8), Equation (6.7), and Equation (6.9), the point-based droplet flash model (PDM) realized by the modified LHCM is built by Equation (4.6)-Equation (4.9), Equation (6.8), Equation (6.7), Equation (4.3), and Equation (6.9), with eight unknowns (u_d, ρ_m, d_d, m_d, T_d, m_v, $P_{sat,v}$, and C_s).

6.3 Case Study of ANSYS FLUENT

In this CFD simulation of spray flash distillation, the droplets flash is modeled by PBM via the Discrete Phase Modeling (DPM) for involving the polarization effect, which is further coupled with the turbulent model for the continuous phase (vapor flow) and solved in ANSYS FLUENT. Since the default DPM of FLUENT cannot predict a self-heat supplied droplet flash process [90], the interactions of momentum/energy transports between phases modeled in Chapter 3 [3] and the flash evaporation for droplets modeled by PBM are compiled by User-Defined Functions (UDFs).

The geometric structure of the evaporator in CFD is shown in Figure 6.2, following its dimension in the real experimental system. The geometric parameters are summarized in Table 6.1. Four assumptions are further adopted in the simulation to simplify the process and reduce the computational cost. First, once the droplets reach the chamber wall or their

temperatures are sufficiently close to the saturated temperature, they will be assumed as being immediately escaped from the chamber. Second, the discharge port of brine is treated as one part of the "wall" for the continuous phase since there is always filled with saturated solution during the process and the vapor cannot escape through. Third, since all droplets are treated as points in DPM, it is assumed there is no volumetric effect of droplets on vapor flow nor volumetric accumulation of water residue. Last, all chamber walls are assumed as perfectly thermally insulated.

Table 6.1 Key Geometric and Operational Parameters

Parametric	Value	Unit
Spray nozzle	Full-cone	-
Spray angle	57	°
Droplets size distribution	Rosin-Rammler distribution: κ=4.413 and δ=1.097	-
Nozzle location	Top center	-
Spray injection velocity	3.3	m/s
Spray liquid	Salty water	-
Initial salinity	0% ~ 10%	-
Spray flow rate	45.0	ml/s
Chamber height	0.5	m
Chamber diameter	0.3	m
Vapor outlet diameter	0.75 (19.05)	Inch (mm)
Liquid outlet diameter	0.5 (12.7)	Inch (mm)
Spray initial temperature	70 - 100	°C
Chamber vacuum pressure	0.25 - 0.8	atm
Chamber material	Stainless steel with insulation	N/A
Thermal resistance of chamber	2.16	$K \cdot m^2/W$

Figure 6.2 Geometric structure in CFD simulation.

A typical spray flash desalination case of the specific salty water (3.5% NaCl solution) with 367K (93.85°C) initial temperature under 40kPa operating pressure is simulated by the CFD. The droplet size distribution and the average velocity of the spray are determined via a laser-scanning aided optical measurement [3], and the specific values are listed in Table 6.1. According to the determined droplets size distribution of the spray, the spray injection consists of seven groups of different sizes of droplets in each parcel or spray trajectories (that is N=7 in equations 22 and 23). The simulation is solved with a transient approach, in which the computation is terminated when all monitored critical variables (such as domain temperature contour, velocities, total evaporation rate, outlet temperatures of two phases) become time-insensitive (after about 300 seconds in this case). Re-Normalized Group (RNG) k-ε model [90] is adopted as the turbulence model, which is widely reported as one of the best applicable turbulence models for in-chamber flow

simulation with a spray [87], [89], [107]. The detailed information of the setup is summarized in Table 6.2.

Table 6.2 Setup Details of CFD Simulation

Solver description	
Steady/unsteady	Transient/unsteady particle tracking
Dimension	3-D
Turbulence model	Re-Normalized Group (RNG) k-ε model
Discrete phase model	Droplets with UDF evaporating laws and coupled heat-mass solution; interacted with continuous phase
Injection	solid cone; spray angel 57°; spray velocity 3.23m/s; Rosin-Rammler size distribution: κ=4.432 and δ=1.099
Boundary conditions	
Spray inlet	Mass flow inlet (zero-in); DPM inlet
Steam outlet	Pressure outlet; DPM escape
Water outlet	Mass flow outlet (zero-out); DPM escape
wall	No heat flux; DPM escape

The mesh sensitivity analysis was conducted on three different mesh densities to ensure the results are independent of the grid, corresponding to the total cell number are 0.28 million, 0.58 million, and 1.33 million, respectively. A ten-seconds operating was simulated for these mesh models and it was found the results will not change significantly between 0.58 million and 1.33 million with the value differences range from 0.14% to 1.2% for curial parameters such as average outlet temperature of two phases, the average temperature of full-field vapor phase, and overall evaporation rate of droplets between 0.58 to 1.33 million. To reduce the computational cost, the 0.58 million-case is adopted for the simulation.

6.4 Result Discussion

The constant parameters (λ_S and λ_L) used for correcting the evaporation rate (determining the α_L) in PBM are calculated and listed in Table 6.3 for the seven re-grouped droplet sizes according to the specific droplet size distribution in Table 6.1. The predicting error margin of PBM in the evaporation rate is within 6% by comparing with SDM in all cases of different sizes. According to the table, the PBM method can significantly improve the accuracy (by up to 700% under the category of the largest droplet) in terms of the transient evaporation rate compared against the regular LHCM.

Table 6.3 The Corrective Parameters of Droplets with Different Size

Droplet diameter	0.4mm	0.6mm	0.8mm	1.0mm	1.2mm	1.4mm	1.6mm
λ_S	-1.678	-1.977	-2.109	-2.124	-2.330	-2.361	-2.379
λ_L	-4.082	-6.163	-8.335	-10.826	-12.440	-14.510	-16.720

In Figure 6.3, temperature profiles of droplets and vapor in this example case are plotted along the axial direction of the evaporation chamber. To focus on the spray flashing moment, the “travel distance” representing axial distance starts from the spray nozzle and is cut-off at 0.3m in the figure. In the CFD, the droplets with Sauter Mean Diameter (0.33mm) that drop along the vertical central path are sampled and plotted as blue solid-line and black dash-line, corresponding to two different initial salinity 3.5% and 0%, respectively. The case of 3.5% salinity is also validated with the experimental results as well as compared with the process model (green dot-line). We can see the result of CFD meets the best agreement with experiments at the front section (within 0.1m) of the travel distance where the flash evaporation is most intense. Meanwhile, the decrease of droplet

temperature in CFD is noticeably slower than the process model. It is most likely because the spray flash process in CFD considered more detailed energy/momentum interactions between droplets and vapor. Also, the terminal temperature of the experiment is lower than CFD, which is likely caused by the inevitable heat dissipation of the chamber in reality.

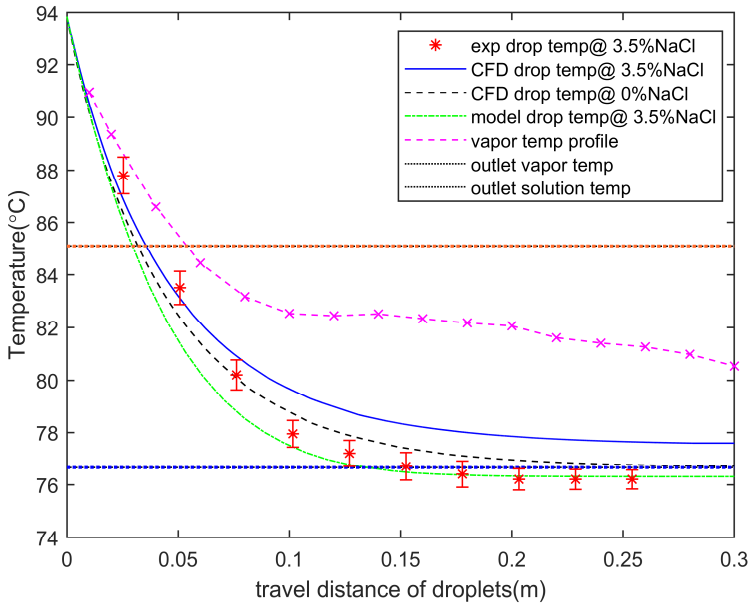

Figure 6.3 Comparison of droplets temperature along with the vertical travel distance.

Moreover, the vapor temperature profile from CFD is also plotted in Figure 6.3. Such values are determined by averaging the vapor temperatures of cross-sections along the axial direction within the chamber, like shown in Figure 6.5(b). Agreed with the previous section, it also predicted a noticeable temperature gap between droplets and vapor. More interesting, since now the vapor non-uniformity is considered via fully defined 3-D Eulerian modeling, we can see the temperature curve drops along the axial direction with a quite fluctuation, which indicates internal convections exist in the gaseous phase. Such an effect will make the processing thermal non-equilibrium between phases becomes more complicated to predict. In addition, the average temperatures at the vapor outlet and spray

residue outlet calculated from CFD are also plotted in Figure 6.3 as referential lines. Although the vapor outlet is at the top of the chamber, we can see the average outlet temperature (85.1°C) is lower than the average temperature near the chamber top (about 91°C). This difference also indicates vapor with different temperatures gets mixed before being extracted out of the chamber. Related details of this part will be further discussed in the following.

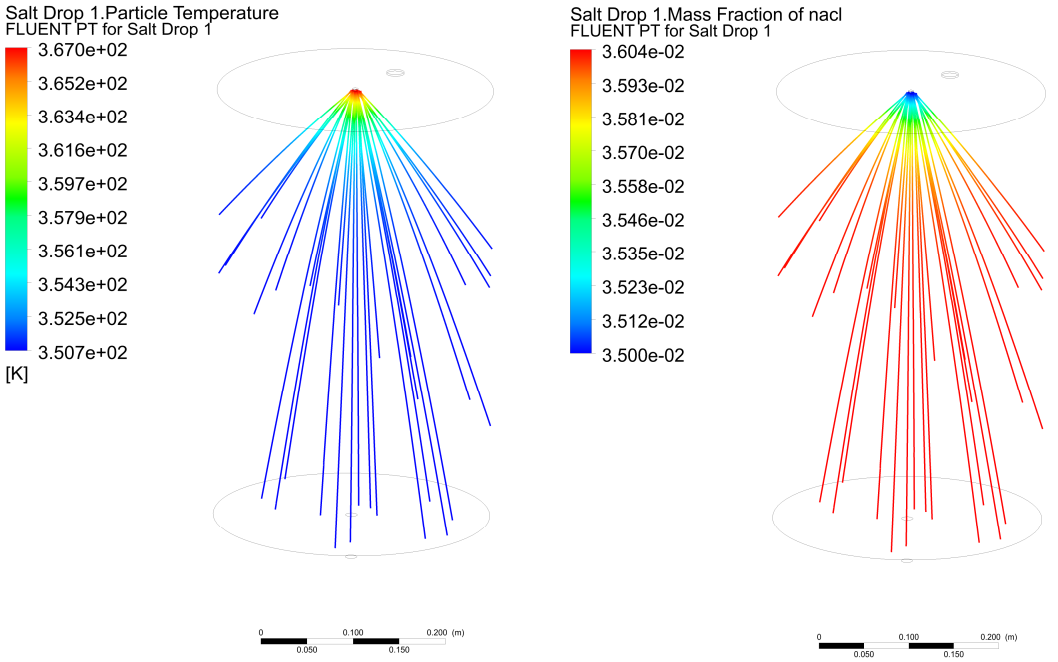

(a) (b)

Figure 6.4 Droplets trajectories of its temperature (a) NaCl mass fraction (b).

Figure 6.4(a) illustrates the spray flash pattern with temperature changes along the droplet trajectories, in which droplets with the Sauter mean diameter are sampled for presenting here. In this size, all droplets are sufficiently cooled down to the saturated temperature of 350 K or 77°C during the traveling. Figure 6.4(b) presents the salinity change of the same droplets along their trajectories. Figures 6.4(a) and 6.4(b) both indicate

the spray flash desalination is a very fast process, with most evaporation completed within the top half of the chamber. Such a process can be very volumetric efficient.

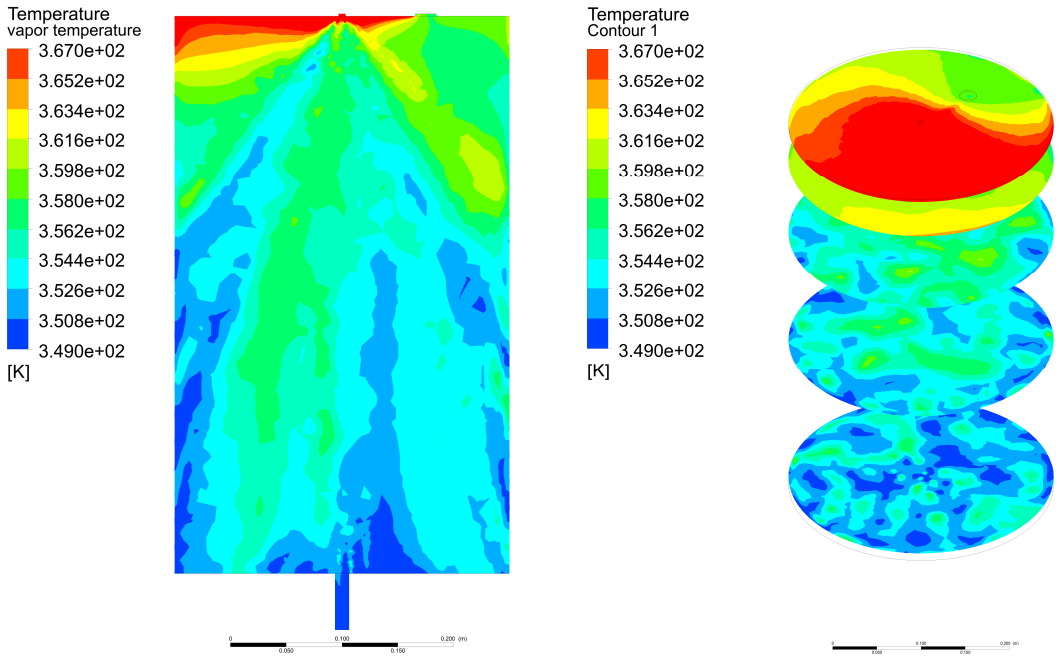

(a) (b)

Figure 6.5 the contours of vapor temperature on the median plane (a) and various cross-sections (b).

Figures 6.5(a) and (b) present the temperature contour of vapor on the median plane and multiple cross-sections within the chamber to demonstrate the thermal non-uniformity during the process. In Figure 6.5(b), the cross-sections are defined based on different axial distances starting from the spray nozzle: 0.01m, 0.05m, 0.15m, 0.3m, and 0.49m (the total height of the chamber is 0.5m). Meanwhile, Figure 6.6(a) shows the vapor source from spray evaporation to the gaseous phase in the median plane of the chamber. We can see vapor was continuously generated from the injecting spray. The hottest vapor is produced and accumulated around the top zone of the chamber, and the fresh vapor from downstream becomes cooler and cooler until evaporation vanishes. Around the vapor outlet, hotter

vapor and cooler vapor get mixed and then extracted out of the chamber. This phenomenon is also indicated by the vapor temperature profile in Figure 6.3. Due to the asymmetrical arrangement of the vapor outlet (located on the right side in figures), we can see the hot vapor accumulates on the left side before escaping out of the chamber, which further indicates such a thermal non-uniformity of the vapor is not only depended on the flash process, but also affected by specific flow conditions from the operation.

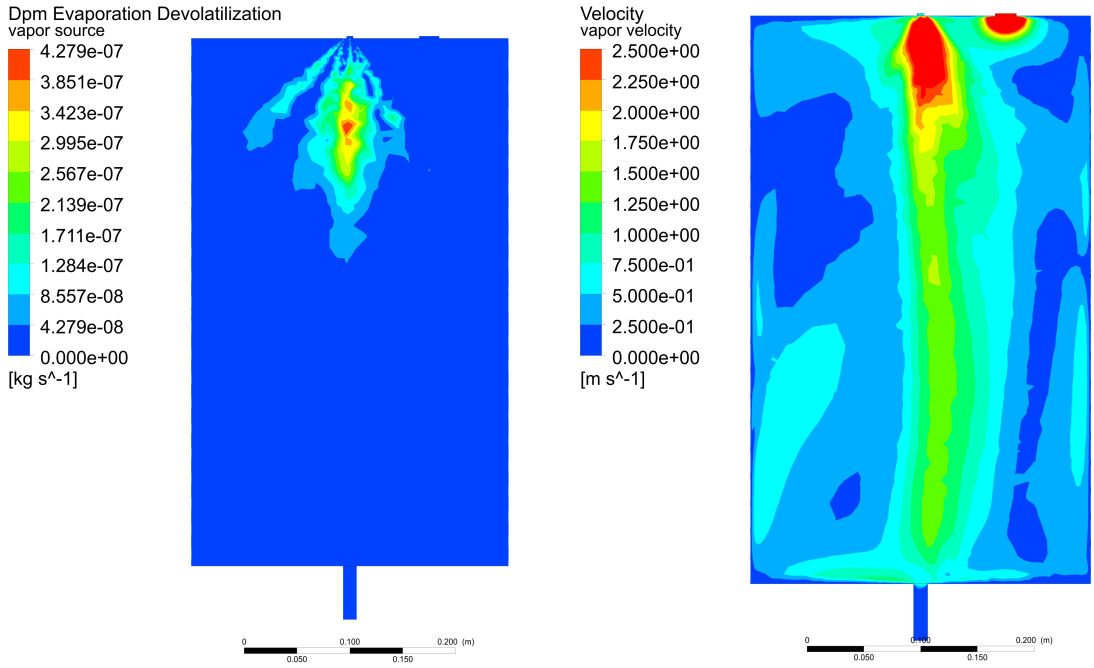

(a) (b)

Figure 6.6 The contours of vapor source on the median plane (a) and vapor velocity magnitude (b).

Figure 6.6(b) shows the velocity contour of the vapor in the median plane. The velocity scale in this figure is limited by 2.5 m/s to present better details of the velocity distribution in most weak-flowing areas. The strong-flowing jetting and sucking areas are colored red, indicating the velocities there could go much higher than 2.5m/s. The result indicates that due to the droplets' downward movement, the generated vapor will also

obtain an initial downward velocity before moving upwards by the vacuum extraction. Such downward initial velocities will also enhance the internal convection of vapor flow.

Finally, the CFD and process model predicted overall evaporation rate and the average outlet temperatures of vapor and spray residue, are validated with experiments and summarized in Table 6.4. We can see CFD provided a better agreement with experiments in this case. The process model over-estimated both evaporation rate and the thermal non-equilibrium by a little bit, which may be caused by the simplified approximation of 1-D Eulerian modeling for vapor flow. However, such relative errors are still acceptable (less than 10%) considering the benefit of significantly reduced computational cost.

Table 6.4 Experimental Validation of Overall Thermal Characteristics

	CFD	Process model	experiment
Evaporation rate	4.13 kg/h	4.46 kg/h	4.05kg/h
Outlet temperature of the vapor	85.1℃	85.4℃	84.5℃
Outlet temperature of the water	76.7℃	76.3℃	75.5℃

6.5 Conclusions

This chapter presented a three-dimensional CFD study of simulating spray flash desalination in an isolated evaporator with active vapor extraction. A point-based droplet flash distillation model is proposed with two-way coupling between discrete phase and continuous gaseous phase by the Lagrangian-Eulerian modeling. The modeling equations are complied and solved via FLUENT DPM and its associated UDFs. A typical desalination process within a cylindrical evaporator has been simulated under vacuuming at 40kPa operating pressure with a single full-cone spray at an inlet temperature of 367K

and NaCl mass fraction of 3.5%. The spray is polydispersed and follows the Rosin-Rammler size distribution.

Both simulations and experiments suggest the spray flash desalination process happens very fast, that most droplets achieve near-equilibrium status very shortly. Two simulation results with different salinity of the spray suggest the salt fraction brings negative impacts on evaporating efficiency and evaporating rate. The CFD study demonstrated intense energy and momentum interactions between spray and vapor, due to the constantly existing thermal non-equilibrium and internal convection of the vapor flow within the domain. The thermal non-equilibrium level between phases during a spray flash desalination not only depends on the spray's superheat level, but is also affected by the flowing condition within the evaporator. The motion of droplets and vacuuming will also promote the vapor convection within the chamber, which could result in reducing the thermal non-equilibrium level of full-field. The CFD model has a little bit better accuracy compared to the process model. The latter over-estimated the evaporation rate and the temperature gap between outlet vapor and spray residue by 10% against experiments in a specific case, which may be caused by the simplified 1-D vapor flow during the modeling. However, the CFD simulation shows that there exist local regions of strong non-uniformity in vapor temperature and velocity, which may be of importance to the practical design of the evaporation system.

CHAPTER 7

TWO-STAGE LAB-SCALE PROTOTYPE

Based on previous understanding of the fundamental processing mechanisms within our technology, in this chapter a two-stage lab-scale prototype of our distillation technology is built accompanied with systematic thermodynamic modeling for testifying the design concept, model validation, as well as evaluating the overall thermal performance.

7.1 Detailed Two-Stage System Design

Our lab-scale two-stage spray flash distillation system is built to achieve the following advantages or functions.

1. multi-stage with heat recovery feature

   The two-stage system is the most basic multi-stagger stage system of our technology that contains one inter-stage heat recovery, in which the heat of the second stage is supplied through the heat recovery from the first stage. Therefore this system can be used to prove and evaluate the important heat recovery solution in our technology on a real lab-scale platform.

2. Active vacuum extraction

   In this system, both two stages are parallelly arranged and connected with the same vacuum source in order to achieve a better flash efficiency. The operating pressure of each evaporator can be independently controlled via a pressure regulator installed before the final condenser.

3. Steam powered

The only external heat input of the system is team, in order to realize and testify the concept that our technology can be driven by low-grade heat only.

4. Steady-state operating condition

The system is able to work with a steady-state operation, in which feed supplement, yield water extraction, and vacuum sucking can be continuously realized during the process.

5. Mobility (compact size and limited weight)

The new system is able to work with a mobile gas-powered heating source or even other kinds of locally heating source. Meanwhile, the weight and size of all equipment are controlled under a certain range to make sure the entire system can be loaded on a truck.

6. Easy replacement of main components for studying with different conditions

The system is adopted by module design, such as nozzle, condenser, and evaporation chamber, to make sure major parts could be easily changed for different applications or experimental studies.

7. Data acquisition

Main processing characteristics are measured transiently via a data acquisition system during the process, such as temperature, pressure, and volumetric flow rate.

7.1.1 The overall Two-Stage System Design

In this section, the overall two-stage system design is schematically presented in Figure 7.1, accompanied by a 3-D view in Figure 7.2.

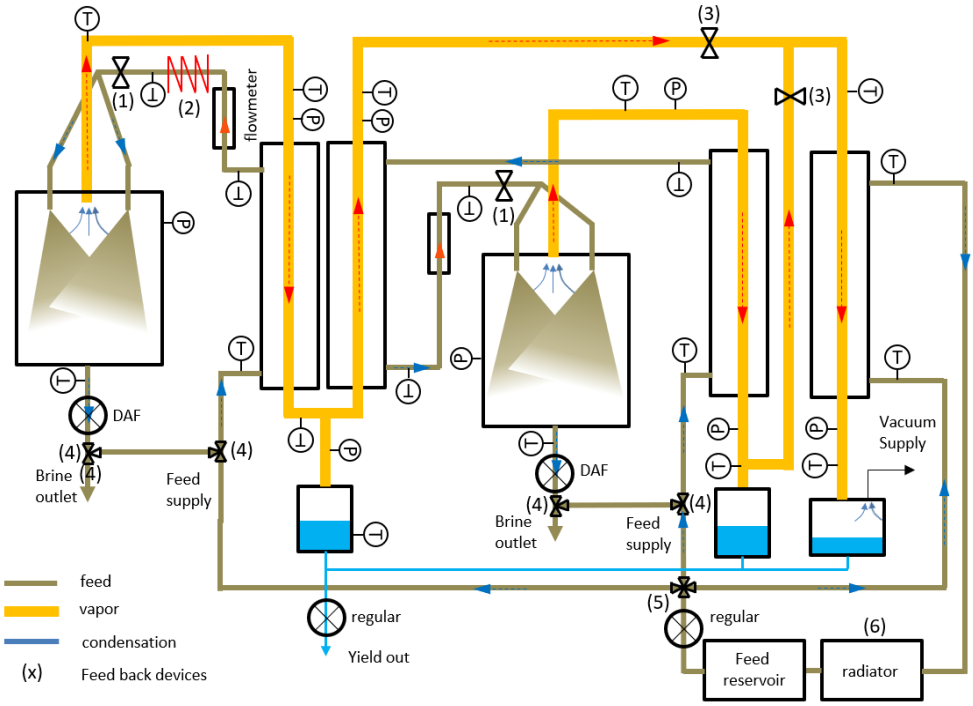

Figure 7.1 Schematic diagram of two-stage distillation system.

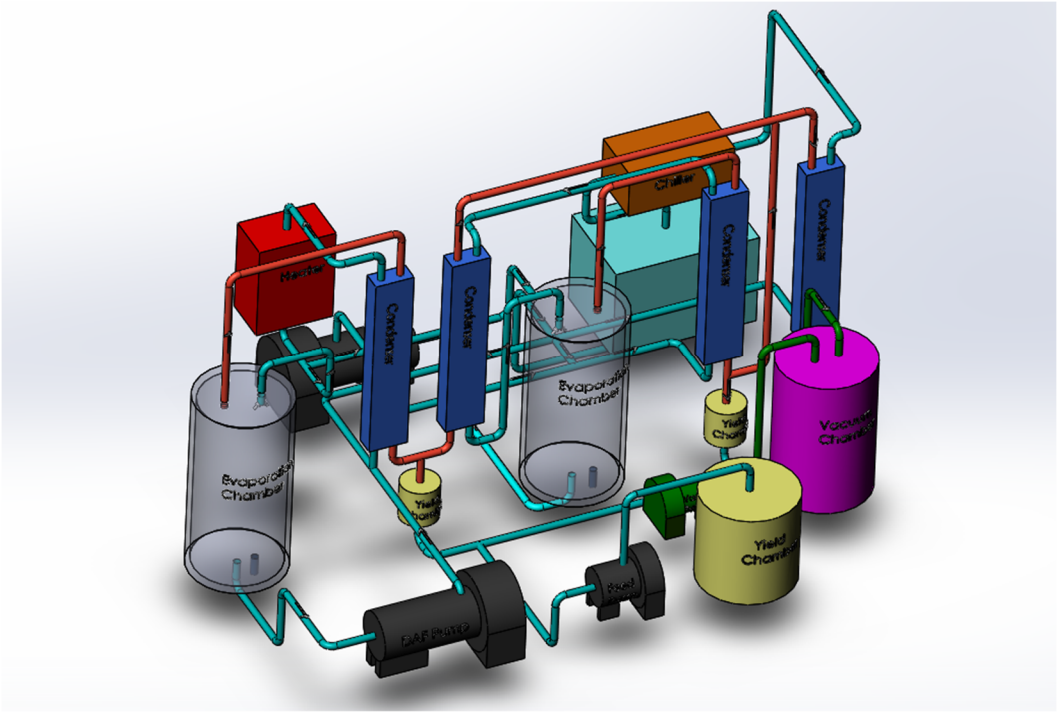

Figure 7.2 Three-D view of the two-stage distillation system.

As we can see, the system comes with one external heat, two evaporators, three yield chambers, and four condensers. The orange path represents the vapor path, and the brown path is the liquid (brine) path. In the last stage, the vapor cooling is realized by the pre-heat of the brine from the brine reservoir, in which a radiator is also arranged for further heat dissipation in case the brine is over-heat. Two dissolved air flotation (DAF) pumps are used for the brine circulation of each stage to avoid the vapor lock due to the pre-cavitation effect in certain low-pressure zone within the pump. In addition, two regular pumps are used for yield extraction and feed supply, respectively. The number-marked switches in Figure 7.1 are either valves in brine paths or the pressure regulators in vapor paths, respectively. In this way, both the brine flow rate and evaporating pressure can be independently controlled during the process.

7.1.2 The Real System

The real system built in the lab is exhibited in Figure 7.3. The system is heated by steam, which is generated from an electric steam generator due to safety concerns. The vacuum source is realized by a regular vacuum pump with a 30 Gallon vacuum reservoir. The entire system is thermally insulated to pursue a better measurement for thermal performance analysis. This system can be contentiously operated under a stead-state. Curial processing parameters are monitored during the operation, which are clarified later in Figure 7.10. The detailed bill of materials is summarized in Table 7.1

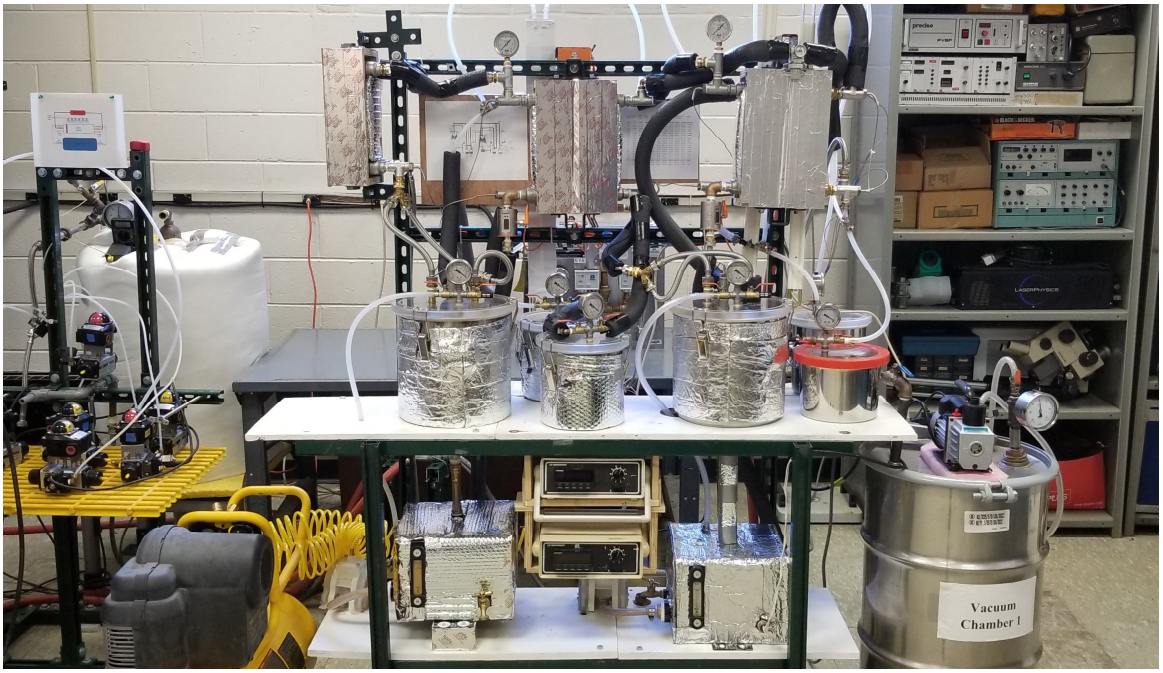

Figure 7.3 The lab-scale two-stage experimental system.

Table 7.1 Bill of Materials of the Two-Stage Experimental System

Items	Quantity	Notes
steam generator	1	power: 7kw
evaporator	2	size: 5 gallons
nozzle	2	model: BETE WL6
condenser	4	capacity: 3.1kbtu/h@5gpm
cyclic brine pump	2	DAF pump
yield chamber	4	size: 2 gallons
brine reservoir	2	size: 5 gallons
vacuum pump	1	power: 0.5kw
vacuum reservoir	1	30 gallons

7.2 Systematic Modeling of the Two-Stage Prototype

In this section, the systematic model of the two-stage experimental system is proposed, which is realized section by section following the computational logic. The overall schematic diagram of the system modeling is presented in Figure 7.4. Firstly, the named naming rulers of systematic nomenclatures are explained as follows.

The pressure term is P, T is temperature, m is mass flow rate, and q is heat transfer rate. In the subscript, all items begin with Arabic numerals to represent the number of stages. For example, 1 is the first stage. In addition, L means the last stage. The second symbol represents the kind of working media, f means liquid feed, and v means vapor. The rest symbols begin after a comma to represent the information of properties, functions, and locations. We have two condensers in each stage, one for the internal heat recovery is named as a, the other one for the external heat recovery is named as b. For example, $T_{1v,ao}$, means the temperature of, stage-1, vapor, condenser 1, outlet. $\Delta P_{1f,h}$ means pressure drop of, stage-1, feed, nozzle. For those commonly shared properties, such as the temperature of feed supply, its name is simplified as T_f.

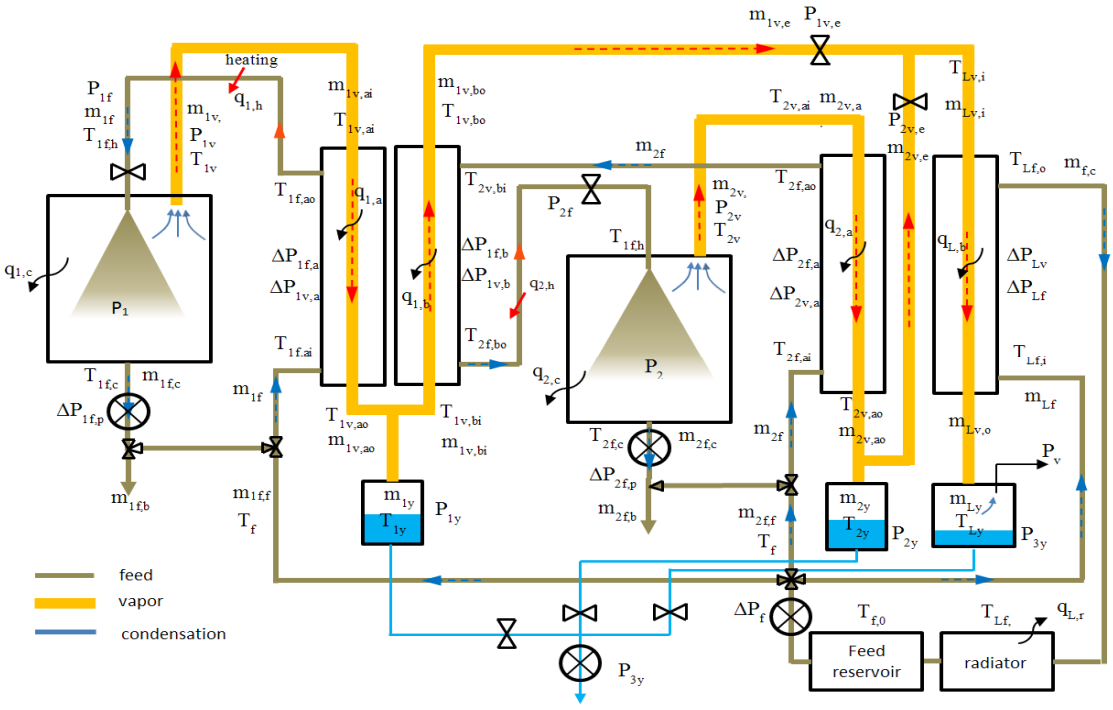

Figure 7.4 Schematic diagram of systematic modeling with key parameters.

7.2.1 Summary of Assumptions

The modeling assumptions are summarized in this section as below.

1. Assume the vacuum level is uniform in each chamber.

2. Assume droplets are spherical within the chamber.

3. Assume only mass heat transfer is considered for droplets' evaporation.

4. Assume the effects of NCG on spray evaporation and vapor condensation are negligible.

5. Assume all pipes are insulated.

6. Assume all condensers are insulated.

7. Assume the helical effect added on the pressure drop within the condenser is negligible.

8. Assume the pressure drop for pipes is negligible.

7.2.2 Modeling by Sections

The overall modeling of multi-stage distillation system consists of four sub-models, the evaporation model, the mixing and condensation model, the last stage model, and the yield model. To intuitively present the calculation domains for each section, the sections within the system is marked by different colors and symbolically exhibited in Figure 7.5, which is separated by six sections following the calculation sequence: (1) the evaporation section of stage-1, (2) the mixing and condensation section of stage-1, (3) the evaporation section of stage-2, (4) the mixing and condensation section of stage-2, (5) the last stage section, (6) the discharge section, and (7) the yield section.

As Figure 7.5 shows, the red color represents the evaporation section of each stage, respectively. The blue part means the brine circulation and the vapor condensation of the first stage, in which the internal heat recovery between the vapor and brine of the first stage

happens within the first condenser (named as internal condenser). The green parts are the mixing and condensation sections for brine and vapor in the second stage, respectively. The evaporation, mixing, and condensation processes of stage-2 follow the same mechanism models as in stage-1. The brine will recover the heat from vapor by the internal condenser (right) firstly, then will be further heated by recovering the heat from the vapor of the first stage within the external condenser (left). It needs to note, this external condenser is also acting as the external heat input for the second stage to drive the flash evaporation process. On the modeling side, the inlet feed temperature of the evaporator in stage-2 is coupled with the outlet brine temperature of the external condensor. Instead, there is no external condenser in the second stage. After both two condensers of the second stage, all vapor will be directly connected to the last stage (purple) after the internal condenser. The vapor residue from both evaporators will be finally fully condensed there, and any non-condensable gas (NGC) will be extracted out by a vacuum source. In this figure, the last condenser (purple) is cooled by the feed from reservoir with a radiator for heat dissipation. Of course, it can also be cooled by an open-flow coolant depending on the applicating condition. The brown path is for discharging the brine, and the yellow path is for collecting the yield water from vapor condensation.

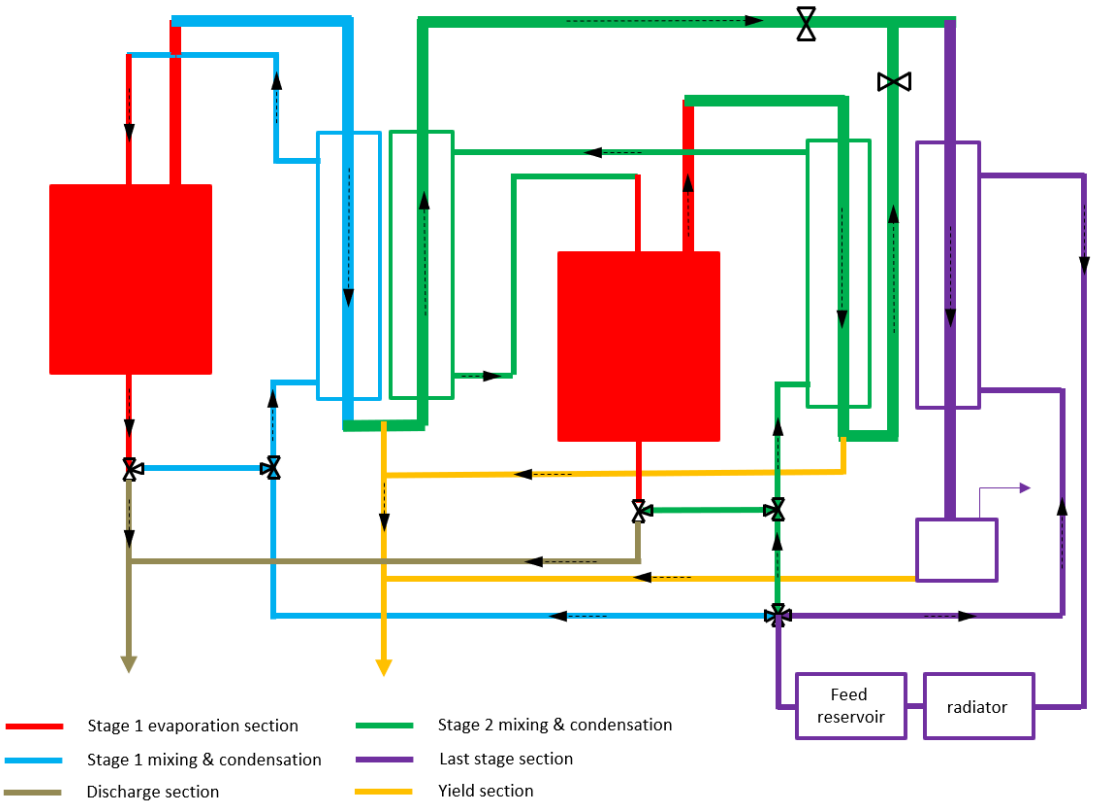

Figure 7.5 A symbolic diagram of the system by sections.

7.2.3 Modeling of Stage-1 Evaporation

Consider the first evaporator, evaporator 1, as the initial step of the entire modeling. Recall from Chapter 3 and Chapter 4. The evaporation process can be modeled either by our proposed SDM model or PBM model with 1-D Eulerian vapor flow. In order to achieve a better computational performance, the PBM model is adopted in this case. For the detailed modeling of spray flash distillation with active vapor extraction, please refer to Chapter 4. The schematic diagram of modeling the stage-1 evaporation section is presented in Figure 7.6.

However, for the systematic modeling, the heat dissipation from the chamber must be further considered in our real system based on the previous process model, which can be expressed below.

$$q_{\text{loss}}(x) = \frac{T_v(x) - T_\infty}{1/h_c(x)2\pi r_{c,i} + \ln(r_{c,o}/r_{c,i})/2\pi k_c + 1/h_\infty 2\pi r_{c,o}} \tag{7.1}$$

It assumes heat dissipation caused by the thermal radiation can be ignored that only the convective heat transfer is accounted. The dissipated heat is assumed to be provided by the fresh vapor/droplets only (no feed reservoir within the chamber), T_v is the temperature of vapor, h_c is heat convection rate of chamber, and both have different values locally. The subscript *i* means inner radius of the chamber, and *o* means outer radius.

As a result, the updated energy equation becomes:

$$\frac{d(\rho_v c_{pv} u_v T_v)}{dx} = \sum_{i=1}^{N}\left(n_d(i)\left[\dot{m}_v(i) c_{pv} T_d(i) + h(i)\frac{\pi}{4} d_d^2(i)(T_d(i) - T_v) - \dot{q}_{loss}(i) \right]\right) \tag{7.2}$$

In addition, to determine the fresh vapor properties from chamber outlet, a series of parameters can be obtained based on the solution of above model. One of the most important processing charaterstic is the average temerpature of the outlet vapor, which can be determined as:

$$\overline{T}_v = \frac{\int_0^H \dot{m}_v T_d dx}{\int_0^H \dot{m}_v dx} \tag{7.3}$$

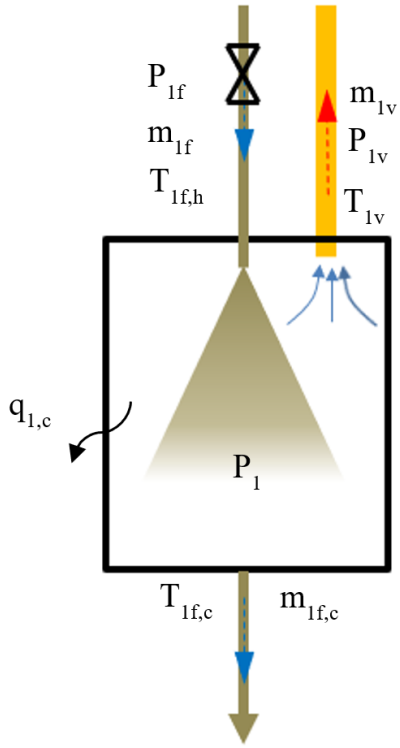

Figure 7.6 The schematic diagram of stage-1 evaporation modeling.

From the design target and application requirements, only $T_{1f,h}$ and m_{1v} are considered as given conditions in the first place. However, to solve the model, P_{1f}, m_{1f}, and P_1 also need to be determined as other input conditions due to the mathematical requirement. Therefore some other restrictions based on the working principles are required as follows:

First, to ensure no pre-cavitation happens before the spray atomization, P_{1f} must go beyond the local saturated pressure of the feeding brine with the temperature of $T_{1f,h}$. The minimum (or the most idealized value) of P_{1f}, equals the saturated pressure.

Second, two parameters m_{1f}, and P_1 are coupled together for determining the evaporative rate of the chamber. Initially, P_1 will be set preliminarily as a design reference. Then as long as a specific yield rate of m_{1v} is required, m_{1f} will be determined by the coupling calculation. Two variables must be double-checked after the calculation for

feasibility concerns. One is P_1 we just mentioned, which should be beyond the value of terminal vacuum level plus the pressure drop along the vapor path, to ensure the operation is realizable. The other one is the dimensional requirement of the evaporator, such as the height of the chamber, which must meet the minimum value based on the modeling prediction, to guarantee droplets have enough time for evaporation.

Last, based the above discussion, P_{1f}, m_{1f}, $T_{1fh,}$ and P_1 are considered as given conditions for each computational step during the iteration. To obtain $T_{1f,c}$, $m_{1f,c}$, T_{1v}, P_{1v}, m_{1v}, $q_{1,c}$, governing equations regarding each key parameter are summarized in Table 7.2. The model of stage-1 evaporation section is closed by 13 unknowns with 13 equations.

Table 7.2 Governing Equations for Stage-1 Evaporation Modeling

Parameter	Governing equation	Equation number
T_d	$dT_d / dt = -h_{fg}\dot{m}_v / m_d c_l$	(s1.e-1)
T_v	$\frac{d(\rho_v c_{pv} u_v T_v)}{dx} = n_d \left[\dot{m}_v c_{pv} T_d + h \frac{\pi}{4} d_d^2 (T_d - T_v) - \dot{q}_{loss} \right]$	(s1.e-2)
$T_{1f,c}$	$T_{1f,c} = T_d$	(s1.e-3)
T_{1v}	$T_{1v} = \overline{T}_v$	(s1.e-4)
u_d	$(m_d + m_a)\frac{du_d}{dt} = (m_d - V_d \rho_v)g - F_d - F_b$	(s1.e-5)
u_v	$\frac{d(\rho_v u_v)}{dx} = n_d \dot{m}_v$	(s1.e-6)
m_d	$m_d = \rho_d \frac{\pi}{6} d_d^3$	(s1.e-7)

Table 7.2 Governing Equations for Stage-1 Evaporation Modeling (Continued)

Parameter	Governing equation	Equation number
m_v	$\dot{m}_v = 5.84\times10^{-1}\alpha\alpha_L A_d \sqrt{\frac{M_w}{T_d}} \frac{\left(N_w P_d - P_\infty\right)}{133.322}$	(s1.e-8)
m_{1v}	$m_{1v} = m_v$	(s1.e-9)
$m_{1f,c}$	$m_{1f,c} = m_{1f} - m_{1v}$	(s1.e-10)
$q_{1,c}$	$q_{1c} = q_c$	(s1.e-11)
q_c	$q_c = h_w S_{ch}(T_{ch} - T_0)$	(s1.e-12)
q_{loss}	$q_{\text{loss}}(x) = \frac{T_v(x) - T_\infty}{1/h_c(x)2\pi r_{c,i} + \ln(r_{c,o}/r_{c,i})/2\pi k_c + 1/h_\infty 2\pi r_{c,o}}$	(s1.e-13)

7.2.4 Modeling of Stage-1 Mixing and Condensation

Mixing and condensation of Stage-1 is the next process that follows evaporation. The schematic diagram of modeling the stage-1 mixing and condensation is presented in Figure 7.7. The system is designed to work in a steady condition, which means the salinity should be kept in a constant value all the time. Therefore, the processing modeling of feed discharge and supply (mixing process) is developed below.

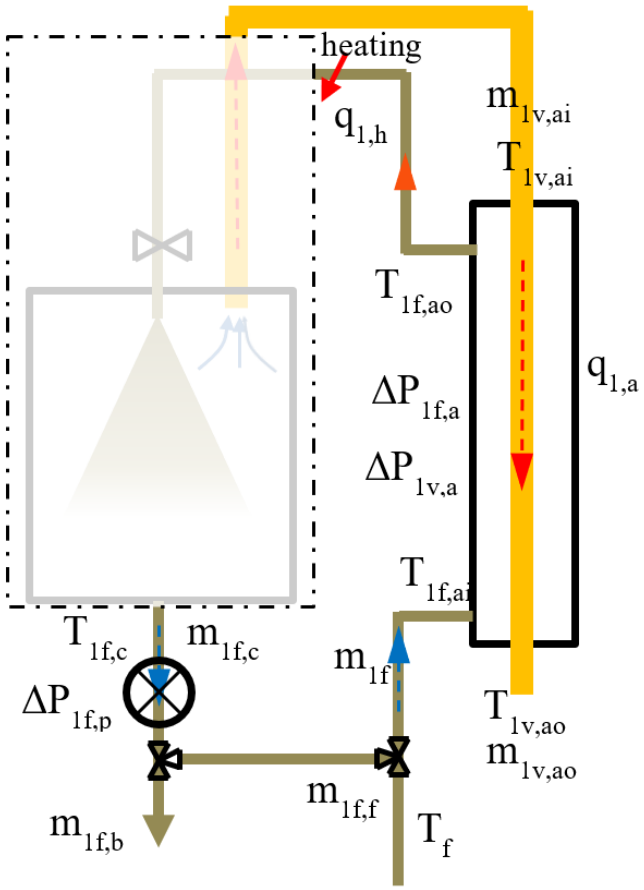

Figure 7.7 The schematic diagram of stage-1 mixing and condensation modeling.

Based on the equilibrium of salinity, we have the brine discharge mass flow rate:

$$m_{f,b} = \frac{m_v Cs_f}{m_f Cs_0 / m_{f,c} - Cs_f} \tag{7.4}$$

Then the mass flow rate of feed supply can be determined by:

$$\dot{m}_{f,f} = \dot{m}_v + \dot{m}_{f,b} \tag{7.5}$$

Assume the pipe is insulated, the pump work is:

$$W = \Delta P_{f,p} \frac{m_{f,c}}{\rho_f} \tag{7.6}$$

Where $\Delta P_{f,p} \geq P_a - P_1$

The temperature increased due to the pump work:

$$\Delta T_p = \frac{W}{m_{f,c} c_f} \tag{7.7}$$

Then we have feed temperature of condenser inlet:

$$T_{f,i} = \frac{m_{f,f} T_f + (m_f - m_{f,f})(T_{f,c} + \Delta T_p)}{m_f} \tag{7.8}$$

Next is the vapor condensing process. Assume the entire condenser is insulated with outside environment. Based on NTU method, we have:

$$T_{f,i} = \frac{m_{f,f} T_f + (m_f - m_{f,f})(T_{f,c} + \Delta T_p)}{m_f} \tag{7.9}$$

And since $Cr = \frac{C_{\min}}{C_{\max}} = 0$

The effectiveness of condenser we have is $\varepsilon = 1 - \exp(-NTU)$.

$$NTU \equiv \frac{UA_e}{C_{\min}} = \frac{UA_e}{\dot{m}_l c_l} \tag{7.10}$$

Since A_e is the total surface area of condenser, which is given, we need to calculate the overall coefficient U.

For the condensation side, since there always is a sucking force by vacuum, assume the condensation happens inside the condenser with dropwise condensation, then for the heat transfer coefficient, we have:

$$\bar{h}_{dc} = 51101 + 2044 T_{sat}$$

Where T is Celsius degree, picked by the average local pressure inside this channel. For the cyclic waterside we have:

$$\mathrm{Re}_D = \frac{4\dot{m}_l}{\pi D_h \mu}$$

Where if the condenser comes with round pipe or rectangular pipe within ratio of 3, then $D_h \equiv \frac{4A_c}{P}$ is hydraulic diameter.

If the condenser comes with very small thin channel like compact heat transfer, $D_h \equiv l_c$, where l_c is the thickness of channel.

For the laminar flow $Nu_D = 3.66$

For the turbulent flow $Nu_D = 0.023\,\mathrm{Re}_D^{4/5}\,\mathrm{Pr}^{0.4}$

Where Pr of water is a polynomial relation with T (Celsius degree)

$$\mathrm{Pr} = -1.049\times10^{-5}T^3 + 0.002707T^2 - 0.2603T + 11.09$$

$$h_w = Nu_D \frac{k_l}{D_h}$$

For the condenser wall we have: $K = k_c / \sigma$, where the material is aluminum and σ is the wall thickness. Finally the overall U is :

$$U = \frac{1}{1/h_{dc} + 1/K + 1/h_w} \tag{7.11}$$

Equation (7.11) can be directly solved based on the spraying calculation before. Therefore we can get NTU. Further, the cooling rate of the condenser will be:

$$q_a = \varepsilon \dot{m}_f c_f (T_{v,i} - T_{f,i}) \tag{7.12}$$

In addition, we can also determine:

$$m_{v,o} = m_{v,i} - \Delta m = m_{v,i} - \frac{\varepsilon q_{\max}}{h_{fg}} \tag{7.13}$$

The modeling of vapor pressure drop during the condenser is also developed below. The detailed condensation model will depend on what kind of heat transfer we are using. In our system, the helical tubing condenser is adopted.

For both vapor and feed sides, the Re can be determined as:

$$D_h = 4A_d / P$$

$$u_l = \frac{m_l}{\rho_l A}$$

$$\mathrm{Re}_D = \frac{\rho_l u_l D_h}{\mu_l}$$

Assume the helical effect along the tube is negligible, the pressure drop of the feed side is:

$$\Delta P = f \frac{\rho u_f^2}{2D_h} \Delta L \tag{7.14}$$

For laminar flow we have: $f = \dfrac{64}{\mathrm{Re}_D}$

For turbulent flow we have: $\dfrac{1}{\sqrt{f}} = 2\log(\mathrm{Re}\sqrt{f}) - 0.8 \qquad \mathrm{Re} > 3000$

For vapor side the pressure drop is:

$$\Delta P = f \frac{\rho u_s^2}{2D_h} \Delta L \tag{7.15}$$

Where $f = (0.7901 \times \ln \mathrm{Re}_D - 1.64)^{-2}$ [63]

Now $T_{1f,c}$, $m_{1f,c}$, T_{1v}, P_{1v}, m_{1v}, m_{1f}, are given inputs that can be obtained by solving the evaporation section of stage-1. In addition, Cs_0, Cs_f, and T_f are also considered as designed inputs, which represent the initial salinity of spray when entering the evaporator, the salinity of supplied fresh feed, and temperature of fresh feed, respectively.

Corresponding to the Figure 7.7, the governing equations regarding to each key parameter are summarized in Table 7.3. For the model of stage-1 mixing and condensation it consists of $m_{1f,b}$, $m_{1f,f}$, $T_{1f,ai}$, $T_{1f,ao}$, $m_{1v,ai}$, $T_{1v,ai}$, $T_{1v,ao}$, $m_{1v,ao}$, $m_{1y,ao}$, $q_{1,a}$,$q_{1,h}$, $\Delta P_{1f,p}$, $\Delta P_{1f,a}$, and $\Delta P_{1v,a}$ 14 unknowns with 14 governing equations.

Table 7.3 Governing Equations for Stage-1 Mixing and Condensation Modeling

Parameter	Governing equation	Equation number
$T_{1f,ai}$	$T_{f,i} = m_{f,f} T_f + (m_f - m_{f,f})(T_{f,c} + \Delta T_p) / m_f$	(s1.mc-1)
$T_{1f,ao}$	$T_{1f,ao} = q_{1,a} / m_f c_f + T_{1f,ai}$	(s1.mc-2)
$T_{1v,ai}$	$T_{1v,ai} = T_{1v}$	(s1.mc-3)
$T_{1v,ao}$	$T_{1v,ao} = T_{1v,ai}$	(s1.mc-4)
$m_{1f,b}$	$m_{f,b} = m_v Cs_f (m_{f,c} - Cs_f) / m_f Cs_0$	(s1.mc-5)
$m_{1f,f}$	$\dot{m}_{f,f} = \dot{m}_v + \dot{m}_{f,b}$	(s1.mc-6)
$m_{1v,ai}$	$m_{1v,ai} = m_{1v}$	(s1.mc-7)
$m_{1v,ao}$	$m_{1v,ao} = m_{1v} - q_{1,a} / h_{fg}$	(s1.mc-8)

Table 7.3 Governing Equations for Stage-1 Mixing and Condensation Modeling (Continued)

Parameter	Governing equation	Equation number
$m_{1y,ao}$	$m_{1v,ao} = q_{1,a} / h_{fg}$	(s1.mc-9)
$\Delta P_{1f,p}$	$\Delta P_{1f,p} = P_{1f} + P_{1f,a} - P_1$	(s1.mc-10)
$\Delta P_{1f,a}$	$\Delta P_{1f,a} = f(u_{1f,a}, \Delta L)$ Equation (7.14)	(s1.mc-11)
$\Delta P_{1v,a}$	$\Delta P_{1f,a} = f(u_{1v,a}, \Delta L)$ Equation (7.14)	(s1.mc-12)
$q_{1,a}$	$q_{1,a} = f(\varepsilon, m_v, T_{v,i}, T_{f,i})$ Equation (7.12)	(s1.mc-13)
$q_{1,h}$	$q_{1,h} = m_{1f} c_f (T_{1f,h} - T_{1f,ao})$	(s1.mc-14)

7.2.5 Modeling of Stage-2

Since the parameters in 1b condenser have to be determined by coupling with stage 2 calculation. Since the initial spray temperature, $T_{2f,h}$ depends on both heat exchange within condenser 1b and spray flash distillation within the evaporator, the evaporation process and the mixing-condensation process of stage-2 are coupled with each other and have to be solved together. The schematic diagram of modeling the overall stage-2 is presented in Figure 7.8.

The evaporation, mixing, and condensation processes in stage-2 follow the same mechanism as in stage-1. However, the difference in stage-2 compared to the initial stage is that now only *m2v* is the given condition from the design target. Therefore, a pre-guess of $T_{if,h}$ is mathematically required to be another input. Next, similar to stage 1, P_{2f}, m_{2f}, and P_2 are also needed to be given.

Then a series of iteration calculations will be performed until the pre-guess input $T_{1f,h}$ get converged to the value of $T_{2f,bo}$. In other words, unlike stage-1, in inter stages (stage 2), the evaporation section and mixing-condensation section are coupled together for obtaining the result. In addition, $T_{1v,ao}$ and $m_{1v,ao}$ are the other inputs obtained from the calculation of stage-1. The governing equations of each variable in stage 2 are listed in Table 7.4.

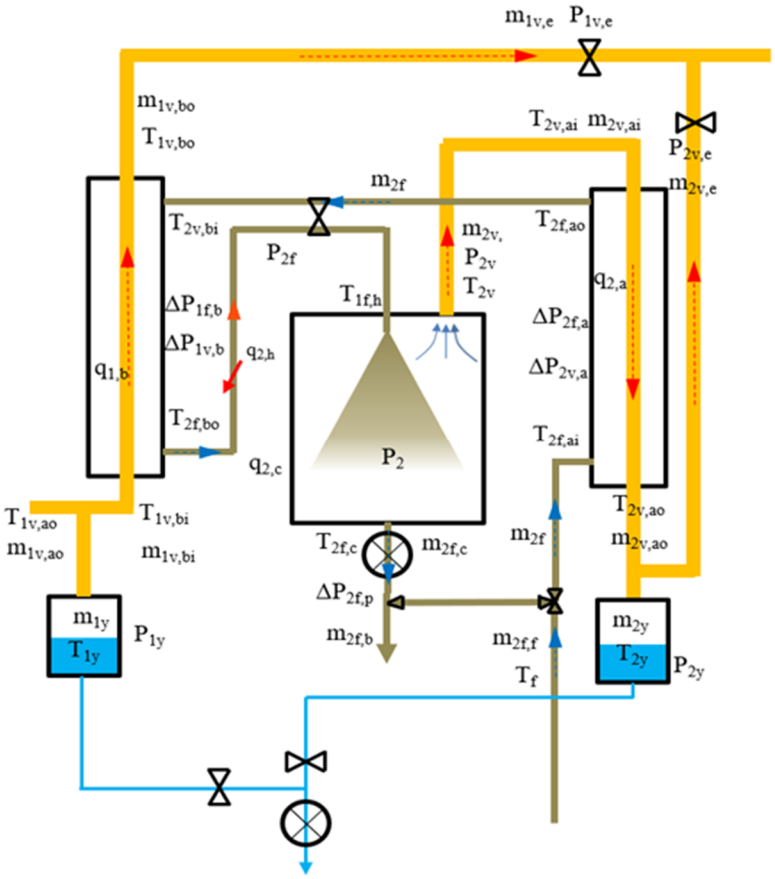

Figure 7.8 The schematic diagram of the overall processes in stage-2.

Now $T_{1f,c}$, $m_{1f,c}$, T_{1v}, P_{1v}, m_{1v}, m_{1f} are given inputs that can be obtained by solving the evaporation section of stage-1. In addition, Cs_0, Cs_f, and T_f are also considered as designed inputs, representing the initial salinity of spray when entering the evaporator, the salinity of supplied fresh feed, and the temperature of fresh feed, respectively.

Table 7.4 Governing Equations for All Processes of Stage-2

Parameter	Governing equation	Equation number
T_d	$dT_d / dt = -h_{fg}\dot{m}_v / m_d c_l$	(s2-1)
T_v	$\overline{T}_v(t) = \int_t^{t_e} \dot{m}_v T_d dt - q_c / (c_v \int_t^{t_e} \dot{m}_v dt)$	(s2-2)
$T_{2f,c}$	$T_{2f,c} = T_d$	(s2-3)
T_{2v}	$T_{2v} = \overline{T}_v$	(s2-4)
$T_{2f,ai}$	$T_{2f,ai} = f(mv, T_{2f,c}, \Delta P_{f,p})$ eq(23)	(s2-5)
$T_{2f,ao}$	$T_{2f,ao} = q_{1,a} / m_f c_f f + T_{2f,ai}$	(s2-6)
$T_{2v,ai}$	$T_{2v,ai} = T_{2v}$	(s2-7)
$T_{2v,ao}$	$T_{2v,ao} = T_{2v,ai}$	(s2-8)
$T_{2v,bi}$	$T_{2v,bi} = T_{2f,ao}$	(s2-9)
$T_{2f,bo}$	$T_{2f,bo} = q_{1,b} / m_{2f} c_{2f} + T_{2f,bi}$	(s2-10)
$T_{1v,bi}$	$T_{1v,bi} = T_{1v,ao}$	(s2-11)
$T_{1v,bo}$	$T_{1v,bo} = T_{1v,bi}$	(s2-12)
T_{1y}	$T_{1y} = T_{1v,ao}$	(s2-13)
m_{2v}	$m_{2v} = m_v$	(s2-14)
$m_{2f,c}$	$m_{2f,c} = m_{2f} - m_{2v}$	(s2-15)
$m_{2f,b}$	$m_{2f,b} = f(m_v)$ Equation (7.1)	(s2-16)
$m_{2f,f}$	$m_{2f,b} = f(m_v)$ Equation (7.2)	(s2-17)
$m_{2v,ai}$	$m_{2v,ai} = m_{2v}$	(s2-18)
$m_{1v,bi}$	$m_{1v,bi} = m_{1v,ao}$	(s2-19)
$m_{1y,bo}$	$m_{1y,bo} = q_{1,b} / h_{fg}$	(s2-20)

$m_{1v,bo}$	$m_{1v,bo} = m_{1v,bi} - q_{1,b} / h_{fg}$	(s2-21)

Table 7.4 Governing Equations for All Processes of Stage-2 (Continued)

Parameter	Governing equation	Equation number
m_{1y}	$m_{1y} = m_{1y,ao} + m_{1y,bo}$	(s2-22)
$m_{2v,ao}$	$m_{2v,ao} = m_{2v} - q_{2,a} / h_{fg}$	(s2-23)
$m_{2y,ao}$	$m_{2v,ao} = q_{2,a} / h_{fg}$	(s2-24)
$P_{2,v}$	$P_{2v} = P_2$	(s2-25)
$\Delta P_{2f,p}$	$\Delta P_{2f,p} = P_{2f} + P_{2f,a} + P_{1f,b} - P_2$	(s2-26)
$\Delta P_{2f,a}$	$\Delta P_{2f,a} = f(u_{2f}, \Delta L)$ Equation (7.14)	(s2-27)
$\Delta P_{1v,b}$	$\Delta P_{1v,b} = f(u_{1v,b}, \Delta L)$ Equation (7.15)	(s2-28)
$\Delta P_{2v,a}$	$\Delta P_{2v,a} = f(u_{2v,a}, \Delta L)$ Equation (7.15)	(s2-29)
$q_{2,c}$	$q_{2c} = q_c$	(s2-30)
$q_{2,a}$	$q_{2,a} = f(\varepsilon, m_v, T_{v,i}, T_{f,i})$ Equation (7.12)	(s2-31)
$q_{2,h}$	$q_{2,h} = m_{2f} c_f (T_{2f,h} - T_{2f,ao})$	(s2-32)

Eventually, the modeling of stage-2 is closed by 32 variables with 32 equations. As we mentioned in the evaporation section, after the convergence of calculation, the pre-designed values *P1* and *P2* need to be double-checked. Their vacuum level must be lower than $P_{1v,e}$ and $P_{2v,e}$. Meanwhile $P_{1v,e}$ and $P_{2v,e}$ must be lower than P_{3y}, to realize the controllability of the system.

7.2.6 Modeling of the Last Stage

For the last stage, $T_{f,0}$ and P_v are given as design targets. $T_{Lv,i}$ and $m_{Lv,i}$ are also could be determined based on the calculation from previous stages. The residue of the gaseous phase is a curial parameter that needs to be determined in order to obtain the capacity requirement of the vacuum pump. Additionally, the detailed modeling methodology for determining the vacuum capacity is developed below. The schematic diagram of modeling the last stage is exhibited in Figure 7.9.

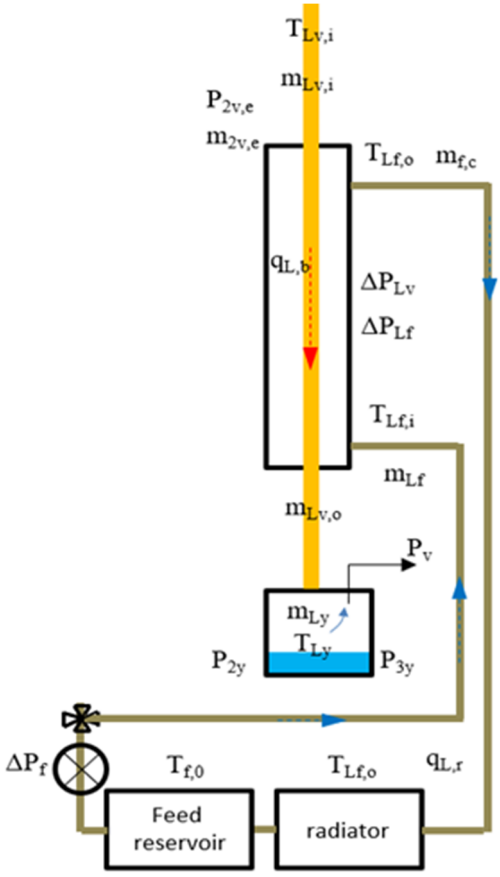

Figure 7.9 The schematic diagram of modeling the last stage.

The average inlet steam temperature and mass flow rate of the last stage is:

$$T_{Lv,i} = \frac{\sum_{i=1}^{N} m_{iv,e} T}{\sum_{i=1}^{N} m_{iv,e}} \tag{7.16}$$

$$m_{Lv,i} = \sum_{i=1}^{N} m_{iv,e} \tag{7.17}$$

The mole flow rate of steam residual can be expressed by:

$$\dot{N}_v = \frac{\dot{m}_{Lv,i} \times 1000}{MW_v} \tag{7.18}$$

Define the mass concentration of NCG, for example, 2‰ among the total yield, then it has:

$$\dot{m}_{NCG} = \dot{m}_{Lv,i} \times 0.0002 \tag{7.19}$$

Then the mole flow rate of NCG is determined as:

$$\dot{N}_{NCG} = \frac{\dot{m}_{NCG} \times 1000}{MW_{NCG}} \tag{7.20}$$

The required sucking volume rate could be obtained based on idea gas law:

$$\dot{V} = \frac{\dot{N}_v + \dot{N}_{NCG}}{P_{3y}} RT \tag{7.21}$$

Then from ideal gas law we have:

$$P_{3y}\dot{V}_{3y} = P_v\dot{V}_v$$

$$\dot{V}_v = \frac{P_{3y}}{P_v}\dot{V}_{3y} \tag{7.22}$$

The exhaust volume capacity of traditional vacuum pump could be calculated as:

$$V_{\max} = \frac{W_{input,\max} \times \eta}{\Delta P} \tag{7.23}$$

Eventually, we have 12 unknowns $T_{Lv,i}$, T_{Ly}, $T_{Lf,i}$, $T_{Lf,o}$, $m_{Lv,i}$, $m_{Lv,o}$, m_{Ly}, ΔP_{Lv}, ΔP_{Lf}, P_v, m_{vac}, and $q_{L,r}$ with 12 governing equations, which are summarized in Table 7.5.

Table 7.5 Governing Equations for Modeling the Last Stage

Parameter	Governing equation	Equation number
$T_{Lv,i}$	$T_{Ly,i} = \sum_{i=1}^{N} m_{iv,e} T / \sum_{i=1}^{N} m_{iv,e}$	(Ls-1)
T_{Ly}	$T_{Ly} = T_{Ly,i}$	(Ls-2)
$T_{Lf,i}$	$T_{Lf,i} = T_f$	(Ls-3)
$T_{Lf,o}$	$T_{Lv,bo} = T_{1v,bi}$	(Ls-4)
$m_{Lv,i}$	$m_{1v,bi} = m_{1v,e} + m_{2v,e}$	(Ls-5)
$m_{Lv,o}$	$m_{Lv,o} = \dot{m}_{NCG}$	(Ls-6)
m_{Ly}	$m_{Lv} = \dot{m}_{1v,bi}$	(Ls-7)
m_{vac}	$m_{vac} = \dot{m}_{NCG}$	(Ls-8)
ΔP_{Lv}	$\Delta P_{Lv} = f(u_{Lv}, \Delta L)$ Equation (7.15)	(Ls-9)
ΔP_{Lf}	$\Delta P_{Lf} = f(u_{Lf}, \Delta L)$ Equation (7.14)	(Ls-10)
P_v	$m_{1v,bo} = m_{1v,bi} - q_{1,b} / h_{fg}$	(Ls-11)
$q_{L,b}$	$q_{L,b} = m_{Lv,i} h_{fg}$	(Ls-12)

7.2.7 Summary of the overall modeling algorithm

In this section, the overall computational algorithm is summarized as follows for determining every key parameter during the operation.

(1). The evaporating pressures in each evaporator should be pre-set with an estimated value, which needs to be double-checked in the end that the assumed valves must

be higher than the terminal vacuum level plus the pressure drop along the vapor path. And the chamber height should be high enough to let the droplet achieve the desired terminal status according to the calculation.

(2). Based on the case set up P_{1f}, m_{1f}, T_{1fh}, T_f is determined.

(3). Take the initial stage as an example. Based on the governing equations (a), (b) and (c), the equations from (1)-(19) are solved and the values of $T_{1f,c}$, $m_{1f,c}$, T_{1v}, P_{1v}, m_{1v}, $q_{1,c}$, $m_{1v,ai}$, $T_{1v,ai}$ are determined.

(4). From eq(20)-(23), $m_{1f,b}$, $m_{1f,f}$, $T_{1f,ai}$ and $\Delta_{P1f,p}$ are determined.

(5). From eq(24)-(27), $T_{1f,ao}$, $T_{1v,ao}$, $m_{1v,ao}$, $q_{1,a}$, $\Delta_{P1f,p}$, $\Delta_{P1f,p}$, $T_{1v,bi}$, $m_{1v,bi}$ are determined.

(6). The results of 1b condenser need to be determined by coupling with stage 2 calculation. Hence a initial guess of $T_{1f,h}$ needs to be introduced.

(7). Similar as the stage1, based on the governing equations (a), (b) and (c), the values of $T_{2f,c}$, $m_{2f,c}$, T_{2v}, P_{2v}, m_{2v}, $q_{2,c}$, $m_{2v,ai}$, $T_{2v,ai}$ are determined.

(8). From eq(20)-(23), $m_{2f,b}$, $m_{2f,f}$, $T_{2f,ai}$ and $\Delta_{P2f,p}$ are determined.

(9). Since two condensers 2a and 1b, are serial arrangement, then from eq(24)-(27),$T_{2f,ao}$, $T_{2v,ao}$ $m_{2v,ao}$,m_{2y}, T_{2y}, $q_{2,a}$, $\Delta P_{2f,a}$,$\Delta P_{2v,a}$, $T_{2v,bi}$, $m_{2v,bi}$,$T_{2v,bi}$, $T_{2f,bo}$ $m_{1v,bo}$ $T_{1v,bo}$ $\Delta P_{1f,b}$, $\Delta P_{1v,b}$ are determined. Combined with the result of No.5 procedure, m_{1y} and T_{1y} will be determined.

(10). The $T1f,h$ is also determined by No.9 step, so a coupling calculation will be performed from N0.6 to No.10, until the results get convergence.

(11). The designed vacuum level in each chamber will be checked with final results by considering pressure drop along each path. The $P_{1v,e}$ and $P_{2v,e}$ must be bigger than P_{3y}.

(12). From eq(31)-(37), the $T_{f,0}$, $T_{l,f}$, $T_{Lf,i}$, $T_{Lf,o}$, $m_{f,c}$, ΔP_{Lv}, ΔP_{Lf} of the last stage will be determined. Further, the required cooling capacity of the radiator is determined.

7.3 Case Study

In this section, an exemplary case is performed both theoretically and experimentally. The spray calibration and geometric information of the case are summarized in Table 7.6. The physical properties adopted in modeling calculation are summarized in Table 7.7. In

addition, a schematic diagram of the case study is exhibited in Figure 7.10 to show crucial parameters measured from the experimental system, which are also compared with modeling predictions. Such information is summarized in Table 7.8 and Table 7.9 corresponding to Stage-1 and Stage-2, respectively.

Table 7.6 Spray Calibration and Geometric Conditions

Parametric	Value	Unit
pressure drop of nozzle	8.7	psi
spray pattern	full-cone	N/A
spray angle	57	degree
photo area (vertical direction)	139-258 (nozzle exit is 0)	mm
photo area (horizontal direction)	0-179 (spray central axis is 0)	mm
average spray velocity	3.23m/s	m/s
spray diameter distribution (Rosin-Rammler)	$1-Q=\exp-(D/0.876357)^{1.4711}$	mm
nozzle arrangement	One at center	N/A
numbers of nozzle	1	N/A
chamber height	0.5	m
chamber diameter	0.3	m
chamber material	stainless steel with insulation	N/A

Table 7.7 Temperature Dependency of Physical Properties

equations	remarks
$h_{fg}=aT^2+bT+c$	a=-1.794;b=-2256;c=2.5e6
$\rho_v= aT^3+bT^2+cT+d$	a=1.063e-6;b=-7.363e-5;c=0.002929;d=-0.01492
$u_v=aT+b$	a=4.031e-8;b=7.882e-6
$c_l= aT^4+bT^3+cT^2+dT^1+e$	a=1.815e-6;b=-4.754e-4;c=0.052;d=-2.139;e=4207
$c_{pv}= aT^2+bT+c$	a=0.01609;b=0.07276;c=1859

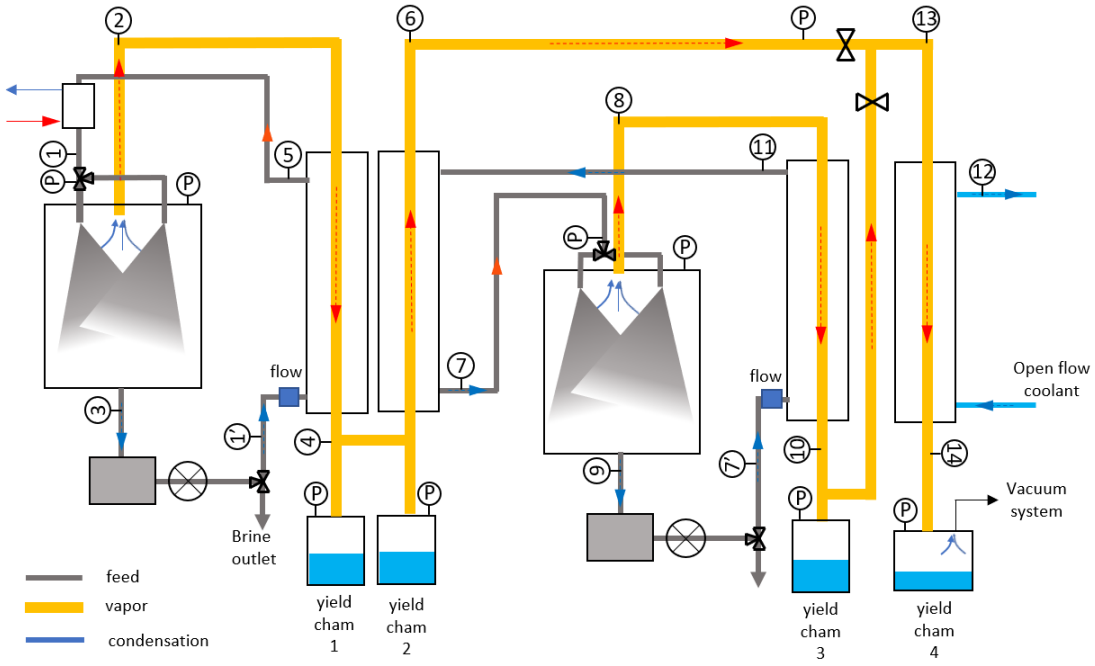

Figure 7.10 The schematic diagram of the case study.

Table 7.8 Results Comparison of Stage-1

parameter	experiment	model	error	Unit
evaporative press.	-0.551	-0.551	N/A	atm
cyclic flow rate	0.22	0.22	N/A	L/min
T1	93.3	93.3	N/A	℃
T2	81.3	81.9	0.7%	℃
T3	77.9	76.6	1.7%	℃
T4	78.9	78.6	0.4%	℃
T5	78.8	77.7	1.4%	℃
T1’	72.4	71.5	1.2%	℃
Ch_1 pressure	-0.59	-0.58	1.7%	atm
Ch_2 pressure	-0.62	-0.6	3.1%	atm
Ch_1 yield amount	345	356	3.2%	ml
Ch_2 yield amount	385	393	2.1%	ml

In Figure 7.10, the measured parameters are marked by either Arabic numbers or P. Arabic number indicates the order of the thermal couple, P indicates the pressure gauge. In addition, the cyclic flow rate of the brine and the yield amount for each yield chamber are also measured from the experiments. In Table 7.7 and 7.8, the relative errors are given

between the modeling results and the experimental results. For errors marked as "N/A", such corresponded parameters are treated as the initial conditions in the modeling calculation.

Table 7.9 Results Comparison of Stage-2

parameter	experiment	model	error	Unit
evaporative press.	-0.6	-0.58	N/A	atm
cyclic flow rate	1.3	1.3	N/A	L/min
T6	77.2	78.0	1.0%	℃
T7	71.0	70.6	0.6%	℃
T8	68.3	67.5	1.2%	℃
T9	69.3	68.9	0.6%	℃
T10	61.0	61.7	1.1%	℃
T11	70.0	69.3	1.9%	℃
T12	33.3	33.0	1%	℃
T13	65.9	64.8	1.7%	℃
T14	31.8	30.9	2.8%	℃
T7’	69.2	68.3	1.3%	℃
Ch_3 pressure	-0.62	-0.59	4.8%	atm
Ch_4 pressure	-0.64	-0.63	1.6%	atm
Ch_3 yield amount	250	259	3.6%	ml
Ch_4 yield amount	365	373	2.2%	ml

Other than the direct comparison between operating parameters, the systematic thermal performances are also compared between the experiment and modeling prediction. Specifically, the heat input for stage-1 and stage-2 evaporations, and the heat exchange within the condenser one to four (from left to right in Figure 7.9), can be determined by followed equations, respectively.

$$\dot{Q}_{evap.1} = \dot{m}_1 \times c_{p,w} \times (T1 - T3) \tag{7.24}$$

$$\dot{Q}_{evap.2} = \dot{m}_1 \times c_{p,w} \times (T7 - T9) \tag{7.25}$$

$$\dot{Q}_{cond.1} = \dot{m}_1 \times c_{p,w} \times (T5 - T1') \tag{7.26}$$

$$\dot{Q}_{cond.2} = \dot{m}_2 \times c_{p,w} \times (T7 - T11) \tag{7.27}$$

$$\dot{Q}_{cond.3} = \dot{m}_2 \times c_{p,w} \times (T11 - T7') \tag{7.28}$$

$$\dot{Q}_{cond.4} \approx (\dot{Q}_{evap.1} - \dot{Q}_{cond.1} - \dot{Q}_{cond.2}) + (\dot{Q}_{evap.2} - \dot{Q}_{cond.3}) \tag{7.29}$$

Table 7.10 listed the calculated thermal performances according to experimental data and modeling results, respectively. We can see the modeling prediction meets a fairly good agreement with experiments for each parameter, with the maximum relative error about 11%. This validation indicates our systematic model has the capability for predicting the thermal performance of our technology, which can be further used in system optimization and scale-up studies.

Table 7.10 Experimental and Modeling Thermal Performance

parameter	experiment	model	error	Unit
Qevap,1	14.23	15.43	8.4%	KJ/min
Qevap,2	9.280	9.282	3.1%	KJ/min
Qcond,1	5.914	5.729	8.4%	KJ/min
Qcond,2	6.550	7.098	0.02%	KJ/min
Qcond,3	4.370	4.860	11.2%	KJ/min
Qcond,4	6.676	6.425	3.8%	KJ/min

Overall speaking, our systematic model meets a good agreement with experiments according to both comparisons of parameters and thermal performance analysis. In addition, another method can also be used to justify the results by comparing the heat exchange amount between different condensers and yield amount between different yield chambers. Obviously, the ratio of vapor released heat in each condenser indicates a yield

apportion between each chamber. Such a heat exchange ratio should roughly equal the yield amount ratio we collected in the yield chamber.

Hence, according to the experimental data, the heat released ratio from vapor in each condenser is:

$$\dot{Q}_{cond.1} : \dot{Q}_{cond.2} : \dot{Q}_{cond.3} : \dot{Q}_{cond.4} = 1 / 1.11 / 0.74 / 1.13$$

Similar, the ratio of the collected yield amount in each yield chamber is:

$$Y_1 : Y_2 : Y_3 : Y_4 = 1 / 1.116 / 0.72 / 1.06$$

As a result, we can see both ratios meets a fairly good agreement with each other. Furthermore, by this way, the theoretical mixed vapor temperature of T_{13} can be calculated as:

$$\frac{(\dot{Q}_{evap.1} - \dot{Q}_{cond.1} - \dot{Q}_{cond.2}) \times T6 + (\dot{Q}_{evap.2} - \dot{Q}_{cond.3}) \times T10}{(\dot{Q}_{evap.1} - \dot{Q}_{cond.1} - \dot{Q}_{cond.2}) + (\dot{Q}_{evap.2} - \dot{Q}_{cond.3})} = 65.29C$$

Comparing with the real measurement of T_{13} as 65.9C, the result is very close. Therefore, we think the modeling methodology is valid.

7.4 Scale-up Study

Due to the safety concern of our lab, the external heat source (steam) is generated by electricity, in which the maximum power is about 7 kW. Such a heat input scale limited the entire processing capacity of our two-stage technology. In theory, the more stage the system has, the better thermal efficiency it can be achieved. In this section, the scale-up study is performed based on our systematic modeling. Based on the same component size as our lab-scale prototype, we calculated the thermal performances corresponding to

different yield capacities under three kinds of system setup: 1-stage system, 2-stage system, and a 4-stage system.

Corresponding to different yield capacities, the energy consumption from both heating and pumping sides are calculated with the three systems with different stages in Figure 7. The left axis is the required heating power as the initial heat input for flash distillation of stage-1, the right axis is the required total pumping power for both vacuum pump, brine pump, and yield pump. We can see, under the yield capacity. The four-stage system requires the minimum heating power, which is about half times of the two-stage system and only one-quarter of the single-stage system. Meanwhile, the pumping power consumption remains about similar, the system with more stages requires slightly more pumping power.

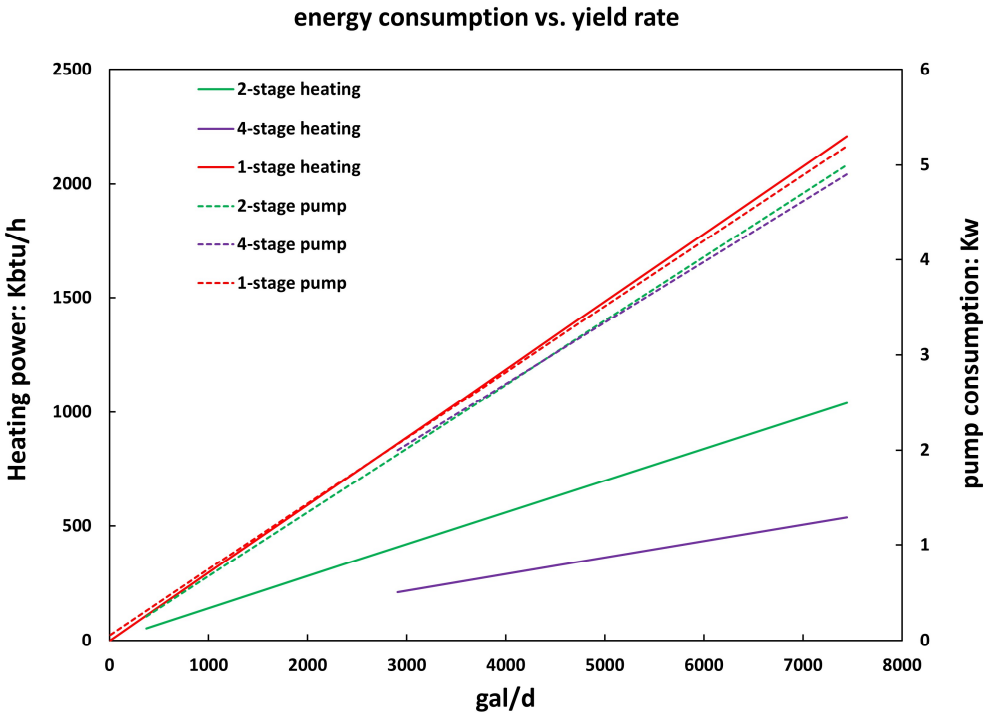

Figure 7.11 Scale-up estimation of energy consumption.

During the scale-up study, we also proposed a designed operating condition based on our current two-stage lab-scale prototype, which is assumed to be powered by propane to overcome the current limitation of the heat power input. We assume the overall yield rate of the system is targeted as 16 gal/hr with a feed flow rate of 0.2 kg/s. The new system will be powered by propane for heating and a small generator for pump and control to realize mobility. The heating power is estimated as 52000 BTU/hr, and the total electric consumption is estimated as 250watt. The vacuum capacity of the new system is 0.04 CFM with a 0.02% mass fraction of non-condensable gas and 0.15 atm vacuuming pressure. The overall size of the system is estimated to be compacter than 4 m^3 with 170 kg dry weight. In Figure 7.12, we put the above operating capacity and the experimental case into the scale-up results from Figure 7.11, and changed the scale as log-scale for a better exhibition.

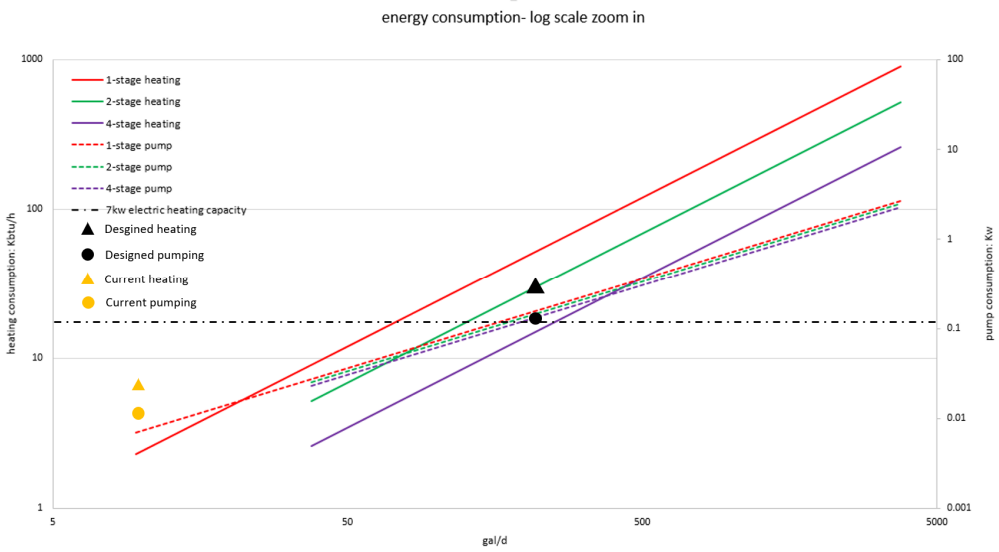

Figure 7.12 Scale-up estimation of energy consumption with two specific cases.

Other than energy consumption, vacuum capacity is also another concern in scale-up the system. More yield capacity of the system will result in more NCG during the process, which will increase the requirement of the vacuuming load. In Figure 7.13, the

vacuum capacity is calculated based on different yield rates and different mass ratios of the NCG during the evaporation. The designed capacity is marked as a red cross in the figure.

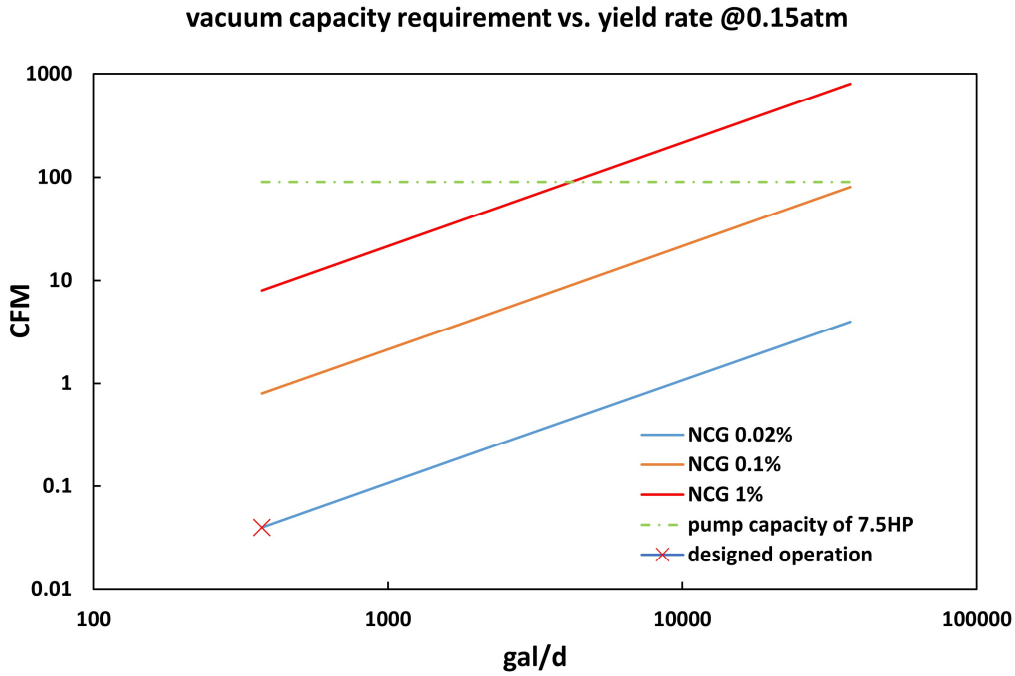

Figure 7.13 Scale-up estimation of vacuum capacity.

7.5 Conclusion

In this section, the design concept and thermal performance analysis of our distillation technology are performed based on a lab-scale two-stage prototype. The detailed system design is presented, and the overall systematic modeling methodology is proposed. An exemplary case study is performed based on this two-stage experimental system. We can see the modeling prediction meets a good agreement with experiments in terms of key operating parameters and featured thermal performances. Based on the model, the scale-up estimation is also discussed to show the potential performance on an industrial scale. The scale-up study indicates our system could achieve a good thermal performance and operating capacity.

CHAPTER 8

CONCLUSION SUMMARY AND FUTURE STUDY

8.1 Dissertation Conclusion

This dissertation aims to develop an innovative membrane-free low-grade energy driven distillation technology that overcomes the common drawbacks in current membrane distillation and thermal distillation. Our technology consists of three advanced features: (1) atomized spray, (2) active vapor extraction, and (3) multi-stagger-stage arrangement. As advantages, the system could be driven by low-grade energy, has better yield rates and energy efficiency, does not need membrane and brine's pre-treatment, has a wide treatment range and no scaling problem, and is safe and quiet for operating. To develop our technology, the highly non-equilibrium spray flash distillation process is studied. The unique phenomenon of thermal non-equilibrium between the two-phase (vapor and droplets) is reported. The coupled temperature-salinity polarization effect during the spray flash process is also investigated. Two kinds of droplets flash models (spatially dependent model and point-based model), and two kinds of vapor flow models (fully described 3-D Eulerian model and simplified 1-D Eulerian model) are proposed. Based on the point-based model, CFD study of the spray flash distillation process is also proposed. All proposed models can effectively predict the curial parameters of the distillation process, which provides important theoretical guidance for us in designing the real system. In this project, a lab-scale two-stage vacuum spray flash distillation system is built. The overall systematic modeling methodology is proposed with experimental validation. The model can effectively predict the processing characteristics and the thermal performance of the

system. In addition, a scale-up study based on the systematic model is discussed, which indicates our technology has the potential to achieve good thermal efficiency and yield capacity on an industrial scale.

8.2 Future Study

As for developing an innovative technology, a lot of work still needs to be done in the future. First, system optimization relies on a more accurate systematic model. The current study has not fully considered the non-line pressure drop of the vapor-water mixture during the condenser, which is a crucial parameter for accurately determining the terminal vacuum pressure for operation. Also, the system should realize an automatic operation eventually, which requires setting up a control system to monitor and adjust certain key processing parameters. Such related work is also desired to be done in the future. In addition, the yielding capacity of the current two-stage system is limited by the input power of the steam generator. In the future, a portable system with more heating power (such as a propane heater) is desired to realize a larger treatment capacity as well as to testify the system mobility (does not rely on electric power grid).

REFERENCES

[1] G. Guo, H. Deng, C. Zhu, and Z. Ji, "Modeling and experimental study of non-equilibrium isolated spray flash evaporation," in *5th Therm. Fluids Eng. Conf.*, p. 1–8, 2020.

[2] G. Guo, C. Zhu, and Z. Ji, "CFD simulation of isolated spray flash evaporation with active vapor extraction," in *5th Therm. Fluids Eng. Conf.*, p. 269–278, 2020.

[3] G. Guo, B. Zhang, C. Zhu, and Z. Ji, "Thermal non-equilibrium in spray flash with vacuum vapor extraction," *Desalination*, vol. 507, p. 115023, 2021.

[4] B. Zhang, G. Guo, C. Zhu, Z. Ji, and C.-H. Lin, "Transport and trajectory of cough-induced bimodal aerosol in an air-conditioned space," *Indoor Built Environm.*, p. 1420326X2094116, Jul. 2020.

[5] G. Guo, H. Deng, C. Zhu, and Z. Ji, "Non-volatile fraction effects in dispersed vacuum spray flash evaporation," in *International Mechanical Engineering Congress and Exposition*, 2020.

[6] H. Nassrullah, S. F. Anis, R. Hashaikeh, and N. Hilal, "Energy for desalination: A state-of-the-art review," *Desalination*, vol. 491, May, 2020.

[7] F. E. Ahmed, R. Hashaikeh, and N. Hilal, "Hybrid technologies: The future of energy efficient desalination – A review," *Desalination*, vol. 495, p. 114659, July 2020.

[8] M. A. Shannon, P. W. Bohn, M. Elimelech, J. G. Georgiadis, B. J. Marĩas, and A. M. Mayes, "Science and technology for water purification in the coming decades," *Nature*, vol. 452, no. 7185, pp. 301–310, 2008.

[9] O. Miyatake, T. Tomimura, Y. Ide, and T. Fujii, "An experimental study of spray flash evaporation," *Desalination*, vol. 36, no. 2, pp. 113–128, Feb. 1981.

[10] D. H. Troup and J. A. Richardson, "Scale nucleation on a heat transfer surface and its prevention," *Chem. Eng. Commun.*, vol. 2, no. 4–5, pp. 167–180, 1978.

[11] O. Miyatake, Y. Koito, K. Tagawa, and Y. Maruta, "Transient characteristics and performance of a novel desalination system based on heat storage and spray flashing," *Desalination*, vol. 137, no. 1–3, pp. 157–166, 2001.

[12] J. Hou, H. Cheng, D. Wang, X. Gao, and C. Gao, "Experimental investigation of low temperature distillation coupled with spray evaporation," *Desalination*, vol. 258, no. 1–3, pp. 5–11, 2010.

[13] M. Maria Antony Raj, K. Kalidasa Murugavel, T. Rajaseenivasan, and K. Srithar, "A review on flash evaporation desalination," *Desalina. Water Treat.* vol. 57, no. 29, pp. 13462–13471, Jun. 2016.

[14] I. Alatiqi, H. Ettouney, H. El-Dessouky, and K. Al-Hajri, "Measurements of dynamic behavior of a multistage flash water desalination system," *Desalination*, vol. 160, no. 3, pp. 233–251, 2004.

[15] P. Guo, T. Li, Y. Wang, and J. Li, "Energy and exergy analysis of a spray-evaporation multi-effect distillation desalination system," *Desalination*, vol. 500, p. 114890, 2021.

[16] A. Lefebvre and V. Mcdonell, *Atomization and Sprays, Second Edition.* Boca Raton, FL : CRC Press, 2017.

[17] A. Hosseini Araghi, M. Khiadani, M. H. Sadafi, and K. Hooman, "A numerical model and experimental verification for analysing a new vacuum spray flash desalinator utilising low grade energy," *Desalination*, vol. 413, pp. 109–118, 2017.

[18] O. Miyatake, T. Tomimura, Y. Ide, M. Yuda, and T. Fujii, "Effect of liquid temperature on spray flash evaporation," *Desalination*, vol. 37, no. 3, pp. 351–366, Jun. 1981.

[19] Y. Ikegami, H. Sasaki, T. Gouda, and H. Uehara, "Experimental study on a spray flash desalination (influence of the direction of injection)," *Desalination*, vol. 194, no. 1–3, pp. 81–89, Jun. 2006.

[20] S. Mutair and Y. Ikegami, "Experimental investigation on the characteristics of fl ash evaporation from superheated water jets for desalination," *Desalination*, vol. 251, no. 1–3, pp. 103–111, 2010.

[21] A. K. El-Fiqi, N. H. Ali, H. T. El-Dessouky, H. S. Fath, and M. A. El-Hefni, "Flash evaporation in a superheated water liquid jet," *Desalination*, vol. 206, no. 1–3, pp. 311–321, Feb. 2007.

[22] W. A. Sirignano, *Fluid Dynamics and Tandsport of Droplets and Spray*. Cambridge, UK : Cambridge University Press, 2010.

[23] C. Wang, R. Xu, Y. Song, and P. Jiang, "Study on water droplet flash evaporation in vacuum spray cooling," *Int. J. Heat Mass Transf.*, vol. 112, pp. 279–288, 2017.

[24] R. N. Dahms and J. C. Oefelein, "The significance of drop non-sphericity in sprays," *International Journal of Multip. Flow*, no. 86, pp. 67–85, 2016.

[25] L. D. Koffman, M. S. Plesset, and L. Lees, “Theory of evaporation and condensation,” *Phys. Fluids*, vol. 27, no. 4, pp. 876–880, 1984.

[26] A. H. Persad and C. A. Ward, “Expressions for the Evaporation and Condensation Coefficients in the Hertz-Knudsen Relation,” *Chem. Rev.*, vol. 116, no. 14, pp. 7727–7767, Jul. 2016.

[27] T. Ytrehus and S. Ostmo, “Kinetic theory approach to interphase processes,” *Int. J. Multiph. Flow*, vol. 22, no. 1, pp. 133–155, 1996.

[28] H. Y. Erbil, “Evaporation of pure liquid sessile and spherical suspended drops: A review,” *Adv. Colloid Interface Sci.*, vol. 170, no. 1–2, pp. 67–86, 2012.

[29] E.L.Cussler, *Diffusion Mass Transfer in Fluid System*, Cambridge, UK : Cambridge University Press, 2009.

[30] M. Bond and H. Struchtrup, “Mean evaporation and condensation coefficients based on energy dependent condensation probability,” *Phys. Rev. E - Stat. Physics, Plasmas, Fluids, Relat. Interdiscip. Top.*, vol. 70, no. 6, p. 21, 2004.

[31] C. A. Ward and G. Fang, “Expression for predicting liquid evaporation flux: Statistical rate theory approach,” *Phys. Rev. E - Stat. Physics, Plasmas, Fluids, Relat. Interdiscip. Top.*, vol. 59, no. 1, pp. 429–440, 1999.

[32] S.S.Penner, “On the Kinetics of Evaporation,” *J. Phys. Chem. A*, vol. 56, no. 4, pp. 475–479, 1952.

[33] T.H.Hwang and M.K.Moallemi, “Heat Transfer of Evaporating Droplet Flow in Low Pressure Systems.,” *Int. Commun. Heat Mass Transf.*, vol. 15, no. 5, pp. 635–644, 1988.

[34] W. L. Cheng, H. Chen, L. Hu, and W. W. Zhang, “Effect of droplet flash evaporation on vacuum flash evaporation cooling: Modeling,” *Int. J. Heat Mass Transf.*, vol. 84, pp. 149–157, 2015.

[35] Q. Chen, K. Thu, T. D. Bui, Y. Li, K. C. Ng, and K. J. Chua, “Development of a model for spray evaporation based on droplet analysis,” *Desalination*, vol. 399, pp. 69–77, Dec. 2016.

[36] B. Cai, Q. Wang, S. Yin, H. Gu, H. Wang, and H. Zhen, “Energy analysis of spray flash evaporation from superheated upward jets,” *Appl. Therm. Eng.*, vol. 148, pp. 704–713, 2019.

[37] C. Wang, R. Xu, X. Chen, P. Jiang, and B. Liu, “Study on water flash evaporation under reduced pressure,” *Int. J. Heat Mass Transf.*, vol. 131, pp. 31–40, Mar. 2019.

[38] S. Kooij, R. Sijs, M. M. Denn, E. Villermaux, and D. Bonn, "What Determines the Drop Size in Sprays?," *Phys. Rev. X*, vol. 8, no. 3, p. 31019, 2018.

[39] B. Zhang, G. Guo, C. Zhu, and Z. Ji, "Transport of aerosol by coughing in an air-conditioned space," in: *4th Therm. Fluids Eng. Conf.*, 2019, vol. 2019-April, pp. 1341–1353.

[40] T. D. Fansler and S. E. Parrish, "Spray measurement technology: A review," *Meas. Sci. Technol.*, vol. 26, no. 1, p. 12002, 2015.

[41] W. L. Cheng, W. W. Zhang, H. Chen, and L. Hu, "Spray cooling and flash evaporation cooling: The current development and application," *Renew. Sustain. Energy Rev.*, vol. 55, pp. 614–628, 2016.

[42] B. Cai *et al.*, "Mathematical study of spray flash evaporation in a spray-assisted seawater desalination chamber," *Desalination*, vol. 465, pp. 25–37, 2019.

[43] C. Zhu, Z. Ji, M. Zhou, G. Guo, and B. Zhang, "Vacuum distillation and desalination", US Patent No.10661194B2.

[44] A. Ismail, "Control of multi-stage flash desalination plants: A survey," *Desalination*, vol. 116, no. 2–3, pp. 145–155, 1998.

[45] Q. Chen, M. K. Ja, Y. Li, and K. J. Chua, "Energy, exergy and economic analysis of a hybrid spray-assisted low-temperature desalination/thermal vapor compression system," *Energy*, vol. 166, pp. 871–885, 2019.

[46] Q. Chen, S. J. Oh, Y. Li, and M. K. Ja, "Thermodynamic optimization of a low-temperature desalination system driven by sensible heat sources," *Energy*, vol. 192, 2020.

[47] H. E. S. Fath, "The non-equilibrium factor and the flashing evaporation rate inside the flash chamber of a multi-stage flash desalination plant," *Desalination*, vol. 114, no. 3, pp. 277–287, 1997.

[48] O. Miyatake, T. Hashimoto, and N. Lior, "The relationship between flow pattern and thermal non-equilibrium in the multi-stage flash evaporation process," *Desalination*, vol. 91, no. 1, pp. 51–64, 1993.

[49] N. Dombrowski and W. R. Johns, "The aerodynamic instability and disintegration of viscous liquid sheets," *Chem. Eng. Sci.*, vol. 18, no. 7, p. 470, 1963.

[50] P. H. Marmottant and E. Villermaux, "On spray formation," *J. Fluid Mech.*, vol. 498, no. 498, pp. 73–111, 2004.

[51] E. Villermaux and C. Clanet, “Life of a flapping liquid sheet,” *J. Fluid Mech.*, vol. 462, pp. 341–363, 2002.

[52] E. Villermaux, “Fragmentation,” *Annu. Rev. Fluid Mech.*, vol. 39, pp. 419–446, 2007.

[53] T. J. Tharakan, A. Mukhopadhyay, A. Datta, and M. A. Jog, “Trends in comprehensive modeling of spray formation,” *Int. J. Spray Combust. Dyn.*, vol. 5, no. 2, pp. 123–180, 2013.

[54] Y. Sun, A. M. Alkhedhair, Z. Guan, and K. Hooman, “Numerical and experimental study on the spray characteristics of full-cone pressure swirl atomizers,” *Energy*, vol. 160, pp. 678–692, 2018.

[55] S. Dehaeck, H. Van Parys, A. Hubin, and J. P. A. J. Van Beeck, “Laser marked shadowgraphy: A novel optical planar technique for the study of microbubbles and droplets,” *Exp. Fluids*, vol. 47, no. 2, pp. 333–341, 2009.

[56] X. Wang and C. Zhu, “Concentric evaporating spray jets in dilute gas-solids pipe flows,” *Powder Technol.*, vol. 129, no. 1–3, pp. 59–71, 2003.

[57] S. Ghaemi, P. Rahimi, and D. S. Nobes, “Evaluation of StereoPIV Measurement of Droplet Velocity in an Effervescent Spray,” *Int. J. Spray Combust. Dyn.*, vol. 2, no. 2, pp. 103–123, 2010.

[58] H. Albrecht, N. Damaschke, M. Borys, and C. Tropea, *Laser Doppler and Phase Doppler Measurement Techniques*. New York, NY : Springer Press, 2013.

[59] A. R. Jones, “Measurement Science and Technology Spray measurement technology: a review Recent citations,” *Meas. Sci. Technol.* vol. 26, p. 012002, 2015.

[60] H. M. Lu and Q. Jiang, “Size-dependent surface tension and Tolman’s length of droplets,” *Langmuir*, vol. 21, no. 2, pp. 779–781, 2005.

[61] R. Mei and R. J. Adrian, “Flow past a sphere with an oscillation in the free-stream velocity and unsteady drag at finite Reynolds number,” *J. Fluid Mech.*, vol. 237, pp. 323–341, Apr. 1992.

[62] S. L. Soo, *Multiphase fluid dynamics*. Oxford, UK : Butterworth-Heinemann Press, 1990.

[63] Theodore L. Bergman, Frank P. Incropera, David P. DeWitt, and Adrienne S. Lavine, *Fundamentals of Heat and Mass Transfer*. Hoboken, NJ : Wiley Press, 2011.

[64] S. Mutair and Y. Ikegami, “On the evaporation of superheated water drops formed by flashing of liquid jets,” *Int. J. Therm. Sci.*, vol. 57, pp. 37–44, 2012.

[65] S. Patankar, *Numerical Heat Transfer and Fluid Flow* . Boca Raton, FL : CRC Press, 2018.

[66] J. Porstendörfer, J. Gebhart, and G. Röbig, “Effect of evaporation on the size distribution of nebulized aerosols,” *J. Aerosol Sci.*, vol. 8, no. 6, pp. 371–380, 1977.

[67] P. Biswas, C. L. Jones, and R. C. Flagan, “Distortion of size distributions by condensation and evaporation in aerosol instruments,” *Aerosol Sci. Technol.*, vol. 7, no. 2, pp. 231–246, 1987.

[68] B. Zhang, C. Zhu, Z. Ji, and C.-H. Lin, “Design and characterization of a cough simulator,” *J. Breath Res.*, vol. 11, no. 1, p. 016014, 2017.

[69] A. G. Bailey, W. Balachandran, and T. J. Williams, “The rosin-rammler size distribution for liquid droplet ensembles,” *J. Aerosol Sci.*, vol. 14, no. 1, pp. 39–46, 1983.

[70] E. Jones, M. Qadir, M. T. H. van Vliet, V. Smakhtin, and S. mu Kang, “The state of desalination and brine production: A global outlook,” *Sci. Total Environ.*, vol. 657, pp. 1343–1356, 2019.

[71] G. Guo, H. Deng, C. Zhu, and Z. Ji, “Numerical study of vacuum-aided spray flash desalination,” *5-6th Therm. Fluids Eng. Conf.*, pp. 777–787, 2021.

[72] A. H. Persad and C. A. Ward, “Expressions for the Evaporation and Condensation Coefficients in the Hertz-Knudsen Relation,” *Chem. Rev.*, vol. 116, no. 14, pp. 7727–7767, 2016.

[73] A. E. Muthunayagam, K. Ramamurthi, and J. R. Paden, “Modelling and experiments on vaporization of saline water at low temperatures and reduced pressures,” *Appl. Therm. Eng.*, vol. 25, pp. 941–952, 2005.

[74] Y. Wu, X. Zhang, and X. Zhang, “Simplified analysis of heat and mass transfer model in droplet evaporation process,” *Appl. Therm. Eng.*, vol. 99, pp. 938–943, 2016.

[75] Q. Chen, K. J. M, Y. Li, and K. J. Chua, “Experimental and mathematical study of the spray flash evaporation phenomena,” *Appl. Therm. Eng.*, 2018.

[76] N. Shahidzadeh-Bonn, S. Rafai, D. Bonn, and G. Wegdam, “Salt crystallization during evaporation: Impact of interfacial properties,” *Langmuir*, vol. 24, no. 16, pp. 8599–8605, 2008.

[77] I. Taniguchi, T. Inoue, and K. Asano, “Evaporation of a salt water drop with crystallization,” *At. Sprays*, vol. 9, no. 1, pp. 69–85, 1999.

[78] S. Y. Misyura, “The crystallization behavior of the aqueous solution of CaCl2 salt in a drop and a layer,” *Sci. Rep.*, vol. 10, no. 1, pp. 1–10, 2020.

[79] Q. Chen, J. M. Kum, and K. J. Chua, “A spray assisted low-temperature desalination technology. ” *Emerging Technologies for Sustainable Desalination Handbook*, Butterworth-Heinemann, 2018.

[80] S. Sawamura, N. Egoshi, Y. Setoguchi, and H. Matsuo, “Solubility of sodium chloride in water under high pressure,” *Fluid Phase Equilib.*, vol. 254, no. 1–2, pp. 158–162, 2007.

[81] M. L. Williams, “CRC Handbook of Chemistry and Physics, 76th edition,” *Occup. Environ. Med.*, vol. 53, no. 7, pp. 504–504, 1996.

[82] H. Langer and H. Offermann, “On the solubility of sodium chloride in water,” *J. Cryst. Growth*, vol. 60, pp. 389–392, 1982.

[83] G. Guo, B. Zhang, C. Zhu, and Z. Ji, “Thermal non-equilibrium in spray flash with vacuum vapor extraction,” *Desalination*, vol. 507, p. 115023, Jul. 2021.

[84] R. Katal, T. Y. Shen, I. Jafari, S. Masudy-Panah, and Mohammad Hossein Davood Abadi Frahani, “An overview on the treatment and management of the desalination brine solution,” *Desalination-Chanllenges Oppor.*, vol. 1, pp. 1–28, 2020.

[85] V. Vitagliano and P. A. Lyons, “Diffusion Coefficients for Aqueous Solutions of Sodium Chloride and Barium Chloride,” *J. Am. Chem. Soc.*, vol. 78, no. 8, pp. 1549–1552, 1956.

[86] Y. Wu, X. Zhang, X. Zhang, and M. Munyalo, “Modeling and experimental study of vapor phase-diffusion driven sessile drop evaporation,” *Appl. Therm. Eng.*, vol. 70, no. 1, pp. 560–564, 2014.

[87] L. X. Huang, K. Kumar, and A. S. Mujumdar, “A comparative study of a spray dryer with rotary disc atomizer and pressure nozzle using computational fluid dynamic simulations,” *Chem. Eng. Process. Process Intensif.*, vol. 45, no. 6, pp. 461–470, 2006.

[88] M. H. Sadafi, I. Jahn, and K. Hooman, “Cooling performance of solid containing water for spray assisted dry cooling towers,” *Energy Convers. Manag.*, vol. 91, pp. 158–167, 2015.

[89] F. Xuening, C. Lei, D. Yuman, J. Min, and F. Jinping, “CFD modeling and analysis of brine spray evaporation system integrated with solar collector,” *Desalination*, vol. 366, pp. 139–145, 2015.

[90] ANSYS Inc., *ANSYS FLUENT 19.0 theory guide*. Canonsburg, PA: ANSYS Inc., 2019.

[91] Renato M. Cotta and Mikhail D. Mikhailov, *Heat Conduction: Lumped Analysis, Integral Transforms, Symbolic Computation*. Hoboken, NJ : Wiley Press, 1997.

[92] C. An and J. Su, “Improved lumped models for transient combined convective and radiative cooling of multi-layer composite slabs,” *Appl. Therm. Eng.*, vol. 31, no. 14–15, pp. 2508–2517, Oct. 2011.

[93] C. R. Regis, R. M. Cotta, and J. Su, “Improved lumped analysis of transient heat conduction in a nuclear fuel rod,” *Int. Commun. Heat Mass Transf.*, vol. 27, no. 3, pp. 357–366, Apr. 2000.

[94] J. Su, “Improved lumped models for asymmetric cooling of a long slab by heat convection,” *Int. Commun. Heat Mass Transf.*, vol. 28, no. 7, pp. 973–983, Sep. 2001.

[95] B. Abramzon and W. Sirignano, “Droplet vaporization model for spray combustion calculations,” *Int. J. Heat Mass Transf.*, vol. 32, no. 9, pp. 1605–1618, 1988.

[96] M. Zientara, D. Jakubczyk, M. Litniewski, and R. Holyst, “Transport of mass at the nanoscale during evaporation of droplets: The Hertz-Knudsen equation at the nanoscale,” *J. Phys. Chem. C*, vol. 117, no. 2, pp. 1146–1150, 2013.

[97] A. Kryukov and V. Levashov, *Non-Equilibrium Phenomena Near Vapor-Liquid Interfaces*. New York, NY : Springer Press, 2013.

[98] X. K. Kakatsios and R. N. Krikkis, “Effect of surface tension and evaporation on phase change of fuel droplets,” *Heat Transf. Eng.*, vol. 22, no. 3, pp. 33–40, 2001.

[99] Gabor A.Somorjai, *Introduction to surface chemistry and catalysis*. Hoboken, NJ : Wiley Press, 1994.

[100] B. Brown, *General Properties of Matter*. New York, NY : Springer Press, 2013.

[101] S. Burian, M. Isaiev, K. Termentzidis, V. Sysoev, and L. Bulavin, “Size dependence of the surface tension of a free surface of an isotropic fluid,” *Phys. Rev. E*, vol. 95, no. 6, 2017.

[102] R. C. Tolman, “The effect of droplet size on surface tension,” *J. Chem. Phys.*, vol. 17, no. 3, pp. 333–337, 1949.

[103] D. C. Agrawal and V. J. Menon, “Surface tension and evaporation: An empirical relation for water,” *Phys. Rev. A*, vol. 46, no. 4, pp. 2166–2169, 1992.

[104] E. M. Blokhuis and J. Kuipers, “Thermodynamic expressions for the Tolman length,” *J. Chem. Phys.*, vol. 124, no. 7, 2006.

[105] M. A. Eltawil, Z. Zhengming, and L. Yuan, “A review of renewable energy technologies integrated with desalination systems,” *Renew. Sustain. Energy Rev.*, vol. 13, no. 9, pp. 2245–2262, 2009.

[106] G. Guo and C. Zhu, “A modified lumped heat capacity model for droplet flash cooling,” *Int. Commun. Heat Mass Transf.*, vol. 127, p. 105557, Oct. 2021.

[107] S. A. Basha and K. Raja Gopal, “In-cylinder fluid flow, turbulence and spray models-A review,” *Renew. Sustain. Energy Rev.*, vol. 13, no. 6–7, pp. 1620–1627, 2009.